



저작자표시-비영리-변경금지 2.0 대한민국

이용자는 아래의 조건을 따르는 경우에 한하여 자유롭게

- 이 저작물을 복제, 배포, 전송, 전시, 공연 및 방송할 수 있습니다.

다음과 같은 조건을 따라야 합니다:



저작자표시. 귀하는 원저작자를 표시하여야 합니다.



비영리. 귀하는 이 저작물을 영리 목적으로 이용할 수 없습니다.



변경금지. 귀하는 이 저작물을 개작, 변형 또는 가공할 수 없습니다.

- 귀하는, 이 저작물의 재이용이나 배포의 경우, 이 저작물에 적용된 이용허락조건을 명확하게 나타내어야 합니다.
- 저작권자로부터 별도의 허가를 받으면 이러한 조건들은 적용되지 않습니다.

저작권법에 따른 이용자의 권리는 위의 내용에 의하여 영향을 받지 않습니다.

이것은 [이용허락규약\(Legal Code\)](#)을 이해하기 쉽게 요약한 것입니다.

[Disclaimer](#)

공학박사학위논문

연속적 이중거동을 하는 전개형 접이식  
소프트 로봇

Deployable Origami Soft Robots with  
Dual Sequential Motions

2022 년 2 월

서울대학교 대학원

기계항공공학부

김 응 배

# 연속적 이중거동을 하는 전개형 접이식 소프트 로봇

Deployable Origami Soft Robots with  
Dual Sequential Motions

지도교수 조 규 진

이 논문을 공학박사 학위논문으로 제출함

2021 년 10 월

서울대학교 대학원

기계항공공학부

김 응 배

김응배의 공학박사 학위논문을 인준함

2021 년 12 월

위 원 장 : 김 윤 영 (인)

부위원장 : 조 규 진 (인)

위 원 : 박 용 래 (인)

위 원 : 조 성 호 (인)

위 원 : 박 용 재 (인)

## **Abstract**

# **Deployable Origami Soft Robots with Dual Sequential Motions**

Woongbae Kim

School of Mechanical Engineering

The Graduate School

Seoul National University

In this thesis, development of deployable origami structures made of soft and flexible materials, and their soft robotic applications capable of deployment and additional motion (e.g., bending, inflating) are presented. The deployable origami structures produce the kinematically defined deployment by folding and unfolding. The developed soft deployable origami structures have additional range of motion due to the flexibility of the materials in addition to the kinematic deployment. By enabling pneumatic actuation, the soft

deployable structures can be guided to undergo quasi-sequential unfolding and additional motion of soft material. Two design methods are developed: the dual-morphing design method that utilizes the unfolding of the foldable structure and the stretching of soft materials, respectively, and the dual-origami design method that utilizes the asymmetric unfolding of origami structures.

Inspired by a peculiar motion of a pelican eel (*Eurypharynx pelecanoides*) that first unfolds its mouth and then inflates it, the dual-morphing structures that embody quasi-sequential behaviors of origami unfolding and skin stretching in response to fluid pressure were developed. In the proposed system, fluid paths are enclosed and guided by a set of entirely stretchable origami units. The dual-morphing feature arises from this geometric and elastomeric design of fluid networks in which fluid pressure acts in the direction that the whole body deploys first, resulting in quasi-sequential dual-morphing response. To verify the effectiveness of our design rule, an artificial creature mimicking a pelican eel and reproduced biomimetic dual-morphing behavior is built. By

compositing the basic dual-morphing unit cells into conventional origami frames, unprecedented architectures of soft machines that exhibit deployment-combined adaptive gripping, crawling, and large range of underwater motion are demonstrated. Furthermore, as an application, a soft bending actuator that using dual-morphing Yoshimura origami cylinder structures is developed. In response to applied pressure, the deployable soft pneumatic bending actuator (D-PneuNets actuator) can increase the moment arm due to the deployment of the origami chambers, thus overcoming the trade-off relationship between the output force and the bulkiness. A robotic soft glove using D-PneuNets actuator with space-efficient advantage was also developed.

The dual-origami design method is to superimpose a pneumatic-driven origami structure and an origami strain-limiting layer, to produce a quasi-sequential deployment and bending motion that is guided by unsymmetric unfolding of two origami components. The dual-origami structure is made of flexible materials with high stiffness compared to highly stretchable elastomers,

thus produces relatively high force and can be easily fabricated using low-cost FDM (Fused Deposition Modeling) 3D printer. The dominance between the deployment and bending can be shifted by varying the unfolding behavior, enabling pre-programming of the motion. Finally, soft gripper applications are presented: they successfully demonstrate gripping tasks that each requires strength, delicacy, precision and dexterity, and the high compactness when folded enables cooperation with a suction gripper without physical interference.

The design methods of deployable soft origami presented in this thesis provide guidelines that enable initially small soft robots but can be deployed to be functional, and they are expected to be applied to advanced next-generation soft robot systems.

**Keywords: Soft robots, Origami engineering, Soft actuators, Soft grippers**

**Student Number: 2015-20720**

# Contents

|   |           |
|---|-----------|
| <b>Abstract</b> .....                                     | <b>i</b>  |
| <b>Contents</b> .....                                     | <b>v</b>  |
| <b>List of Tables</b> .....                               | <b>x</b>  |
| <b>List of Figures</b> .....                              | <b>xi</b> |
| <br>  |           |
| <b>Chapter 1 Introduction</b> .....                       | <b>1</b>  |
| 1.1 Motivation.....                                       | 1         |
| 1.1.1 Soft Robots.....                                    | 1         |
| 1.1.2 Origami-inspired Engineering in Soft Robotics ..... | 2         |
| 1.2 Research Overview .....                               | 4         |
| <br>  |           |
| <b>Chapter 2 Deployable Origami Architectures</b> .....   | <b>8</b>  |
| 2.1 Miura Origami Polyhedron .....                        | 8         |
| 2.2 Yoshimura Origami Cylinder.....                       | 9         |
| 2.2 Origami Fish Base.....                                | 11        |
| <br>  |           |
| <b>Chapter 3 Bioinspired Dual-morphing Stretchable</b>    |           |

|  |           |
|--|-----------|
| <b>Origami (SOrigami) .....</b>  | <b>16</b> |
| 3.1 A Dual-morphing Behavior of the Pelican-eel.....   | 18        |
| 3.2 Working Principle of SOrigami .....  | 19        |
| 3.2.1 Pelican-eel-inspred Dual-morphing Stretchable origami .....  | 19        |
| 3.2.2 Comparison Between SOrigami and Conventional Origami...  | 22        |
| 3.2.3 2D Pseudo Rigid Body Modeling .....  | 25        |
| 3.3 Bio-mimicking dual-morphing pelican-eel origami .....  | 29        |
| 3.4 Dual-morphing Miura Origami.....   | 33        |
| 3.4.1 Pelican-eel-inspred Dual-morphing Stretchable origami .....  | 33        |
| 3.4.2 Definition of the Module, Deployment Ratio ( $\lambda$ ) and Angle ( $\phi$ )<br>of the Dual-morphing M-ori..... | 37        |
| 3.4.3 Parametric Study .....   | 39        |
| 3.4.4 Soft Robotic Applications of Dual-morphing M-ori .....   | 48        |
| 3.5 Dual-morphing Yoshumura Origami (Y-Ori).....   | 52        |
| 3.5.1 Design of Y-ori .....  | 52        |
| 3.5.2 Y-ori Deployable Caging Gripper .....  | 52        |
| 3.6 Materials and Methods.....   | 57        |
| 3.6.1 Materials for SOrigami .....   | 57        |
| 3.6.2 Layer Stacking Method for Fabrication.....   | 58        |
| 3.6.3 Experiment, Simulation and Analysis.....   | 62        |

|  |   |     |
|--|---|-----|
| 3.7  | Discussion .....  | 64  |
| <br>   |   |     |
| <b>Chapter 4 Application: Deployable Soft Pneumatic Networks (D-PneuNets) Actuator with Dual-morphing Origami Chambers..... 66</b> |   |     |
| 4.1  | Design of the D-PneuNets Actuator.....                    | 68  |
| 4.2  | Characterization of the Actuator .....                    | 71  |
| 4.2.1  | Concept Validation .....                                  | 71  |
| 4.2.2  | Characterization of the Behavior.....                     | 74  |
| 4.2.3  | Dual-material Yoshimura Origami Cylinder Chamber.....     | 80  |
| 4.3  | Robotic Soft Glove Using D-PneuNets Actuators .....       | 83  |
| 4.4  | Fabrication of D-PneuNets Actuators .....                 | 87  |
| 4.5  | Discussion .....  | 91  |
| <br>   |   |     |
| <b>Chapter 5 A Dual-origami Design for Soft Robots.... 94</b>  |   |     |
| 5.1  | Motivation: Drawbacks of the Dual-morphing Principle .... | 95  |
| 5.2  | Design and Working Principle .....                        | 98  |
| 5.2.1  | Dual-origami Components.....                              | 98  |
| 5.2.2  | Quasi-sequential Deployment and Bending Motion.....       | 99  |
| 5.3  | Pre-programming of the Motion .....                       | 106 |

|       |  |     |
|-------|--|-----|
| 5.3.1 | Simplified Kinematic Model.....  | 106 |
| 5.3.2 | Pre-programming Method.....  | 111 |
| 5.4   | Force Estimation: Simplified Pseudo rigid Body Model ...                           | 116 |
| 5.5   | 3D Printing and Heat Treatment of Dual-origami Soft Fluidic Bending Actuator ..... | 123 |
| 5.6   | Materials and Methods.....   | 126 |
| 5.6.1 | Characterization and Measurement.....  | 126 |
| 5.6.2 | Finite Element Analysis .....  | 127 |
| 5.6.3 | 3D Printing Process and Materials.....   | 127 |
| 5.7   | Discussion .....   | 128 |

**Chapter 6 Application: Soft Gripper Using Dual-origami Origami Actuators..... 131**

|     |   |     |
|-----|---|-----|
| 6.1 | Design of the Gripper.....                      | 131 |
| 6.2 | Characterization of the Gripper .....           | 134 |
| 6.3 | Development of a Versatile Soft Gripper .....   | 137 |
| 6.4 | Gripper Customized for Box-shaped Objects ..... | 141 |
| 6.5 | Discussion .....                                | 143 |

**Chapter 7 Conclusion..... 144**

Bibliography..... 145

국문초록..... 163

## List of Tables

|           |   |     |
|-----------|---|-----|
| Table 2.1 | Notations used in chapter 2 .....   | 15  |
| Table 3.1 | Notations used in chapter 3 .....   | 65  |
| Table 4.1 | Notations used in chapter 4 .....   | 93  |
| Table 5.1 | Comparison of the dual-origami design and dual-morphing<br>origami design ..... | 97  |
| Table 5.2 | Constant values in effective torsional stiffness model .....                    | 119 |
| Table 5.3 | Notations used in chapter 5 .....   | 130 |

## List of Figures

- Figure 1.1 Design strategy for the deployable soft origami structures ..... 6
- Figure 1.2 Commercially Available Elastomers. .... 7
- Figure 2.1 Paper origami architectures. (a) A Miura origami polyhedron.  
(b) A Yoshimura origami cylinder. (c) An origami fish base. 12
- Figure 2.2 A Miura origami polyhedron module. (a) Schematic of a 1-  
module rigid Miura-ori polyhedron. (b) The deployment  
behavior of a Miura-ori polyhedron characterized by the angle  
between adjacent modules ( $\theta_M$ )..... 13
- Figure 2.3 Yoshimura origami cylinders. (a) A paper Yoshimura origami  
pattern (left) and paper Yoshimura origami cylinders with  $N_F=$   
2, 3, and 4. (b) An elastomeric Yoshimura origami cylinder with  
 $N_F= 2$ . An inset image represents a cross-sectional drawing of  
an elastomeric Yoshimura origami cylinder ..... 14
- Figure 3.1 Pelican-eel-inspired dual-morphing stretchable origami. (a)  
The live pelican eel that dynamically extends its mouth. (b)  
Morphing principle of the pelican eel interpreted by the  
stretchable forms of origami fish base. (c) The concept of  
SOrigami. (d) Fabrication. (e) Morphing behaviors of

SOrigami, paper origami, and an elastomer unit in response to longitudinal stress in the direction that the system deploys. The inset images indicate the initial, unfolded, and stretched states of SOrigami..... 21

Figure 3.2 Scaling relationship of dual-morphing stretchable origami. (a) Basic 2D PRBM model derived from the dual-morphing stretchable origami unit cell. (b) Force diagram of the model. (c) P- $\theta$  relation with increasing thickness. (d) P- $\epsilon$  relation with increasing thickness. (e) Bending-stretching relationship with increasing thickness..... 28

Figure 3.3 A dual-morphing origami architecture mimicking a pelican eel (dual-morphing P-ori). (a) Dual-morphing P-ori built on double-layered origami fish base. (b) Geometric morphing of paper origami fish base. (c and e) Top and side view of the dual-morphing behavior of P-ori (left) and a live pelican eel (right). (d and f) Trajectory of the jaw end point of P-ori and a pelican eel from the top and side view..... 31

Figure 3.4 Kinematics of pelican eel and dual-morphing P-ori. (a and b) Overlaid images of pelican eel (left) and dual-morphing P-ori (right) from the top (a) and side view (b). We particularly

|            |   |    |
|------------|---|----|
|            | focused on the motion of the jaw end point, highlighted by red dots .....   | 32 |
| Figure 3.5 | Dual-morphing Miura origami (dual-morphing M-ori). (a) Kinematic composition and dual-morphing behavior of 6-module M-ori. Inset image: conventional morphing of a paper Miura-ori polyhedron. (b) Programmable dual-morphing responses of M-ori with distinct material disposition.. .....   | 35 |
| Figure 3.6 | Comparison between conventional fluidic bending actuators and M-ori. (a and b) Geometry of a 2-module conventional fluidic bending actuator (a) and a 2-module M-ori (b). The geometric values of both designs were equally defined: 1.5 mm of wall thickness, 30 mm of chamber width, and 40 mm of chamber length. (c) Comparison between bending and unfolding at the same pressure level (25 kPa) based on FEA. (d) Quantitative analysis of dual-morphing behavior of 2-module M-ori in comparison with a conventional pneumatic bending actuator. .... | 36 |
| Figure 3.7 | Deployment ratio ( $\lambda$ ) and angle ( $\phi$ ) of dual-morphing M-ori. (a) A process flow of measuring and calculating the length (L) and $\lambda$ of the dual-morphing M-ori. (b) Definition and measurement   |    |

|             |   |    |
|-------------|---|----|
|             | of $\phi$ . (c) Measurement of $\lambda$ and $\phi$ of four different dual-morphing M-ori .....   | 38 |
| Figure 3.8  | Parametric study of dual-morphing M-ori. (a and b) Quantitative analysis of dual-morphing behavior of 2-module M-ori for different values of geometric parameters, $\alpha$ (a) and $w$ (b). (c and d) Experimental and simulation results of deployment ratio ( $\lambda$ ) and deployment angle ( $\phi$ ) about 5 different dual-morphing M-ori.....                                 | 41 |
| Figure 3.9  | Parametric study of dual-morphing M-ori. (a and b) Top view of 2-module dual-morphing M-ori with different values of geometric parameters: $\alpha$ and $w$ . (c) The result of image analysis measuring the facet length. (d and e) Plot of the facet length change ( $L/L_0$ ) as a function of applied pressure for different values of geometric parameters: $\alpha$ and $w$ ..... | 42 |
| Figure 3.10 | Geometry-dominant origami-like morphing of dual-morphing M-ori with different $\alpha$ values.....  | 43 |
| Figure 3.11 | Dynamic behavior of the 2-module M-ori. ....  | 44 |
| Figure 3.12 | Strain-dominant soft robotic morphing of dual-morphing M-ori with programmed material disposition. (a) Programmed material disposition in a 2-module dual-morphing M-ori. (b)   |    |

Dual-morphing response of 2-module dual-morphing M-ori with different material disposition. (c, d) Inner or outer bending of 2-module dual-morphing M-ori in response to continuous fluid pressure ..... 45

Figure 3.13 The quasi-sequential motion of the bending M-ori. (a) A 3D plot of pressure, bending angle and deployment ratio. (b) Change in bending angle and deployment ratio during actuation 47

Figure 3.14 Tip force of the 6-module inner bending M-ori ..... 47

Figure 3.15 Soft robots consisting of dual-morphing M-ori. (a) The unique behavior of dual-morphing M-ori features initial compactness (thus capable of being concealed in a heap of sand), rapid deployment ( $<0.4$  s), and adaptive, functional morphing. (b) A soft crawling robot consisting of four 4-module dual-morphing M-ori demonstrates deployment-combined crawling locomotion characterized by the repeated transition in the second morphing mode. (c) A soft robotic eye tentacle consisting of 12-module dual-morphing M-ori and a wireless camera. (d) The robot's extreme shape changing capabilities can cover a wide field of vision..... 50

Figure 3.16 A dual-morphing M-ori gripper. (a and b) A dual-morphing M-ori gripper that hugs an object, taken from a top (a) and a side view (b). (c and d) A gripper that supports an object, taken from a top (c) and a side view (d) ..... 51

Figure 3.17 Architecture of material stiffness distribution the soft robotic eye tentacle ..... 51

Figure 3.18 Dual-morphing Yoshimura origami (dual-morphing Y-ori). (a) Dual-morphing response of 4-module Y-ori under fluidic pressurization compared with that of a paper Yoshimura-ori cylinder. (b) Morphing behavior and mechanism of the dual-morphing Y-ori caging gripper. (c and d) Characterization of dual morphing of the Y-ori caging gripper. While the gripper grows in the height direction with increasing applied pressure, the inner area reduces only during the 2nd morphing mode. (e) Universal dual-morphing gripping of irregular-shaped objects  
54

Figure 3.19 Dual-morphing Y-ori with programmability. Two different elastomers [DragonSkin30 (E1~600 kPa) and DragonSkin10 (E2~150 kPa)] are patterned differently with the same geometry in order to show multiple dual-morphing responses

of 4-module Y-ori ..... 55

Figure 3.20 A dual-morphing human-interactive soft robot. (a) The soft robot consists of a 7-module dual-morphing Y-ori (body) and two 4-module dual-morphing M-ori (arms) with a 3D printed rigid frame. The robot uses dual-morphing for both body development and hugging. (b) A dual-morphing behavior of the robot that hugs and lifts a doll using its arms and the body .. 56

Figure 3.21 Fabrication process of dual-morphing origami architectures: a layer stacking method. (a) Put a cover mold at the bottom and align a main layer mold. (b) Pour uncured low stiffness elastomer. (c) Place a separating layer mold. (d) Place a second main layer mold and pour uncured high stiffness elastomer. (e and f) Repeat the process from c to d for the stacking of 2- (e) and 4-module (f). Finally, place a cover layer mold to finish the stacking process. (g) Remove all layer molds. (h) Seal the cured structure using a half-cured silicone or a silicone adhesive .. 61

Figure 3.22 Image analysis process. (a) Experimental setup for the investigation of the morphing behavior of 2-module dual-morphing M-ori. Red markers are attached for image analysis. (b) The result of image analysis finding the positions of the red

|            |   |    |
|------------|---|----|
|            | markers .....   | 63 |
| Figure 4.1 | A D-PneuNets actuator with five Yoshimura origami cylinder structured chambers and its deployment and bending behavior  | 70 |
| Figure 4.2 | A force measurement experiment. (a) D-PneuNets and two soft pneumatic network actuators with each height equal to $H_{initial}$ and $H_{fold}$ . (b) An experimental setup for force measurement. (c) An experimental result of the force measurement ..... | 73 |
| Figure 4.3 | The deployment and bending behavior of a D-PneuNets actuator. (a) An experimental setup to measure the deployment and bending behavior. (b) FEA simulation results of the D-PneuNets actuator with $l_g = 3$ mm.....  | 77 |
| Figure 4.4 | Experimental and simulation result (a) of the curvature $\kappa$ and (b) the change in chamber height $\Delta H$ for the actuators with $l_g = 1$ mm and 3 mm.....  | 78 |
| Figure 4.5 | Simulation result of the D-PneuNets and PneuNets actuators for the internal volume and (b) the stored energy to applied pressure. (c) The relationship between the stored energy and the bending curvature.....   | 79 |
| Figure 4.6 | A Dual-material Yoshimura origami cylinder chamber. (a) A   |    |

|             |   |    |
|-------------|---|----|
|             | material composition of the dual-material chamber. (b) Dual-material origami chambers viewed from above. (c) Experimental and simulation results for the eccentricity of the origami chambers. (d) Experimental results for the burst pressure of the origami chambers.....   | 82 |
| Figure 4.7  | A prototype of the D-PneuNets soft robotic glove .....  | 85 |
| Figure 4.8  | Wrap grasping pressure measurement results for cylindrical objects of (a) diameter= 65mm and (b) diameter= 140mm...   | 85 |
| Figure 4.9  | Grasping tests with various objects. (a) Snack bag, (b) bath duck, (c) Sticky note set, (d) plastic cup set, (e) tennis ball, and (f) socket box.....   | 86 |
| Figure 4.10 | A schematic diagram of the fabrication process. (a) Assembly process of mold using neodymium magnet. (b) Fabrication process of the single-material chambers, (c) the dual-material chambers, (d) the inextensible strain-limiting layer. (e) Attachment process of the chambers and the strain-limiting layer..... | 90 |
| Figure 5.1  | Design and principle of the dual-origami soft fluidic bending actuator. (a) Unfolding of six-module dual-origami soft fluidic bending actuator. (b) Parent paper origami structures and their   |    |

schematic drawings of behavior in a dual-origami soft fluidic bending actuator. (c) Quasi-sequential deployment and bending motion of six-module dual-origami soft fluidic bending actuator. Insets represent corresponding simulation result.. 101

Figure 5.2 End-tip trajectories of dual-origami soft bending actuator and conventional soft pneumatic bending actuator..... 102

Figure 5.3 Deployment ratio ( $\lambda$ ) and bending angle ( $\phi$ ) in response to applied pressure..... 103

Figure 5.4 The quasi-sequential motion of the Dual-origami actuator. (a) A 3D plot of pressure, bending angle and deployment ratio. (b) Change in bending angle and deployment ratio during actuation 104

Figure 5.5 Dimensions of (a) dual-origami soft fluidic bending actuator ( $w= 6$  mm and  $l= 20$  mm) and (b) conventional soft bending actuator ..... 105

Figure 5.6 Linkage model for dual-origami soft fluidic actuator. (a) 6-module dual-origami soft fluidic actuator’s linkage model and position vectors. (b) Definition of angles for calculating position. (c) Comparison of model for bending angle and experimental result ..... 110

Figure 5.7 Linkage model for dual-origami soft fluidic actuator. (a) 6-module dual-origami soft fluidic actuator’s linkage model and position vectors. (b) Definition of angles for calculating position. (c) Comparison of model for bending angle and experimental result ..... 113

Figure 5.8 Pre-programming of 6-module dual-origami soft fluidic actuators. (a) For strain-limiting layer with different width ( $w$ ), six-module dual-origami soft fluidic bending actuators were placed in row and actuated simultaneously by same applied pressure. Experimental and simulation results for (b) end-tip trajectories, (c) deployment ratio ( $\lambda$ ), and (d) bending angle ( $\phi$ ) were plotted. (e, f, g, and h) Same procedure as (f-i) were performed for strain-limiting layer with different length ratio ( $L$ ) ..... 114

Figure 5.9 A parametric study of the relationship between the quasi-sequential deployment and bending motion and the thickness of the strain-limiting layer ( $t$ ). Data are achieved using FEA simulation. A) End-tip trajectories of the 6-module dual-origami fluidic soft actuators with variable  $t$ . B) Bending-to-deployment ratio factor in response to applied pressure ( $< 50$

|  |     |
|--|-----|
| kPa, deployment state) with variable $t$ .....                             | 115 |
| Figure 5.10 Pseudo rigid body model for dual-origami soft fluidic actuator |     |
| 117  |     |
| Figure 5.11 Free body diagram of the PRBM model .....                      | 117 |
| Figure 5.12 (a) Effective torsional stiffness $k_n$ in response to applied |     |
| pressure $P= 50\text{kPa}$ . FEA simulations were performed with           |     |
| interaction condition on and off respectively. (b) Change in $k_n$         |     |
| due to the contact of facets.....  | 118 |
| Figure 5.13 Modeling result of $k_n$ . (a) $n=1$ , and (b) $n>1$ . .....   | 120 |
| Figure 5.14 Force estimation for applied pressure of (a) 50 kPa and (b)    |     |
| 60kPa.....   | 122 |
| Figure 5.15 Fabrication and reinforcement of the dual-origami soft fluidic |     |
| bending actuator. (a) 3-step process of fabrication. (b)                   |     |
| Micrographs of raw surface and heat-treated surface. (c)                   |     |
| Maximum sealing pressure of raw air chamber and heat-treated               |     |
| air chamber.....   | 125 |
| Figure 5.16 Failure cases of the heat treatment. (a) Deformation occurred  |     |
| when the soft robot was heat-treated without constraining                  |     |
| aluminum blocks. (b) The soft robots melted when heat-treated              |     |
| at an excessively high temperature (180°C 6 hours) .....                   | 125 |

|             |   |     |
|-------------|---|-----|
| Figure 6.1  | A dual-origami two-finger gripping unit. Gripping motion and affordable object size of (a) a conventional soft gripper and (b) a dual-origami two-finger gripping unit, and comparison of their (c) possible approaching paths.....   | 133 |
| Figure. 6.2 | Motion and configuration design of the gripping units.....  | 133 |
| Figure. 6.3 | Experimental setup for gripping force measurement of the dual-origami two-finger gripping unit.....   | 135 |
| Figure. 6.4 | (a) The gripping force of the Design I gripping unit ( $P= 200\text{kPa}$ ) when the gripped cylinder ( $D= 50\text{mm}$ ) is pulled-out. (b) Peak gripping forces of the Design I gripping unit in response to applied pressure for different cylinder diameters.....  | 135 |
| Figure 6.5  | Repeatability test results of the dual-origami two-finger gripping unit. A) Side view of the dual-origami two-finger gripping unit at applied pressure of $40\text{ kPa}$ and number of cycles $N_{40\text{kPa}}$ . B) Variation of bending angle $\phi_N$ with the number of cycles $N_{40\text{kPa}}$ ..... | 136 |
| Figure 6.6  | A versatile soft gripper. (a) Overview of the developed gripper. (b) Pick-and-place for various objects of irregular shapes and sizes. (c) Depending on the object and environment, finger grip, suction grip, and collaborative grip could be considered   |     |

|            |  |     |
|------------|--|-----|
|            | respectively.....  | 139 |
| Figure 6.7 | A soft gripper. (a) grasping Korean radish weighing 1.3 kg, (b) raspberry, (c) a coin, and (d) inserting it in a coin slot.....  | 140 |
| Figure 6.8 | A soft gripper customized for box-shaped objects. (a) Overview of the two-finger gripping unit for box-shaped objects. (b) Box-shaped objects of different sizes. (c and d) Soft gripper picking and placing different boxes ..... | 142 |

# Chapter 1. Introduction

## 1.1 Motivation

### 1.1.1 Soft Robots

Advances in soft robotics have presented the way robots interact with human or unstructured environments. In response to external stimuli, such as fluidic pressure [1]–[19], electric signals [20]–[28], magnetic fields [29]–[36], and motor-tendon actuation [37]–[43], the architected soft matters, mostly elastomers, produce continuous and adaptive motions that allow delicate handling of fragile objects or shape adjusting to unstructured environments. By utilizing the inherent features of softness, soft robots are gradually being used for safety demanding applications or near human applications such as soft grippers [18], [29], [37], [44]–[48], soft manipulators [12], [21], [49]–[51], mobile robots [2], [10], [13], [14], [22], [30], [38], assistive wearable robots [15], [39], [52]–[55], and minimally invasive surgical tools [16], [34], [56]–[59]. The established design method for soft fluidic robots is to embody anisotropic deformation in soft bodies by carving geometric patterns of extensible fluidic networks and embedding inextensible strain-limiting appendages (e.g., paper strips, fabrics, tendons) [60], [61]. Consequently, the applied fluid causes asymmetric extension of fluidic networks and strain-

limiting appendages, and the whole soft body produces pre-programmed motion such as bending [61]–[64], twisting [65], and contraction [66], [67]. Researches to date have mainly focused on architecting fluidic networks and have achieved rapid actuation [62], high aspect ratio design [68], and high force generation [63], [64]. However, the current design method compels soft robots to be shaped as a long elastomeric beam or a cylinder because their form factors are subordinated to inextensible strain-limiting appendages, which may limit their spatial efficiency, and make it inconvenient for soft fluidic robots to be used with other mechanical elements due to physical interferences.

### **1.1.2 Origami-inspired Engineering in Soft Robotics**

Origami deployable architectures have unique feature that are folded into compact forms when not in use, and be transformed into large shapes to be functional. This deployment combined functionality provides portability and mobility at the folded state while it can generate large motions at the deployed state. For example, in nature, flying insects such as ladybugs and earwigs fold and retract their hind wings for reduced inertia, and only deploy and flap them during flight [69], [70]. With additional benefits such as desired shapes or motions which can be robustly guided by kinematics, and a large variety of constituting materials (from compliant paper to steel plate), the origami design

has been considered as a promising method for deployable machines with possible applications in mobile robots [71]–[76], manipulators [77]–[83], space missions [84]–[87], and biomedical tools [78], [88]–[90]. Likewise, several researches of soft fluidic robots have adopted origami deployable architectures [91]–[95]. Martinez et al developed paper-elastomer composite soft fluidic robots including Yoshimura origami cylinder structure (so-called bellows-like pattern) that grow or bend due to glued facets or an attached strip [91]. Li et al presented soft fluid robots in which an origami skeleton is sealed by flexible skin, and negative pressure is applied to fold the crease lines in a pre-programmed sequence [92]. Chen et al developed a hybrid actuator with a motor-driven tendon and a fluid-driven asymmetric Yoshimura origami cylinder, in which the effective length of the bending configuration can be changed [93]. These existing works successfully imported origami deployable architectures' large range of motion into fluidic networks, while they have not yet focused on designing or programming additional motions beyond kinematics of origami deployment. To address the problem, soft and compliant materials have recently been implemented in origami architectures to widen the accessible regime of origami folding over origami kinematics [96], [97].

## 1.2 Research Overview

The proposed research is to superimpose origami deployment and adaptive functional motion of soft robots (Fig. 1.1.). The design principle of the pneumatic-driven soft robot is to convert the expansion of the flexible body into another functional motion by attaching non-expandable appendages. When the origami structures are built with soft materials, their deployment also can be converted into additional motion by guiding asymmetric lengthening. Commercially available soft materials, highly stretchable silicones (Elastic modulus  $< 1000$  kPa) and thermoplastic polyurethanes (elastic modulus  $> 10000$  kPa), are shown in Fig. 1.2. The purpose of the research is to propose design methods for converting the deployment of soft origami structures, made of highly stretchable silicones or flexible TPUs, into additional motion to generate quasi-sequential deployment and soft robotic motion.

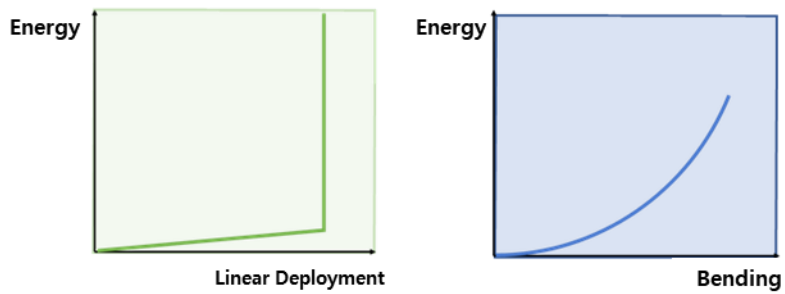
Chapter 2 introduces conventional deployable origami structures. Subsequent chapters deal with the contribution of the thesis:

- A dual-morphing principle that utilizing both origami unfolding and elastomeric stretching was presented, and by applying it to various origami structures, quasi-sequential deployment and additional motion was realized (Chapter 3).
- A deployable pneumatic bending actuator and a soft robotic

wearable glove utilizing the dual-morphing principle were developed (Chapter 4).

- A dual-origami design principle that superimpose two origami structures to generate quasi-sequential deployment and bending motion was developed (Chapter 5).
- Soft grippers with pneumatic-driven deployable fingers were developed by applying dual-origami design principle (Chapter 6).

# Deployable Origami      Soft Robot



## Deployable Soft Origami

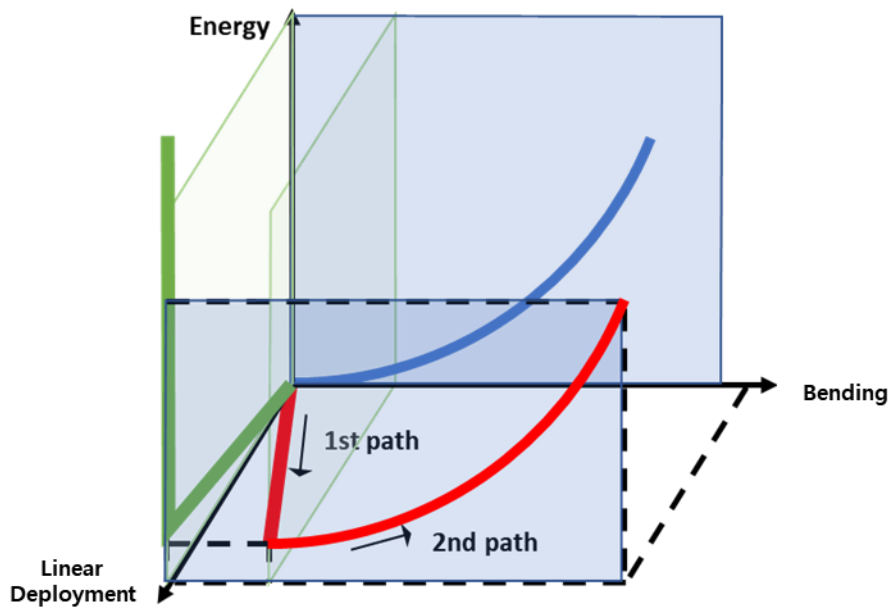
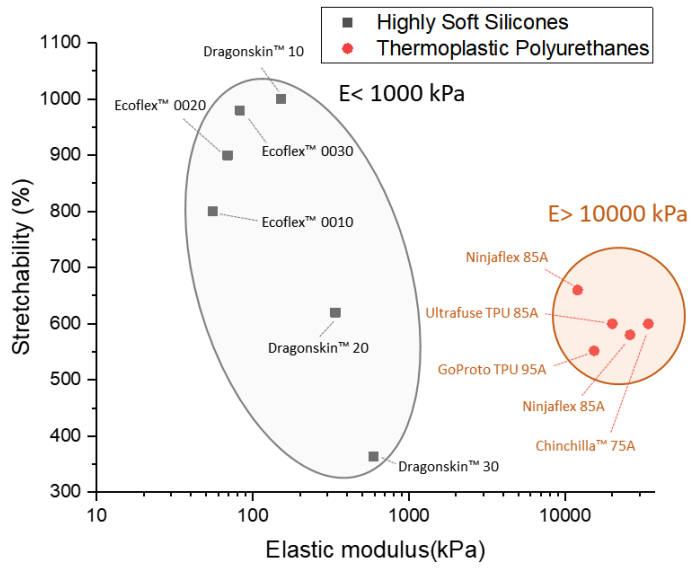


Fig. 1.1. Design strategy for the deployable soft origami structures.



**Fig. 1.2. Commercially Available Elastomers.**

## Chapter 2. Deployable Origami Architectures

In this section, a literature review on existing deployable origami architectures and an investigation of commercial soft materials that can be applied to the origami architectures are presented. A paper Miura origami polyhedron, a paper Yoshimura origami cylinder, and an origami fish base are shown in Fig. 2.1.

### 2.1 Miura Origami Polyhedron

Miura origami is a tessellation comprised only of parallelograms that are patterned in mirror symmetry [98], [99]. When two mirrored Miura origami with the same number of parallelograms are connected along the boundary lines, a polyhedron-shaped origami structure is constructed (Fig. 2.1 (a)). This Miura-ori polyhedron can be rigidly folded into the flat shape of the stacked layers in which each of them consists of two parallelograms. Thus, the Miura-ori polyhedron can be fully defined by three parameters of the parallelogram: the length of each side and the included angle ( $\alpha_M$ ) (Fig. 2.2.). Because of its asymmetric geometry (connected in a zigzag shape), it is possible to make a large deployment ratio.

When a fluidic pressure is applied, Miura-ori polyhedron deploys in a way that maximizes its internal volume. A 1-module Miura-ori polyhedron is

composed of parallelograms with side lengths of  $a_M$  and  $b_M$  and the subtended angle ( $\alpha_M$ ). Let  $\psi_M$  is a half of the included angle of two sides different parallelograms that contact in another side (Fig. 2.2.). The inner volume of the 1-module Miura-ori polyhedron ( $V_M$ ) is represented as follows:

$$V_M = 2a_M^2 b_M \sin \psi_M \sqrt{\cos^2 \psi_M - \cos^2 \alpha_M} \quad (2.1)$$

We can find  $\psi_M$  that maximizes  $V_M$  by differentiating  $V$  with  $\psi_M$

$$\frac{dV_M}{d\psi_M} = 2a_M^2 b_M \frac{\cos \psi_M (2 \cos^2 \psi_M - \cos^2 \alpha_M - 1)}{\sqrt{\cos^2 \psi_M - \cos^2 \alpha_M}} \quad (2.2)$$

$$\cos \psi_M = \frac{\sqrt{2 + 2\cos^2 \alpha_M}}{2} \quad (2.3)$$

When the included angle between the side and a line that equally divides two sides is defined as  $0.5\theta_{Madj}$ , the following condition is satisfied.

$$\cos(0.5\theta_{Madj}) = \frac{\cos \alpha_M}{\cos \psi_M} \quad (2.4)$$

Finally, the angle between the adjacent modules ( $\theta_{Madj}$ ) can be derived as:

$$\theta_{Madj} = 2 \cos^{-1} \left( \frac{2 \cos \alpha_M}{\sqrt{2 + 2\cos^2(\alpha_M)}} \right) \quad (2.5)$$

## 2.2 Yoshimura Origami Cylinder

Yoshimura origami is a famous buckling pattern that appears when an axial compression load is applied to a thin tube-shaped cylinder, in which triangles and inverted triangles are connected continuously [100]. The structure is not rigidly foldable, but can be compressed into the flat shape when made of

compliant materials (e.g. paper, fabric). When folded, the structure, from the top view, is shaped into a polygon surrounded by triangles. The cylinder is radially symmetric, so that its deployment is characterized by linear motion in the height direction. Also, the triangle tessellation can be modified to the trapezoid tessellation (also known as an accordion pattern or a bellows pattern), which is relatively more foldable than the original one (Fig. 2.1 (b)). When all isosceles trapezoid tessellations are designed to be equal, the structure can be fully defined by the length of the upper and lower sides of the isosceles trapezoid and its angle ( $\phi$ ).  $\phi$  is determined by the number of facets ( $N_F$ ) that lie in the same plane when fully folded as follow:

$$\phi = \frac{90^\circ}{n} \quad (2.6)$$

The Yoshimura origami cylinder is not a continuously and rigidly foldable structure (deformation of facets are inevitable for deployment), resulting in a low deployment ratio when made with conventional materials (e.g., papers, fabrics). However, when the entire structure is built with highly flexible or stretchable materials, it can fully deploy into a cylindrical structure because the facets can be easily deformed. The fully folded initial height  $H_{initial}$  and potential fully unfolded height  $H_{unfold}$  of the origami chamber can be defined as follows (Fig. 2.3.):

$$H_{initial} = N_l(h_{g1} + h_{g2} + 2t_w) + t_c \quad (2.7)$$

$$H_{unfold} = H_{initial} + N_l l_c \quad (2.8)$$

Therefore, the deployment ratio  $\lambda$  is derived as:

$$\lambda = \frac{H_{unfold}}{H_{initial}} = 1 + \frac{N_l l_c}{N_l(h_{g1} + h_{g2} + 2t_w) + t_c} \quad (2.9)$$

### 2.3 Origami Fish Base

The origami fish base is originally single-sheet-foldable and generally used as a starting point for origami fish [101]. By folding the reverse side of the origami fish base backward along its center line, we built the shape of a pelican eel with a short triangular mouth and a long triangular jaw (Fig. 2.1 (c)). When the mouth part of the origami structure is pulled up and down, the entire structure unfolds and the facets spread sideways similar to the geometric morphing of a natural eel's mouth in which the jaw spreads sideways during its opening.

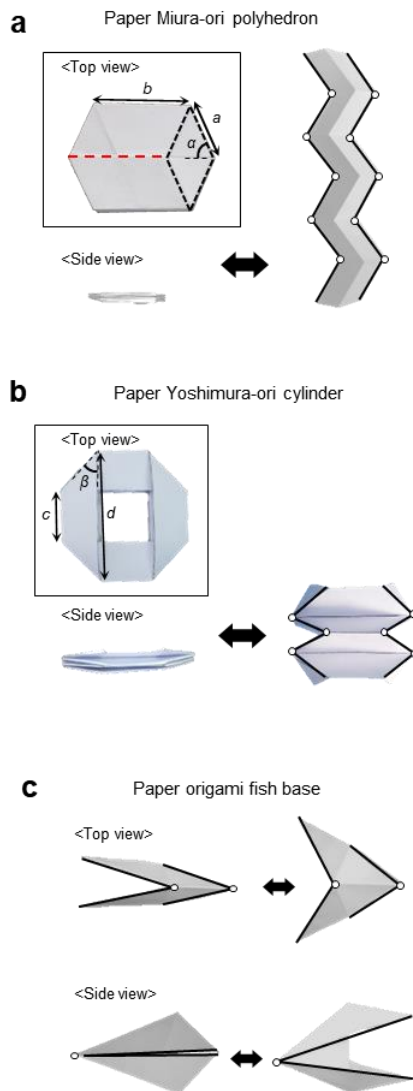


**Fig. 2.1. Paper origami architectures. (a) A Miura origami polyhedron. (b) A Yoshimura origami cylinder. (c) An origami fish base.**

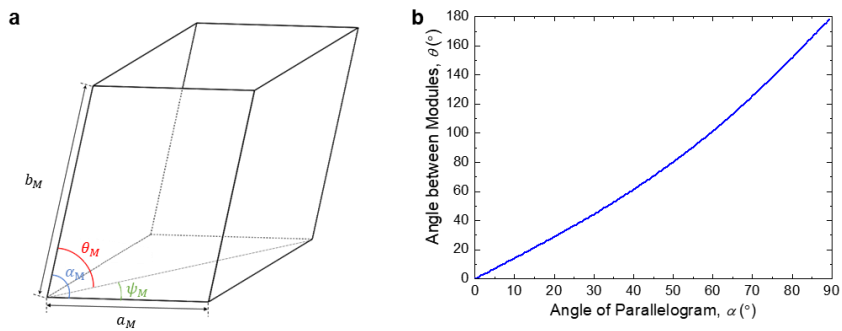


**Fig. 2.2.** A Miura origami polyhedron module. (a) Schematic of a 1-module rigid Miura-ori polyhedron. (b) The deployment behavior of a Miura-ori polyhedron characterized by the angle between adjacent modules ( $\theta_M$ ). Based on the equation,  $\theta_M = 2 \cos^{-1}(2 \cos \alpha_M / \sqrt{2 + 2 \cos^2 \alpha_M})$ , it is noted that the deployment behavior can be defined only by the geometric parameter.

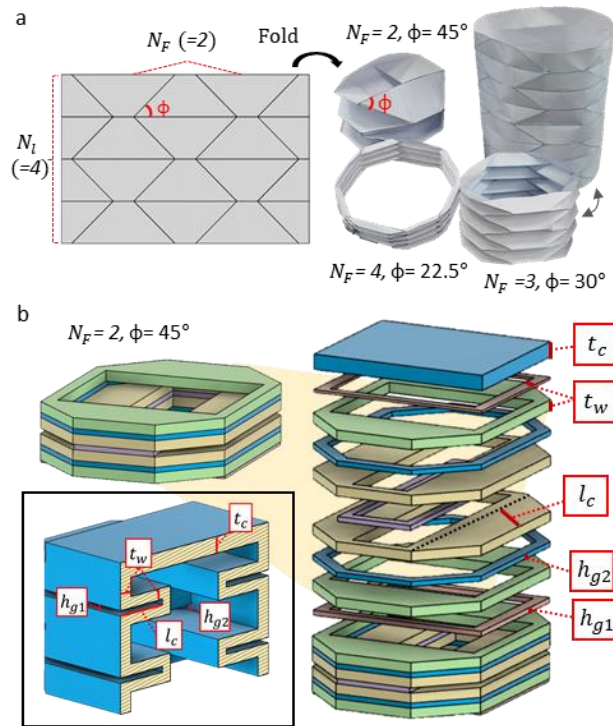


**Fig. 2.3.** Yoshimura origami cylinders. (a) A paper Yoshimura origami pattern (left) and paper Yoshimura origami cylinders with  $N_F = 2, 3,$  and  $4$ . (b) An elastomeric Yoshimura origami cylinder with  $N_F = 2$ . An inset image represents a cross-sectional drawing of an elastomeric Yoshimura origami cylinder.

| Notation        | Definition  |
|-----------------|---|
| $\alpha_M$      | Subtended angle of the Miura-ori parallelogram  |
| $\psi_M$        | Half of the included angle of two sides different parallelograms that contact in another side |
| $V_M$           | Inner volume of the 1-module Miura-ori polyhedron   |
| $\theta_{Madj}$ | Angle between the adjacent modules  |
| $a_M$           | Side length of Miura-ori tessellation   |
| $b_M$           | Another side length of Miura-ori tessellation   |
| $\phi$          | Subtended angle of the Yoshimura origami trapezoid  |
| $N_F$           | Number of facets of Yoshimura origami cylinder that lie in the same plane when fully folded   |
| $N_l$           | Number of layers of the Yoshimura origami cylinder  |
| $H_{initial}$   | Fully folded height of the Yoshimura origami cylinder   |
| $H_{unfold}$    | Fully unfolded height of the Yoshimura origami cylinder                                       |
| $h_{g1}$        | Outside gap length between facets   |
| $h_{g2}$        | Inside gap length between facets  |
| $t_w$           | Wall thickness of the Yoshimura origami cylinder  |
| $t_c$           | Ceiling thickness of the Yoshimura origami cylinder   |
| $l_c$           | Height of a single Yoshimura origami tessellation   |

**Table 2.1. Notations used in chapter 2.**

## Chapter 3. Bioinspired Dual-morphing

### Stretchable Origami (SOrigami)

Adaptive and extreme shape morphing is an elegant solution in nature for adapting to and prospering in surrounding environments [70], [102]–[105]. The naturally organized architectures comprising many life forms often shrink, swell, or deform along prescribed geometric morphology to produce macroscopic unique patterns of movement, exemplified by the origami-like unfolding of swellable ice plants *Delosperma nakurense* [102] or the geometric eversion of the spreading tentacles of terrestrial snails [103]. The underlying principles of such biological morphing behaviors have in many cases been a central design strategy of current artificial shape-morphing systems [106], [107]. In particular, given the complexity of natural morphing principles, efforts to simplify them into ‘monolithic functions’ —such as swelling, skin stretching, origami, kirigami or geometric eversion— enabled successful reproduction of bioinspired morphing mechanisms in artificial system. Pioneering examples included shape-morphing composites encoded with localized swelling anisotropy [108]–[111], soft robots that generate mobility and functionality using sequences of skin stretching driven either by pneumatic

[61], [62], [112], [113] or electrical [20], [22] stimulation, and robotic architectures capable of kinematically guided shape morphing by origami folding [77], [91], [92] or eversion of non-stretchable layers [12]. The results are the unprecedented evolution of the way artificial systems interact with human or sophisticated environments.

Despite the achievements of biomimicry as an engineering solution, there still remains an unexplored regime of natural morphing that cannot be reproduced in artificial system by a monolithic ‘single-mode’ morphing mechanism. For example, recent observation of the *Eurypharynx pelecanoides* (commonly known as pelican eels) shows that the morphing behavior of its inflating head is characterized by two functionally different modes of morphing that first unfolds its mouth and then inflates it to maximize the probability of engulfing the prey. This embodied ‘dual-mode’ morphing is attributed to the coexistence of folded geometry and stretchable skin of the eel’s head structure, which takes both advantages of kinematically guided shape development and adaptability induced, respectively, by unfolding and skin stretching.

In this section, taking inspiration from the design and morphing principle of the pelican eel’s frames, we present entirely soft, dual-morphing architectures that can create quasi-sequential behaviors of origami unfolding and skin stretching in response to fluid pressure. We developed and characterized the

fundamental building blocks (unit cell) of entirely stretchable origami that imitated the role of the pelican eel's stretchable and foldable frames. The soft-bodied architectures, whose embedded fluid paths were defined by the kinematic arrangement of such unit cells, experienced the fluid pressure distribution acting in the direction of deploying the body first and inducing skin stretching, resulting in adaptive and extreme dual-mode shape-morphing. The bioinspired dual-morphing capability of our design rule was verified by reproducing the eccentric dual morphing of a live pelican eel. Using the dual-morphing stretchable origami in combination with traditional origami bases such as Miura origami and Yoshimura origami, we achieved unexplored realms of kinematic features, locomotion and gripping mechanisms, and biomimicry.

### **3.1 A Dual-Morphing Behavior of the Pelican-eel**

The pelican eel *Eurypharynx pelecanoides* is a type of eel with a distinctively shaped mouth that inhabits the deep ocean. We recently spotted and filmed a bizarre-looking pelican eel that morphed in a manner not previously discovered. The eel dramatically transformed the shape of its head from a folded to an inflated state suitable for hunting (Fig. 3.1. (a)). This peculiar pattern of movement is characterized by two functionally different modes of morphing that first trigger body shape development by geometric unfolding and then

create additional motion by the stretching of the constructed body. We found that the unfolding principle of the head follows that of the fundamental origami fish base and, at the same time, it can stretch extremely due to the highly stretchable skin frame Fig. 3.1. (b).

## **3.2 Working Principle of SOrigami**

### **3.2.1 Pelican-eel-inspired Dual-morphing Stretchable Origami**

Inspired by the design and morphing mechanism of the pelican eel's stretchable and foldable frames, we developed synthetic origami units that can be both unfolded and stretched, achieving 'dual-mode morphing' (Fig. 3.1. (c)). A unit cell of the stretchable origami has a C-channel shaped unit geometry that can not only share geometric similarities with conventional origami unit cells (thus able to composite nearly all types of origami architectures), but also be stretched easily. The facets and the crease line of the C-channel unit are made of the same stretchable elastomers, so that deployment relies dominantly on the extreme bending of the facets near the clamped edge (Fig. 3.1. (c)); while, in conventional origami unit cells, the difference in bending stiffness between the crease line and the facets induces unfolding. This C-channel shaped stretchable origami unit cells can be arranged in a manner that forms fluidic channels and chambers, and therefore can use the effect of material stretching for morphing as if a pneumatic network unit is being stretched due to fluid pressure. To

efficiently fabricate 3-dimensional (3D) architectures of unit cells, we developed a new elastomer casting method, termed a ‘layer stacking method’ (Fig. 3.1. (d)). In this method, dozens of flat, water-soluble layer molds (main, separating and cover molds) were stacked together in alternating sequence with pouring of elastomer; and after curing, the resulting structure could be obtained by dissolving the molds in water. The fabricated prototype of the 6-module dual-morphing stretchable origami has a compact initial configuration and illustrates dual morphing response with both unfolding and stretching (inset image of Fig. 3.1. (d)).

The quantitative investigation on this behavior suggested that the dual-morphing behavior can be characterized by the superimposition of the geometry-driven origami unfolding and the stretching of the elastomer. We found that the geometry-driven unfolding could be completed much earlier than the stretching of the elastomer within far low material stresses (Fig. 3.1. (d)). This also indicates that robotic architectures consisting of such stretchable origami linkages can experience high levels of rapid and large-magnitude morphing without losing soft and adaptable properties through the quasi-sequential dominance shift between unfolding and stretching.

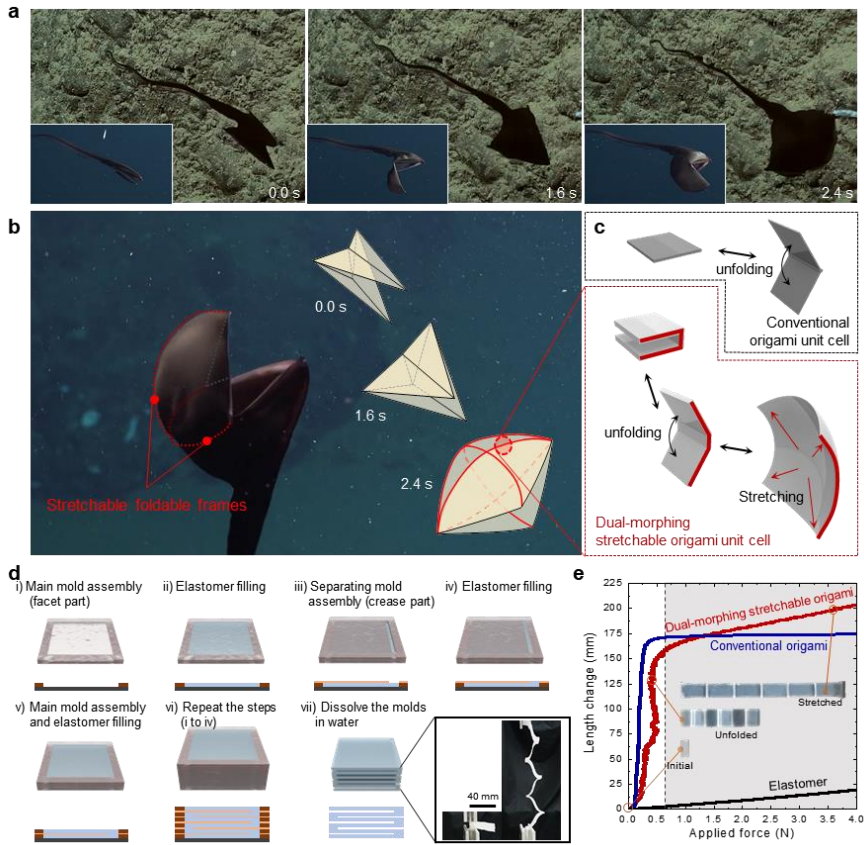


**Fig. 3.1. Pelican-eel-inspired dual-morphing stretchable origami.** (a) The live pelican eel that dynamically extends its mouth. (b) Morphing principle of the pelican eel interpreted by the stretchable forms of origami fish base. (c) The concept of SOrigami. (d) Fabrication. (e) Morphing behaviors of SOrigami, paper origami, and an elastomer unit in response to longitudinal stress in the direction that the system deploys. The inset images indicate the initial, unfolded, and stretched states of SOrigami.

### **3.2.2 Comparison Between SOrigami and Conventional Origami**

Conventional origami consists of easily foldable crease lines with the connected rigid or compliant facets. In general, the bending stiffness of the crease line is engineered to be low enough to be negligible in comparison with the facets. Therefore, rotation occurs intensively at the crease lines when the force is applied to the origami structure, resulting in easy folding or unfolding. Previous approaches to design the low bending stiffness of the crease lines include the use of mechanical hinges, embedment of flexible materials such as fabrics or films, and pre-plastic deformation (e.g., paper folding).

In contrast, our dual-morphing origami is made entirely of soft and stretchable elastomers and facets and crease lines are not distinguished by material stiffness. Because the bending stiffness of both facets and crease lines are very low, facets as well as crease lines would easily fold. Therefore, to create origami-like morphing of entire soft origami architecture, a new design strategy that allows rotation to occur intensively at the crease line similar to the conventional origami should be explored while the unique properties of elastomers (hyperelasticity, high flexibility and stretchability) are also considered in design. Details on the design rule for dual-morphing origami are as follows:

- (i) A crease line of a dual-morphing origami unit cell is defined by a

kinematically arranged C-channel shaped geometry with the clamped facets (Fig. 3.1. (c)). When fluid pressure is applied, the direction of the pressure is distributed preferentially to create rotational moment with respect to the clamped facets. As a result, the unfolding of the dual-morphing origami unit cell, which is induced by the bending of the clamped facets, takes precedence over the stretching (Fig. 3.1. (e)).

(ii) In general, the crease line of conventional origami is designed as a very thin line, thus its thickness (or width) and the corresponding rotational stiffness are considered to be negligible. By contrast, that of dual-morphing origami should be designed to have a sufficient width in order to withstand material stretching when morphing. Therefore, we designed the crease line as a C-channel shaped deployable kinematic structure that has a specific width ( $w$ ), which also affects the rotational stiffness.

(iii) In some cases, the folding of crease lines in conventional origami can be replaced with the bending of flexible facets. Therefore, when designing dual-morphing origamis, it is possible to combine multiple facets into a single facet by removing the crease lines that do not affect the deployment behavior of the dual-morphing origami. In the case of dual-morphing M-ori, for example, bending occurs around the center line of the concave hexagon shaped facets, replacing the function of the original crease lines of the Miura-ori polyhedron.

(iv) Due to the hyperelasticity of elastomers, it is impossible to fabricate dual-morphing origami through pre-plastic deformation by folding. Different from conventional origami that folds in the plane in order to create a three-dimensional structure, dual-morphing origami architectures were fabricated by a ‘layer stacking method’ in which dozens of flat layer molds were sequentially stacked together with the pouring of elastomer.

(v) Elastomeric crease lines of dual-morphing origami have high elasticity. Thus, the energy stored in the crease lines causes the restoring force to return to the initial state when the applied external pressure is removed. The tendency of restoration becomes larger as the width of the crease line, the thickness of the facets, and the stiffness of the material increases.

(vi) Pneumatic actuation intrinsically requires the enclosure of the stretchable origami. Origami geometries that can be easily (or by itself) enclosed such as cylindrical or spherical (e.g. Yoshimura origami cylinder and origami magic ball) and double-layered structures (e.g. Miura-ori polyhedron, double-layered origami fish base) are the representative candidates of the allowable geometry. In addition, the pneumatic actuation is proper for the fully folded geometry of origami in which volume increases as unfolded. As a result, the initial state of dual-morphing origami was formed into a fully folded geometry of parent origami.

### 3.2.3 2D Pseudo Rigid Body Modeling

Given the unit flexible and stretchable plate (elastic modulus:  $E$ , length:  $L$ ) under uniform pressure ( $P$ ), both strain and angle are independent of the length scale based on the following relations:

$$E\varepsilon = P, \quad k_L \Delta L \sim P(L^2), \quad k_L \sim L \Rightarrow \varepsilon \sim L^0 \quad (3.1)$$

$$EI \frac{\partial^2 w}{\partial x^2} = M \sim P(L^3) \Rightarrow \frac{\partial w}{\partial x} \sim L^0, \quad \theta \sim L^0 \quad (3.2)$$

Therefore, if all geometry parameters are equally scaled, the dual-morphing behavior (unfolding and stretching) of the robot built by our design rule would still work equally for the same applied pressure when neglecting the effect of gravity. Because gravity is proportional to the cube of the length scale ( $F_G \sim L^3$ ), it can be inferred that the influence of gravity increases as the scale increases. Accordingly, at very large scales, the entire morphing of the body cannot withstand its own body: this is the typical limitation of entirely soft robots in terms of the scale.

In the case of our dual-morphing origami, the important geometry parameter for the scale issue is thickness. Considering the dual-morphing origami unit cell in which the geometric values are the same but only vary in thickness, the relationship between the stretching and bending changes: as the thickness decreases, bending becomes more preferred to stretching. This is

because bending energy density ( $u_b$ ) is proportional to  $t^3$  while stretching energy density ( $u_s$ ) is proportional to  $t$ :

$$u_b = \frac{Et^3}{24(1-\nu^2)} \left\{ \left( \frac{\partial^2 w}{\partial x^2} + \frac{\partial^2 w}{\partial y^2} \right)^2 - 2(1-\nu) \left[ \frac{\partial^2 w}{\partial x^2} \frac{\partial^2 w}{\partial y^2} - \left( \frac{\partial^2 w}{\partial x \partial y} \right)^2 \right] \right\} \quad (3.3)$$

$$u_s = \frac{Et}{2(1-\nu^2)} (\varepsilon_x^2 + \varepsilon_y^2 - 2\nu\varepsilon_x\varepsilon_y) \quad (3.4)$$

To verify the above results more systematically, we applied Pseudo Rigid Body Model (PRBM) to a simple 2D situation where the C-channel unit structure is subject to uniform pressure (Fig. 3.2. (a)). For simplicity, we assumed that the elastic modulus is constant at low pressure where bending occurs dominantly. The model gives the following two equations (see Fig. 3.2. (b) for the force diagram):

$$k_L \Delta L = \frac{Ewt}{L} \Delta L \quad (3.5)$$

$$k_L \Delta L = p(\gamma L + \Delta L) \sin \theta \cos \theta + \frac{p(1-\gamma)L}{2} \sin \theta \quad (3.6)$$

$$2k_T \theta = \frac{\gamma k_\theta Ewt^3}{3L} \theta \quad (3.7)$$

$$2k_T \theta = p(\gamma L + \Delta L)^2 \left( \cos^2 \theta - \frac{1}{2} \right) + \frac{p(1-\gamma)(\gamma L + \Delta L)L}{2} \cos \theta \quad (3.8)$$

The result shows that bending is much more preferred than the stretching in the early morphing stage ( $0 < P < P_{trans}$ ), and, after the saturation of  $\theta$  near  $45^\circ$ , the stretching occurs dominantly. Using the specific values matched to the experiment ( $L=30$  mm,  $w=30$  mm,  $E=0.9$  MPa,  $t=1.0, 1.5, 2.0$  mm under

the pressure  $P$  ranging from 0 to 10 kPa), we solved the relationship between the bending and stretching and plotted the results as shown in Fig. 3.2. (c) to (e). It is found that bending predominates in the low-pressure regime while stretching occurs across the entire regime of applied pressure, resulting in the quasi-sequential dominance shift between bending and stretching.

In summary, given that the unit cell of the dual-morphing stretchable origami can be considered as a stretchable plate subject to uniform pressure, the unique dual-morphing behavior is generally free from scaling issues when all geometric parameters are equally scaled while neglecting the effect of gravity. However, if the geometric values are constant but only vary in thickness ( $t$ ), bending becomes preferable to stretching as the thickness decreases because bending energy density is proportional to  $t^3$  while stretching energy density is  $\sim t$ . A simple pseudo rigid body model (PRBM) approach also supported the scaling relationship in our dual-morphing origami design.

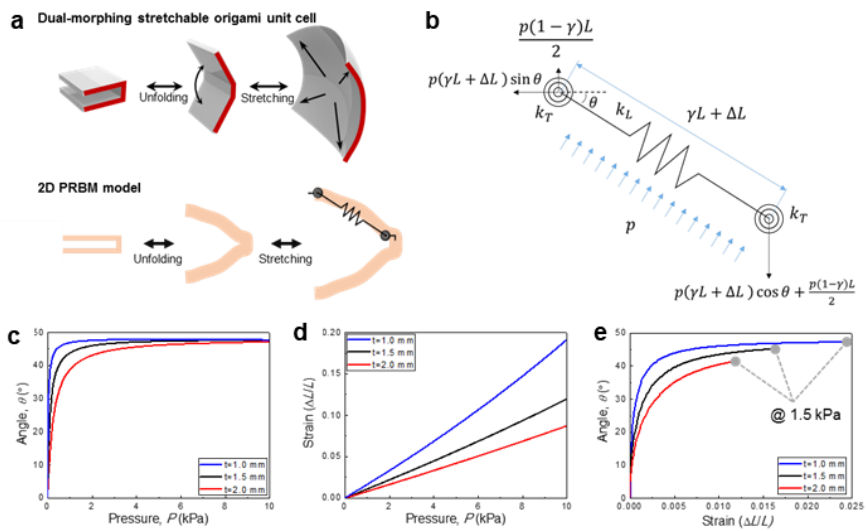


**Fig. 3.2. Scaling relationship of dual-morphing stretchable origami. (a) Basic 2D PRBM model derived from the dual-morphing stretchable origami unit cell. (b) Force diagram of the model. (c) P- $\theta$  relation with increasing thickness. (d) P- $\varepsilon$  relation with increasing thickness. (e) Bending-stretching relationship with increasing thickness.**

### **3.3 Bio-mimicking dual-morphing pelican-eel origami**

To verify the effectiveness of this unconventional but ‘natural’ origami, we built an artificial creature that mimicked the morphing of a pelican eel. The pelican eel’s head can be divided symmetrically up and down against its long mouth, in which each part contains a short snout connected to the long jaws on both sides. The head is found to be an initially folded structure that spreads sideways geometrically when the mouth is opened and finally inflates like a balloon. Since this unique pattern of movement is similar to the development of origami fish base, we built a pelican eel-like soft origami architecture, termed dual-morphing ‘P-ori’, using a double-layered origami fish base structure with embedded fluid paths (the inner layer for the frame and the outer one for the skin) (Fig. 3.3. (a) and (b)). The dual-morphing P-ori was designed to have length ratios in the mouth and jaw parts that correspond to those of the live animal so as to enhance the similarity between the dual morphing profiles. The material for the outer skin was selected to be much softer than that of the inner frame to extend the overlapping regimes of the first (geometry-dominant) and second (strain-dominant) morphing modes. This allows significant body stretching during geometric unfolding as in the case of a live pelican eel (Fig. 3.3. (c) and (e)). The kinematics of the live animal and its artificial analogue was analyzed to verify the successful reproduction of the dual-morphing

principle by tracking the relative displacement of the jaw end point from the top and side view with angles that were taken as close as possible to those for the live eel (Fig. 3.3. (d) and (f), and Fig. 3.4.). The results suggest that our design rule that patterns dual-morphing, entirely stretchable unit cells into the origami base observed in natural life forms adequately imitated the nature's solution to adaptive and extreme shape morphing, although the jaw profile from the side view exhibited slight discrepancy due to the existence of the closing motion.

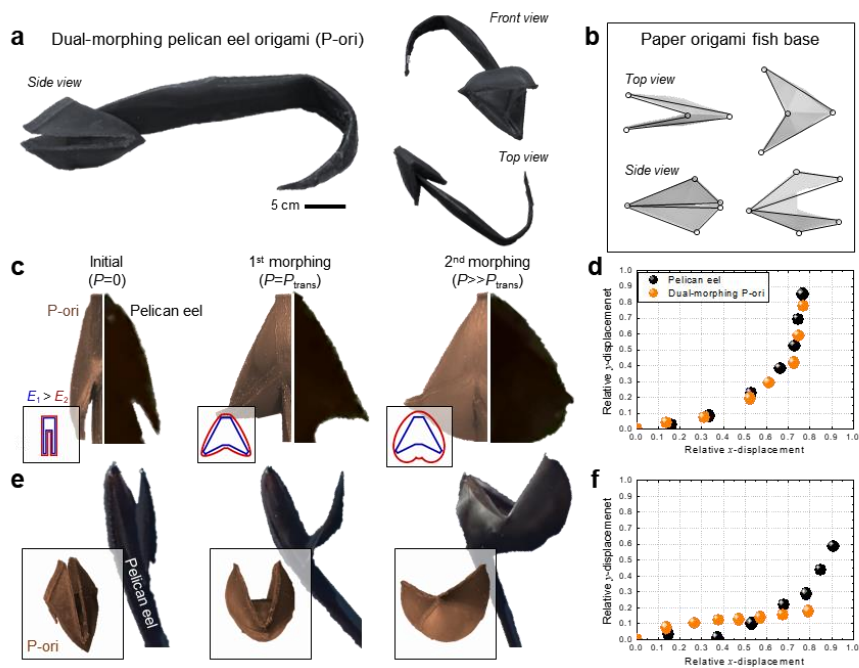


**Fig. 3.3.** A dual-morphing origami architecture mimicking a pelican eel (dual-morphing P-ori). (a) Dual-morphing P-ori built on double-layered origami fish base. (b) Geometric morphing of paper origami fish base. (c and e) Top and side view of the dual-morphing behavior of P-ori (left) and a live pelican eel (right). (d and f) Trajectory of the jaw end point of P-ori and a pelican eel from the top and side view.

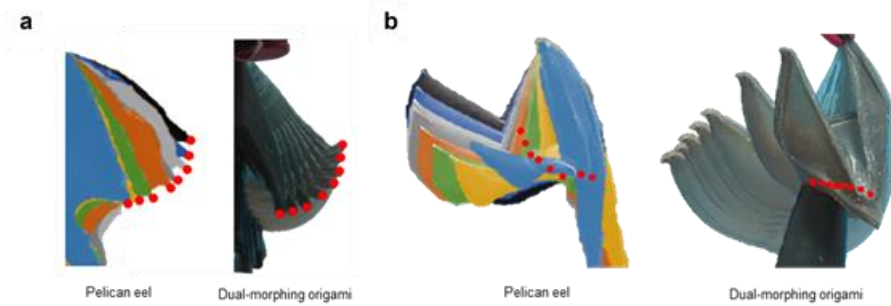


**Fig. 3.4. Kinematics of pelican eel and dual-morphing P-ori. (a and b) Overlaid images of pelican eel (left) and dual-morphing P-ori (right) from the top (a) and side view (b). We particularly focused on the motion of the jaw end point, highlighted by red dots.**

## **3.4 Dual-morphing Miura Origami (M-ori)**

### **3.4.1 Design of M-ori**

The basic origami unit cell originated from the pelican eel's frames can extend the morphing dimension and the corresponding kinematic feature of traditional origami. We demonstrated unprecedented architectures of stretchable origami that achieved extensible kinematic domains in a manner that was previously inaccessible. One typical design is dual-morphing Miura origami (M-ori), which was built on a parent Miura-ori polyhedron (Fig. 3.5. (a)). By compositing dual-morphing origami unit cells in an alternatively stacked manner, we defined the embedded fluidic networks of dual-morphing M-ori. Due to the geometric correspondence with the Miura-ori polyhedron, the dual-morphing M-ori can initially exhibit origami-like morphing that enables rapid, large-magnitude and kinematically defined deployment without structural interference between adjacent facets when unfolded. Additional pressurization causes the morphing mode to be shifted from a geometry-dominant mode to a strain-dominant mode, allowing the robot's body to stretch as a whole and create versatile 'hidden soft robotic' secondary morphing (bending in an inner (M1) or outer (M4, M5) direction, S-shape (M3), and bloating (M2)) along the engineered distribution of the material stiffness (Fig. 3.5. (b) and (c)). Attractive features of this design methodology are that the dual-morphing profile can be designed to (i) have the large-magnitude deployment at a

relatively low-pressure level in comparison with the conventional fluidic bending actuator that utilizes the close proximity of inflation between neighboring chambers (Fig. 3.6.); and to (ii) generate the secondary stretching motion that guides the morphing in the direction different (even normal) to unfolding.

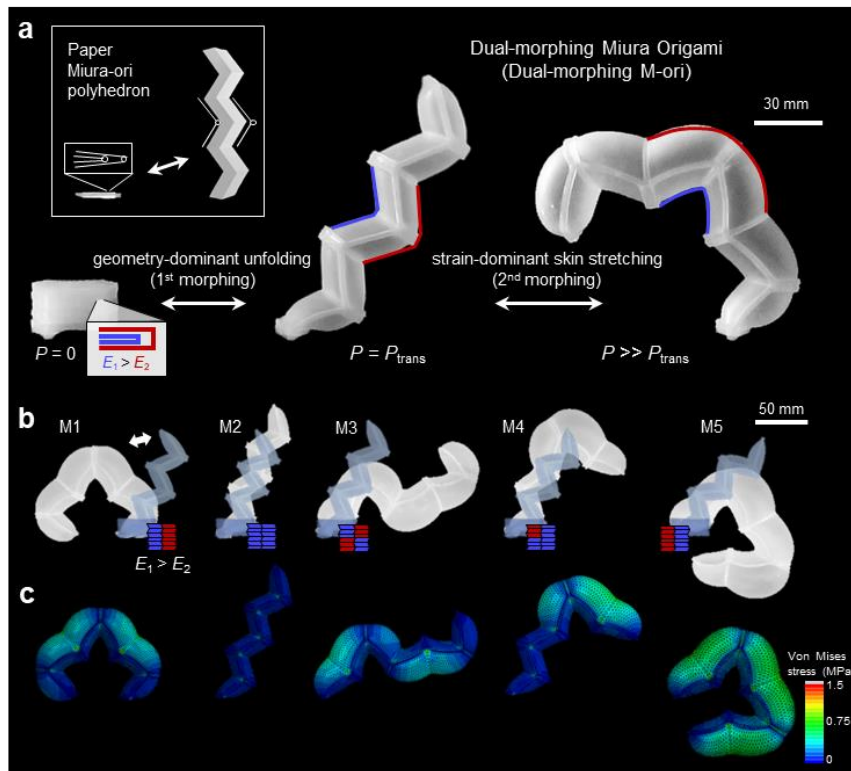


**Fig. 3.5. Dual-morphing Miura origami (dual-morphing M-ori).** (a) Kinematic composition and dual-morphing behavior of 6-module M-ori. Inset image: conventional morphing of a paper Miura-ori polyhedron. (b) Programmable dual-morphing responses of M-ori with distinct material disposition.

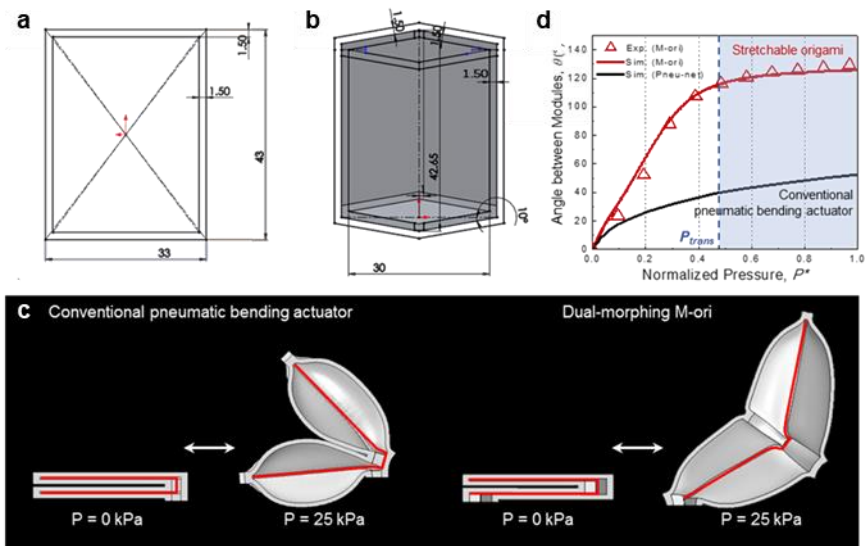


**Fig. 3.6.** Comparison between conventional fluidic bending actuators and M-ori. (a and b) Geometry of a 2-module conventional fluidic bending actuator (a) and a 2-module M-ori (b). The geometric values of both designs were equally defined: 1.5 mm of wall thickness, 30 mm of chamber width, and 40 mm of chamber length. (c) Comparison between bending and unfolding at the same pressure level (25 kPa) based on FEA. (d) Quantitative analysis of dual-morphing behavior of 2-module M-ori in comparison with a conventional pneumatic bending actuator.

### 3.4.2 Definition of the Module, Deployment Ratio ( $\lambda$ ) and Angle ( $\phi$ ) of the Dual-morphing M-ori.

We defined a unit module of dual-morphing M-ori as the structure consisting of a flat hexagon shaped air chamber enclosed by two parallel facets. Multiple modules can be connected via a diamond-shaped end loop of crease lines, so that a multi-module dual-morphing M-ori can be easily formed by stacking. To define the deployment ratio ( $\lambda$ ) and angle ( $\phi$ ) of the dual-morphing M-ori, we expressed the module as a tetragon where its vertexes are located at the joints of the fluidic channel from a cross-section view (Fig. 3.7. (a)). The center of each module, ground, and ceiling are connected in straight segments, and the total length of the line is defined as a length of the robot ( $L$ ). According to the definition, the initial length ( $L_0$ ) is the shortest length from the bottom to top of dual-morphing M-origami, and  $\lambda$  is defined as follows:

$$\lambda = \frac{L}{L_0} \quad (3.9)$$

To define the deployment angle ( $\phi$ ), two points are selected; one from the top facet and the other from the bottom facet of the dual-morphing M-ori (Fig. 3.7. (b)). The point at the top facet is the vertex of hexagon that is farthest from the adjacent air channel, which is the end-point of the dual-morphing M-origami. Another point is a corresponding vertex at the bottom facet. The deployment angle ( $\phi$ ) is defined as the angle between z-axis and the

connected line of the two points, and therefore, according to the definition, the initial deployment angle ( $\phi_0$ ) is  $0^\circ$ .

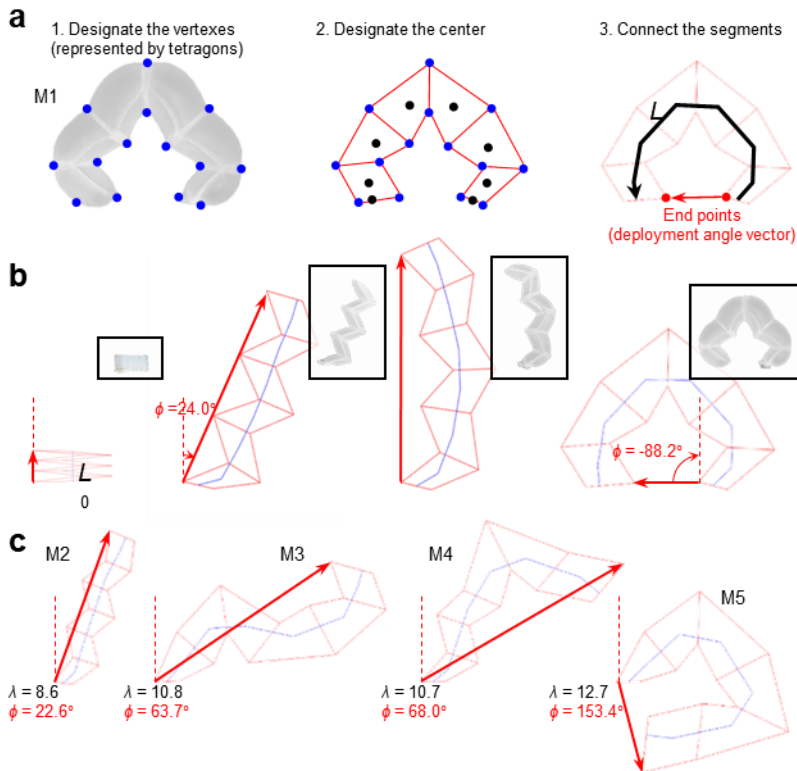


**Fig. 3.7. Deployment ratio ( $\lambda$ ) and angle ( $\phi$ ) of dual-morphing M-ori.**  
**i. (a) A process flow of measuring and calculating the length ( $L$ ) and  $\lambda$  of the dual-morphing M-ori. (b) Definition and measurement of  $\phi$ . (c) Measurement of  $\lambda$  and  $\phi$  of four different dual-morphing M-ori.**

### 3.4.3 Parametric Study

A quantitative study of the dual-morphing behavior was performed for the angle between adjacent modules ( $\theta$ ) and the transition pressure between the two morphing modes ( $P_{\text{trans}}$ ) (Fig. 3.8. (a) and (b)). The experimental and finite element analysis (FEA) simulation results showed that both the dominance between each mode and the unfolding behavior can be determined by the geometric parameters ( $\alpha$  and  $w$  for Miura origami) of the parent origami frame (Fig. 3.9.). The maximum  $\theta$  significantly increases from  $90^\circ$  to  $140^\circ$  as  $\alpha$  increases from  $50^\circ$  to  $80^\circ$  (Fig. 3.8. (a) and Fig. 3.10), while the increase in  $w$  from 0.5 mm to 4 mm changes  $P_{\text{trans}}$  from 2 to 9 kPa (Fig. 3.8 (B)). The approximate time responses of  $\theta$  at each pressure level are shown in Fig. 3.11. On the other hand, skin stretching occurs across the entire regime of applied pressure (Fig. 3.9.), which implies that the superimposition of bending and stretching results in the quasi-sequential dominance shift between the two morphing modes (also described in Fig. 3.1 (e)).

Complex response of the second morphing mode was also investigated for  $\theta$ , deployment ratio ( $\lambda$ ) and deployment angle ( $\phi$ ) (Fig. 3.12.). First, we studied the effect of the distributed stiffness on the morphing behavior of an M-ori unit module based on two elastomer mixtures with a modulus ( $E$ ) difference [(i)  $E_1 > E_2$  and (ii)  $E_1 < E_2$ ] (Fig. 3.12 (a)). It is observed that the stiffness distribution

causes asymmetric bending (inner or outer) of the unit module in the strain-dominant morphing mode while a single-material module [(iii)  $E_1=E_2$ ] experiences uniform bloating (Fig. 3.12. (b) to (d)). Extended to the multi-module dual-morphing M-ori architectures (M1 to M5, depicted in Fig. 3.5.), the coupled dual-morphing responses generated similar deployment vectors ( $\lambda\sim 7$ ,  $\phi\sim 30^\circ$ ) during the first geometry-dominant morphing mode ( $0 < P \leq 3$  kPa); and featured extreme versatile secondary morphing configurations ( $\lambda > 10$ ,  $90^\circ < \phi < 180^\circ$ ), which cannot be derived from the deployment behavior of traditional Miura origami (Fig 3.8. (c) and (d)). The quasi-sequential motion of the bending M-ori is shown in Fig. 3.13. Furthermore, we confirmed that the dual-morphing M-ori could produce a blocked tip force of  $\sim 2.8$  N at  $\phi = 0^\circ$  through the second strain-dominant morphing that moves in the direction different to unfolding, allowing it to function as a soft actuator (Fig. 3.14.).

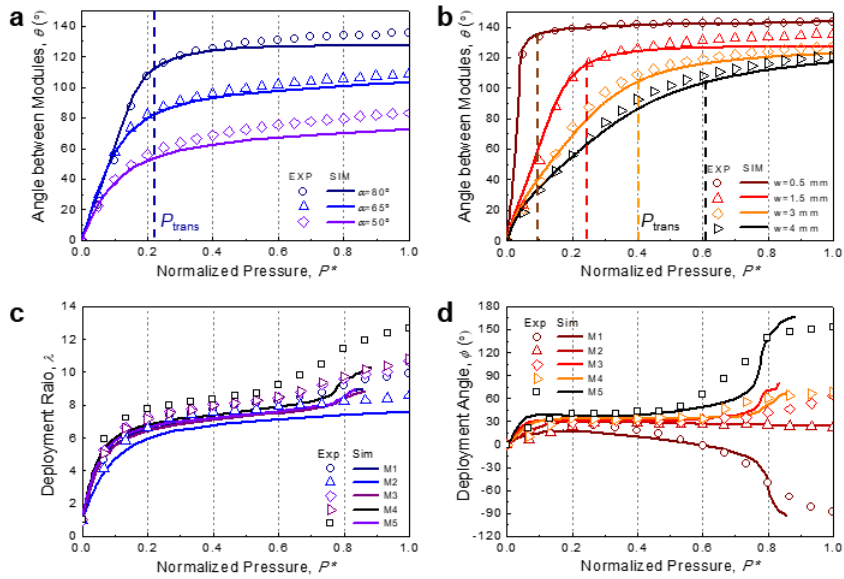


**Fig. 3.8. Parametric study of dual-morphing M-ori. (A and B) Quantitative analysis of dual-morphing behavior of 2-module M-ori for different values of geometric parameters,  $\alpha$  (A) and  $w$  (B). (C and D) Experimental and simulation results of deployment ratio ( $\lambda$ ) and deployment angle ( $\phi$ ) about 5 different dual-morphing M-ori.**

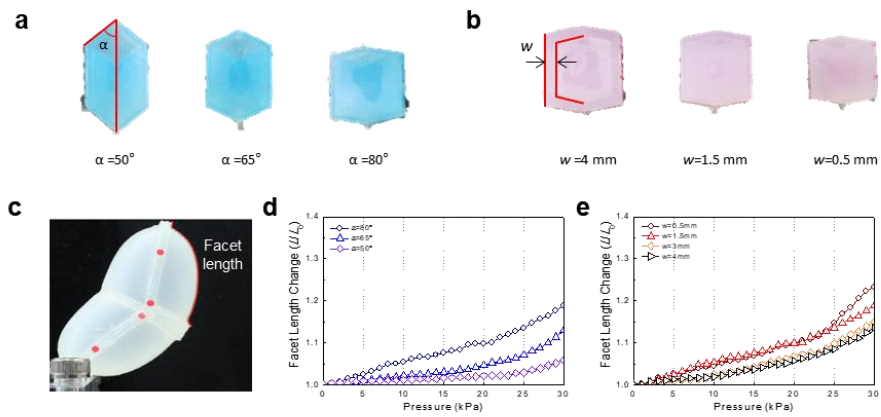


**Fig. 3.9. Parametric study of dual-morphing M-ori. (a and b) Top view of 2-module dual-morphing M-ori with different values of geometric parameters:  $\alpha$  and  $w$ . (c) The result of image analysis measuring the facet length. (d and e) Plot of the facet length change ( $L/L_0$ ) as a function of applied pressure for different values of geometric parameters:  $\alpha$  and  $w$ .**

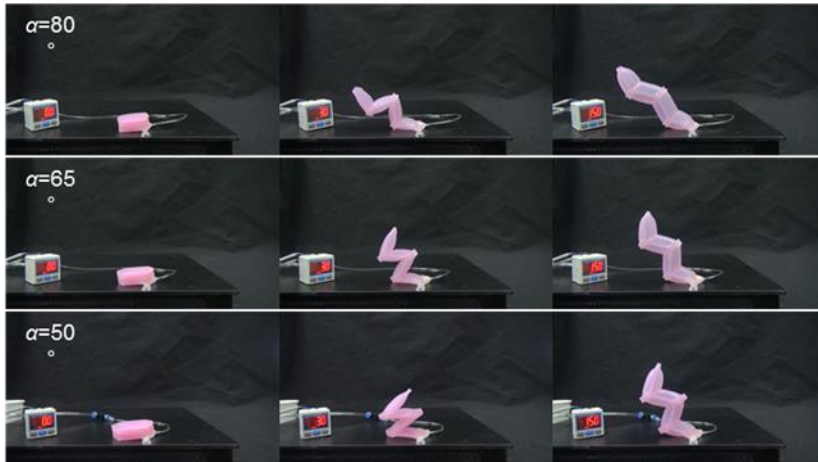


**Fig. 3.10. Geometry-dominant origami-like morphing of dual-morphing M-ori with different  $\alpha$  values. The 4-module dual-morphing M-ori were made of only a single elastomer (DragonSkin 30, Smooth-On).  $\theta$  increases with increasing  $\alpha$  at the same pressure level ( $P=0, 3, 15$  kPa in each step).**

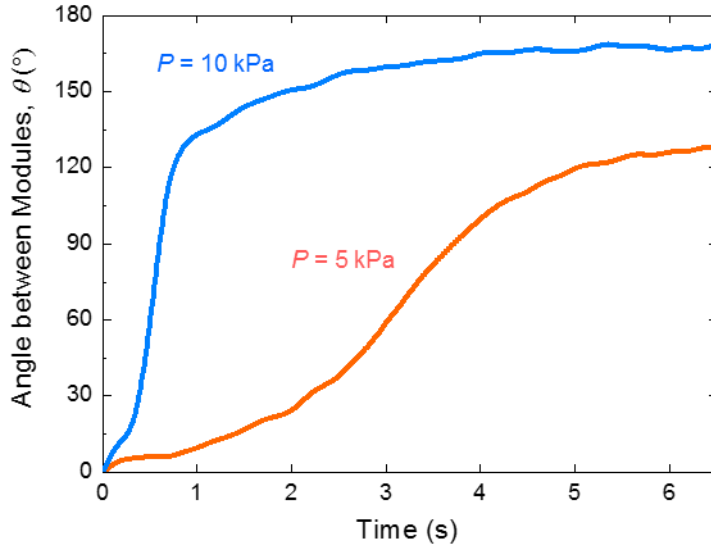


**Fig. 3.11. Dynamic behavior of the 2-module M-ori. The M-ori sample with  $\alpha=80^\circ$ ,  $w=1.5$  mm made of DragonSkin10 and DragonSkin30 was prepared and actuated with constant pressure levels (5 and 10 kPa in this case). As is well known, the time response of such dynamic behaviors varies significantly with the pneumatic source.**

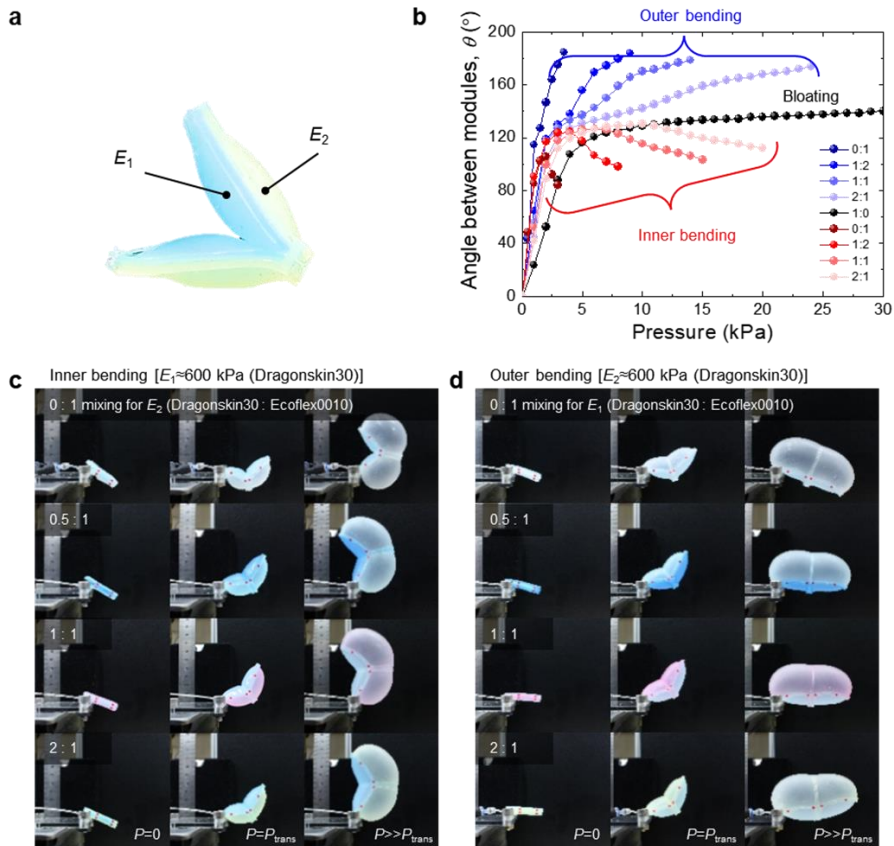


**Fig. 3.12. Strain-dominant soft robotic morphing of dual-morphing M-ori with programmed material disposition. (a) Programmed material disposition in a 2-module dual-morphing M-ori. (b) Dual-morphing response of 2-module dual-morphing M-ori with different material disposition. (c, d) Inner or outer bending of 2-module dual-morphing M-ori in response to continuous fluid pressure.**

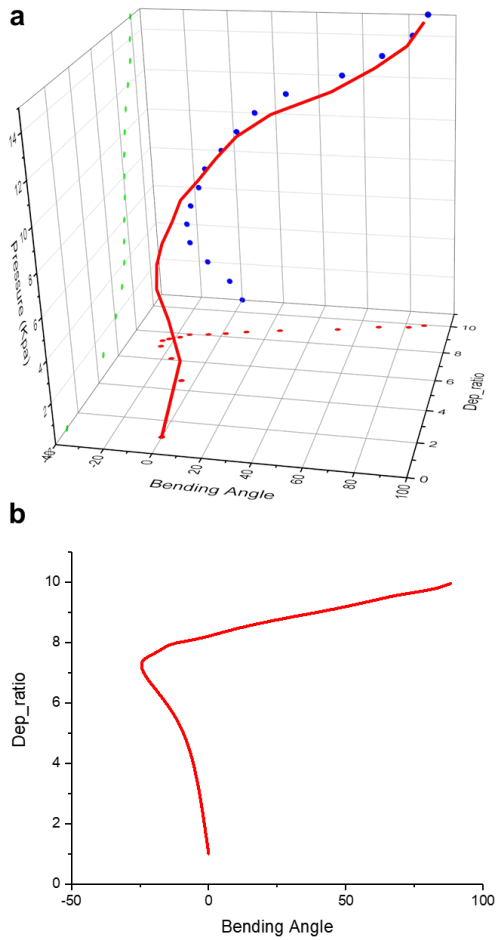


**Fig. 3.13.** The quasi-sequential motion of the bending M-ori. (a) A 3D plot of pressure, bending angle and deployment ratio. (b) Change in bending angle and deployment ratio during actuation.

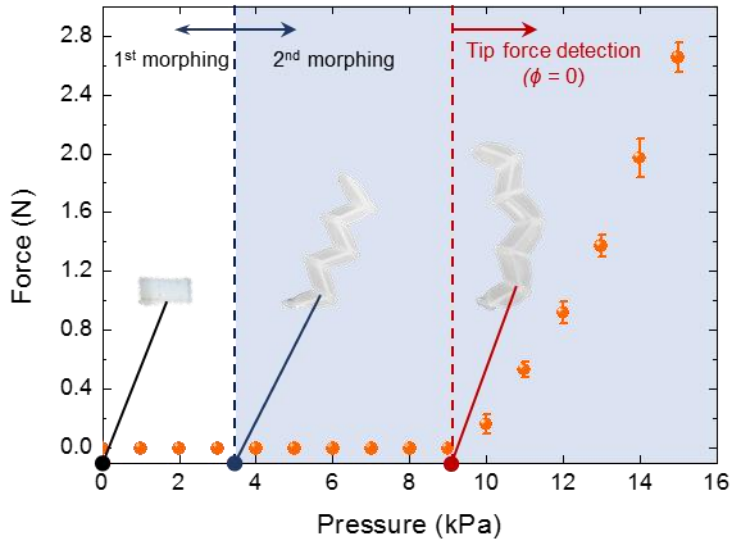


**Fig. 3.14.** Tip force of the 6-module inner bending M-ori. The tip force was measured by the blocked force measurement method (the commonly used method for analyzing the force of soft pneumatic actuators in which its up and down side are blocked by the limiting layer). At the pressure level of ~9kPa, the 6-module M-ori reached the deployment angle ( $\phi$ ) of  $0^\circ$  and the tip force started to be measured, and gradually increased to ~2 N with increasing pressure to 14 kPa (the force of the conventional pneumatic actuator varies from one to tens of N, depending on the design, scale and materials).

### 3.4.4 Soft Robotic Applications of Dual-morphing M-ori

The dual-morphing M-ori showcases a previously unexplored class of morphing behavior in soft robotic applications. To exemplify the potential functionalities such as initial compactness and deployment-combined adaptive morphing, we demonstrated unconventional gripping and locomotion mechanisms, and a soft machine that can cover a wide field of vision underwater (Fig. 3.15). First, we constructed a deployable soft gripping system using three 6-module dual-morphing M-ori in which the second morphing mode was regulated for inner bending. The ability to change their length extremely from an initially compact design allowed the system to be portable (Fig. 3.16.) or easily concealed inside their surrounding environment such as in a heap of sand (Fig. 3.15. (a)). It could protrude from the sand through origami-like morphing ( $<0.4$  s) and subsequently actuate towards  $\phi=-90^\circ$  to grasp a fast-moving object softly but robustly (Kamigami Robot bug, Dash Robotics Inc.) ( $<1.3$  s).

Another cooperative dual-morphing strategy enabled a robotic crawler to embody deployment-combined locomotion (Fig. 3.15 (B)). We demonstrated the soft crawling robot consisting of four 4-module dual-morphing M-ori to verify the enhanced mobility (or even portability) of soft robots based on our approach. The deployable soft crawler could first develop its shape to be ready

for locomotion and crawled via repeated transitions in the second morphing mode of soft robotic bending motion.

Further extreme shape morphing was showcased by a robotic eye tentacle consisting of a 12-module dual-morphing M-ori (Fig. 3.15 (C)). Inspired by the eye tentacle of terrestrial snails that make a better field of vision using a dual-morphing mechanism, the robot was designed to enable extreme lengthening (more than fifteen times its initial height of 36 mm) and bizarre-looking quivering by programmed material disposition (Fig. 3.17. for the architecture of material stiffness distribution in the soft robotic eye tentacle). In addition, a wireless camera (GoPro Hero5 Session) was equipped to provide vision. Accordingly, the images captured by the robotic tentacle were collected from the deep bottom to the outside of the water. Subsequently, the embodied dual-morphing capability enabled the robot to cover a wide field of vision underwater via repeated secondary morphing (Fig. 3.15 (D)).

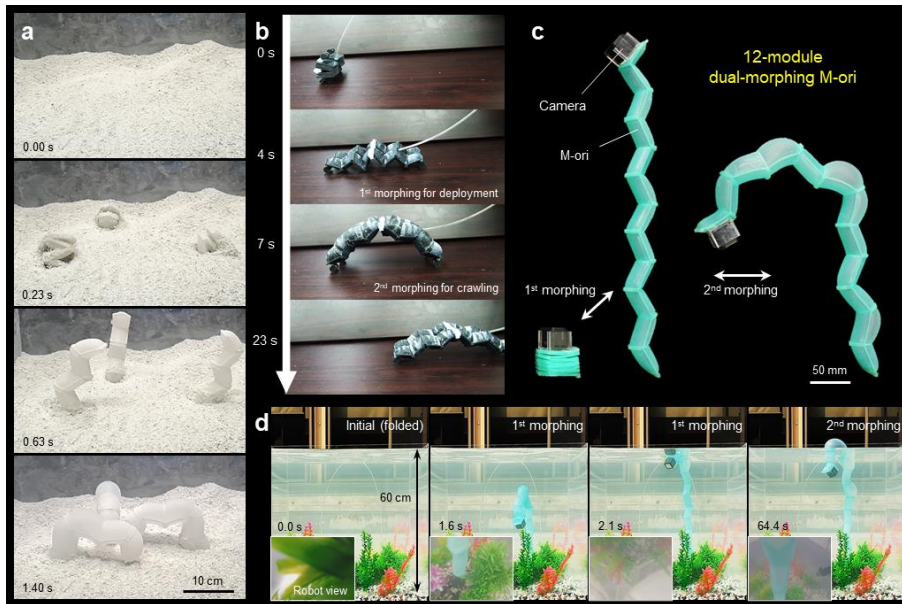


**Fig. 3.15. Soft robots consisting of dual-morphing M-ori. (a) The unique behavior of dual-morphing M-ori features initial compactness (thus capable of being concealed in a heap of sand), rapid deployment ( $<0.4$  s), and adaptive, functional morphing. (b) A soft crawling robot consisting of four 4-module dual-morphing M-ori demonstrates deployment-combined crawling locomotion characterized by the repeated transition in the second morphing mode. (c) A soft robotic eye tentacle consisting of 12-module dual-morphing M-ori and a wireless camera. (d) The robot's extreme shape changing capabilities can cover a wide field of vision.**

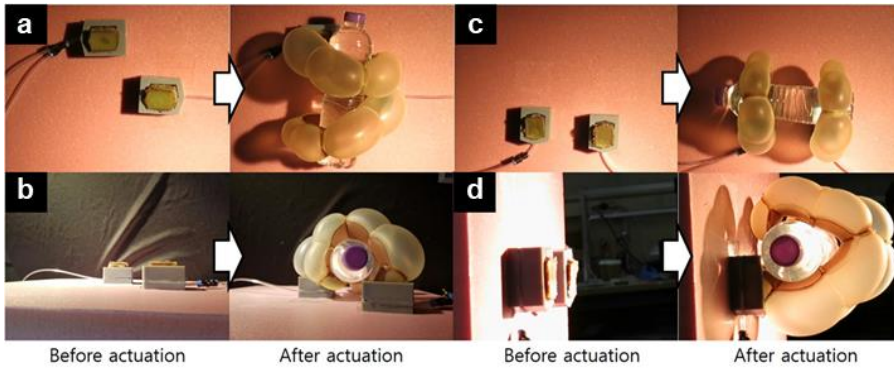


**Fig. 3.16.** A dual-morphing M-ori gripper. (a and b) A dual-morphing M-ori gripper that hugs an object, taken from a top (a) and a side view (b). (c and d) A gripper that supports an object, taken from a top (c) and a side view (d).

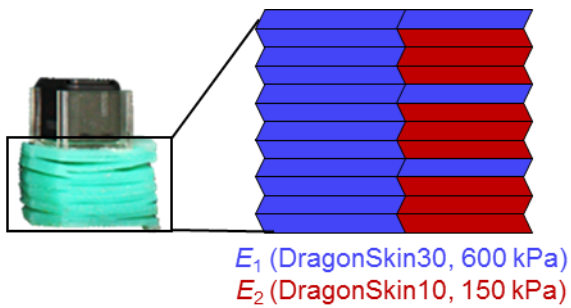


**Fig. 3.17.** Architecture of material stiffness distribution the soft robotic eye tentacle.

## **3.5 Dual-morphing Yoshimura origami (Y-Ori)**

### **3.5.1 Design of Y-ori**

Similar to the dual-morphing M-ori, the stretchable origami unit cells were composited based on the parent Yoshimura-ori cylinder. The resulting dual-morphing origami architecture, termed ‘dual-morphing Y-ori’, has strengths in symmetric growing and programmable bloating (Fig. 3.18. (a)). The dual-morphing Y-ori was fabricated by arranging a set of dual-morphing origami unit cells mirror-symmetrically. Similar with other dual-morphing origami architectures, the quasi-sequential morphing is a key mechanism that shifts dominance from geometry-dominant shape development in the height direction ( $\lambda \approx 4.5$  for 4-module architecture) to strain-dominant asymmetric bloating ( $\lambda \approx 5.5$ ) (Fig. 3.19.). The feature that grows symmetrically in the height direction could be integrated into other dual-morphing behaviors, leading to a class of soft robots capable of versatile, adaptive, and human-interactive tasks (Fig. 3.20.).

### **3.5.2 Y-ori Deployable Caging Gripper**

To further demonstrate the benefits of the dual-morphing Y-ori, we developed a deployable soft caging gripper that exploited dual morphing for universal grasping in a previously inaccessible manner (Fig. 3.18 (B)). The gripper was made from two dual-morphing Y-ori with different radii and material stiffnesses.

In particular, the stiffness of the inner cylinder was designed to be lower than that of the outer one for asymmetric bloating. The two quasi-sequential morphing modes are functionally separated in terms of grasping ability: the first mode triggers only a body length change ( $\lambda \approx 3.1$ ) and the second mode performs the task of grasping by reducing the inner area of the gripper to enclose the object (Fig. 3.18. (C) and (D)). Compared to the existing mechanisms of universal soft grippers that used granular jamming [44], finger grasping [61] and suction [114], the dual-morphing mechanism allowed the gripper to grow toward the object, enclose it, and hold it. This unique gripping behavior has the advantages of protecting the object from external impact and enabling a 5-Kg-heavy object to be held stably. It also demonstrated universal gripping irrespective of the shape of objects (Fig. 3.18 (E)).

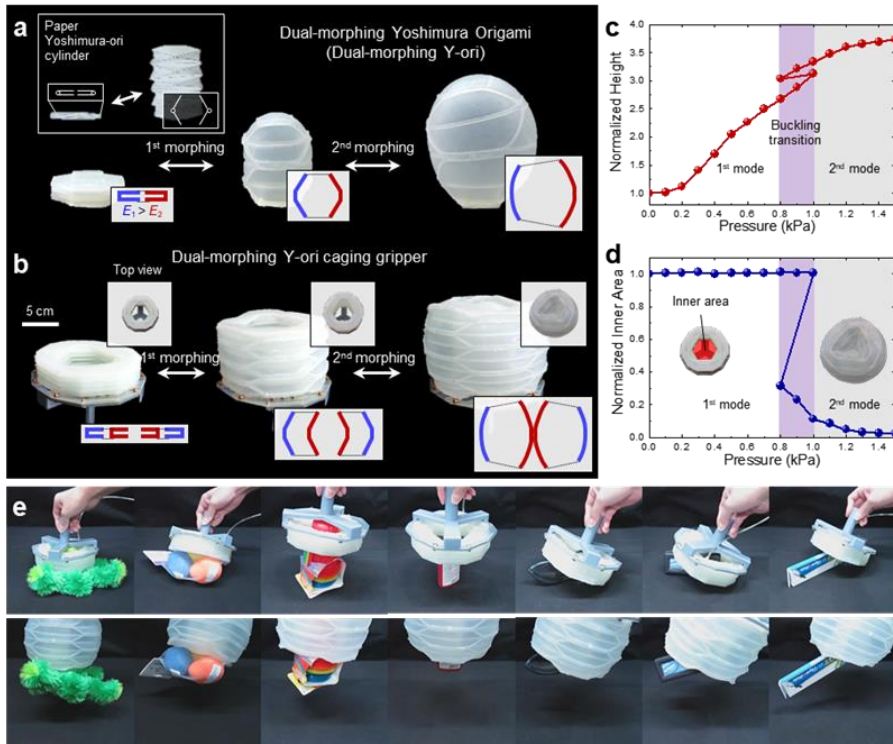


**Fig. 3.18. Dual-morphing Yoshimura origami (dual-morphing Y-ori).**

(a) Dual-morphing response of 4-module Y-ori under fluidic pressurization compared with that of a paper Yoshimura-ori cylinder. (b) Morphing behavior and mechanism of the dual-morphing Y-ori caging gripper. (c and d) Characterization of dual morphing of the Y-ori caging gripper. While the gripper grows in the height direction with increasing applied pressure, the inner area reduces only during the 2<sup>nd</sup> morphing mode. (e) Universal dual-morphing gripping of irregular-shaped objects.

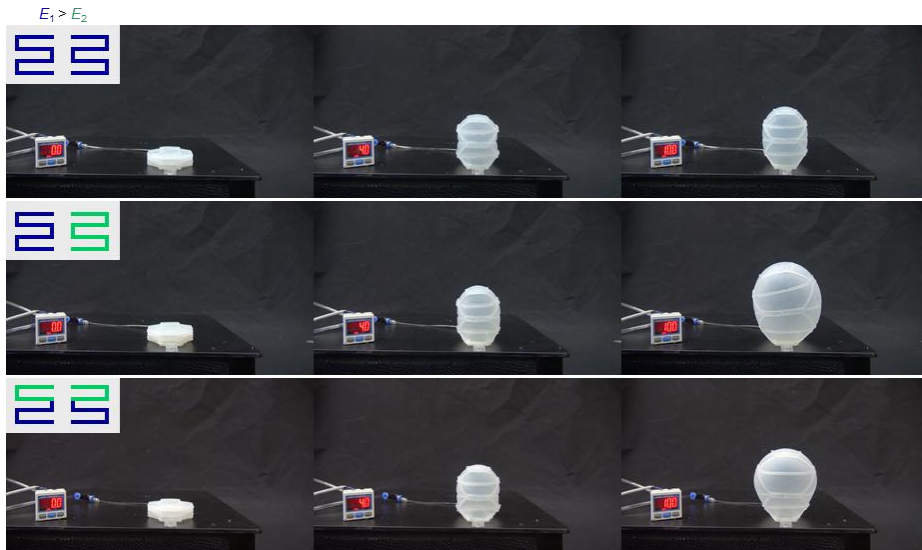


**Fig. 3.19. Dual-morphing Y-ori with programmability. Two different elastomers [DragonSkin30 ( $E_1 \sim 600$  kPa) and DragonSkin10 ( $E_2 \sim 150$  kPa)] are patterned differently with the same geometry in order to show multiple dual-morphing responses of 4-module Y-ori.**



**Fig. 3.20.** A dual-morphing human-interactive soft robot. (a) The soft robot consists of a 7-module dual-morphing Y-ori (body) and two 4-module dual-morphing M-ori (arms) with a 3D printed rigid frame. The robot uses dual-morphing for both body development and hugging. (b) A dual-morphing behavior of the robot that hugs and lifts a doll using its arms and the body.

## **3.6 Materials and Methods**

### **3.6.1 Materials for SOrigami**

The dual-morphing origami was made of silicone rubbers or rubber-like 3D printed materials. Commercially available highly soft and stretchable rubbers Dragonskin™ 10 and 30 (shore hardness A10 and A30, elongation at break of 1000% and 364%, respectively, Smooth-on Inc.) and Ecoflex™ 0010 (shore hardness 0010 and 800% of elongation at break, Smooth-on Inc.) were used for casting. The silicones are originally translucent white, but we used Silc Pig™ (Smooth-on Inc.) to color them if necessary. The 12-module dual-morphing M-ori was colored green and the dual-morphing P-ori was colored black. For multi-material 3D printing, a rigid material ‘VeroWhitePlus™’ (shore hardness 85D, Stratasys, Ltd.) and a rubber-like material ‘TangoBlackPlus™’ (shore harness A27 and elongation at break of 218%, Stratasys, Ltd.) were used. The shore hardness of each part of the dual-morphing origami could be controlled from 27A to 95A by changing the composition ratio between the two materials selectively. For the demonstration of the 3D printed dual-morphing M-ori utilized for a soft crawler, we selected TangoBlackPlus™ for the part of the stretchable facets and FLX9840-DM (shore hardness A35-40) for the part of the relatively stiff facets. All dual-morphing origami architectures were connected to 1.8-mm-diameter polyurethane tube (MPUT1.8-10-C, MISUMI) for fluidic actuation.

### 3.6.2 Layer Stacking Method for Fabrication

A new fabrication technique called a ‘layer stacking method’ was developed that can build a soft robot architecture with complex embedded fluid channels. In this method, dozens of flat layer molds (thickness=0.5 or 1 mm) were sequentially stacked together with the pouring of elastomer. We classified the layer molds into three types: a ‘main layer mold (M-mold)’, a ‘separating layer mold (S-mold)’ and a ‘cover mold (C-mold)’. The M-mold defines the shape of the main facets (and associated crease lines) of dual-morphing origami, which form origami tessellation. The S-mold, which is stacked between the two M-molds, defines the crease lines that not only separate the facet portion but also connect the crease portion. The C-mold defines the floor and cover of the completely stacked mold. All molds have holes at the sides for alignment.

The molds were made by the 3D printing of a water-soluble material PVA+(eSUN) or the laser cutting (VLS 3.5; Universal Laser System) of thin acrylic plates or paraffin wax plates with the thickness of 0.5 mm (S-mold) and 1 mm (M-mold and C-mold). After the layer molds were fabricated and coated with a silicone release agent (Ease Release 200, Mann Release Technologies, Inc), the following molding processes were carried out: First, the C-mold was placed at the bottom with pins for alignment and the M-mold was stacked on it (Fig. 3.1 (d), i and Fig. 3.21. (a)). A liquid-phase elastomer was poured into the

M-mold (Fig. 3.1 (d), ii and Fig. 3.21. (b)), and then the S-mold was carefully covered over the M-mold and filled with an elastomer (Fig. 3.1 (d), iii and iv, and Fig. 3.21. (c) and (d)). In the same manner, the sequential process of stacking the M- mold, pouring a liquid-phase elastomer, and covering with the S-mold was repeated (Fig. 3.1 (d), v and vi, Fig. 3.21. (e)). When the layers were totally stacked up, the C-mold was placed on the top to finish the process (Fig. 3.21. (f)). The stacked layer molds were placed in an oven for 1 hours at 65°C. After the elastomer was fully cured, the bridges were cut and the inner and outer parts of the layer mold were disconnected. Subsequently, the soluble molds (made of PVA+) were dissolved in the 70°C water with a magnetic stirring process for 8 hours (Fig. 3.1 (d), vii and Fig. 3.21. (g)). When insoluble molds (acrylic plates) were used, the molds were physically removed while the material and the structure often underwent large mechanical stress and undesired deformation. Finally, the remaining structure was sealed using a half-cured elastomer or a silicone adhesive (Sil-poxy, Smooth-On, Inc.) (Fig. 3.21. (h)). Since the width of voids of the S-molds was narrow within a few millimeters, the elastomer placed underneath the mold did not mix with that placed at the upper side of the mold. Therefore, different elastomers could be patterned individually for each M-mold, which means that stiffness could be spatially distributed for each layer. Excluding mold fabrication time, the whole

process could be completed within 12 hours and most of the process did not require any manual labor.

We also used an Objet 260 Connex multi-material printer (Stratasys Ltd.) to directly fabricate the dual-morphing origami architectures. Since the multi-material 3D printer could combine two different materials to meet the desired shore A hardness ranging from 27 to 95, we could build the soft facets with different stiffnesses to design programmable motions. This direct method enabled us to fabricate non-flat foldable origami structures, such as the Kresling pattern and the origami magic ball, in which the folded geometry of the facets is not parallel to the base surface (thus difficult to fabricate by the layer stacking method). Although 3D printing enabled direct printing of complex and multi-material origami structures, it has several drawbacks such as limited material availability, high price, and difficulty in mass production. Further, the elongation ratio of TangoBlackPlus was much lower than that of highly stretchable elastomers used in a layer stacking method (elongation limit ~1000%), resulting in poor repeatability and robustness.

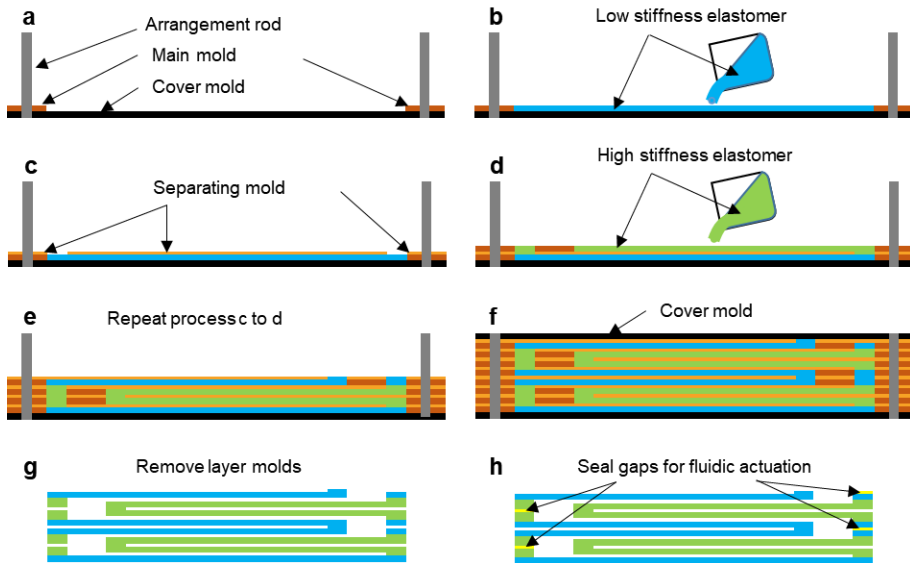


**Fig. 3.21. Fabrication process of dual-morphing origami architecture s: a layer stacking method. (a) Put a cover mold at the bottom and align a main layer mold. (b) Pour uncured low stiffness elastomer. (c) Place a separating layer mold. (d) Place a second main layer mold and pour uncured high stiffness elastomer. (e and f) Repeat the process from c to d for the stacking of 2- (e) and 4-module (f). Finally, place a cover layer mold to finish the stacking process. (g) Remove all layer molds. (h) Seal the cured structure using a half-cured silicone or a silicone adhesive.**

### 3.6.3 Experiment, Simulation and Analysis

The actuation of dual-morphing origami architectures was carried out by a tethered pneumatic source. A compressor or a fluidic pump was used as an air source and fluids were applied into dual-morphing origami through urethane tubes with the diameter of 1.8 mm. The applied pressure was regulated precisely by a pressure regulator and solenoid valves. The level of pressurization subjected to dual-morphing origami was measured by a pressure sensor.

Image analysis was performed to extract data from the experiments. We attached red markers at dual-morphing origami (Fig. 3.22. (a)). The center positions of the attached markers were found by MATLAB function 'imfindcircle' and by the codes that filtered the mistaken circles by RGB data (Fig. 3.22.). The relative coordinates of the markers were used to calculate the angle between adjacent modules ( $\theta$ ), deployment ratio ( $\lambda$ ) and angle ( $\phi$ ). The length change of the facet was obtained by analyzing the color difference from the background; we manually selected two points and then MATLAB calculated the length of the arc between the points. The inner area of the dual-morphing Y-ori caging gripper was also calculated by converting the captured images into binary ones (0, black and 1, white) and finding the number of '0' pixels.

The non-linear FEA was performed using commercial FEA software ABAQUS (Dassault systems). Material properties used in FEA (Dragonskin 30, Dragonskin 10, and Ecoflex 0010) were obtained totally from uniaxial tension tests and volumetric tests. In the software, materials were considered as a Yeoh hyperelastic material model which was matched well with the experimental results. To make the same condition with the actual experiments for the dual-morphing M-ori, the diamond shaped fluidic channel of the bottom surface was set to a fixed boundary condition. For every case, the applied pressure was set to increase linearly and a contact condition was a ‘general contact’. Positions of the desired nodes were collected to evaluate the angle between modules ( $\theta$ ), deployment ratio ( $\lambda$ ) and deployment angle ( $\phi$ ).

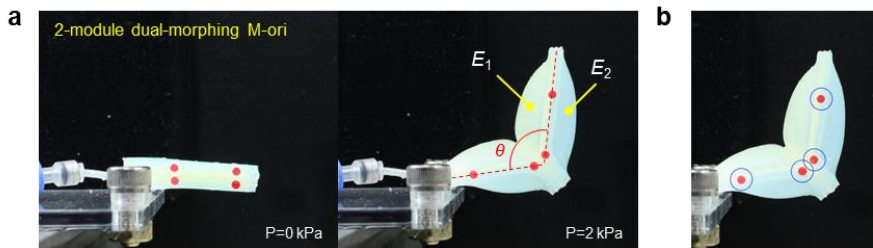


**Fig. 3.22. Image analysis process. (a) Experimental setup for the investigation of the morphing behavior of 2-module dual-morphing M-ori. Red markers are attached for image analysis. (b) The result of image analysis finding the positions of the red markers.**

### **3.7 Discussion**

Stretchable origami frames found in nature intrinsically embody two functionally different morphing mechanisms, unfolding and stretching. We have shown that the entirely stretchable origami unit cell is the fundamental building block of the dual-morphing mechanism that is the nature's solution to adaptive and extreme shape morphing. We demonstrated some prototypes of kinematic arrangements of the unit cells for pneumatically driven dual-morphing architectures. Although made entirely of stretchable elastomers, these robotic architectures could experience rapid, large-magnitude and kinematically defined deployment at low material stresses during the first morphing mode, suggesting a new paradigm in architecting adaptive and extreme shape-morphing system. The possibility of sharing a wide range of origami design pools including well-known Miura and Yoshimura origami as well as origami bases existing in nature enabled us to readily illustrate the versatility of artificial dual-morphing systems. Our approach offers a new platform for the material architecture and shape-morphing system that can potentially be used to realize bioinspired morphing mechanisms, portable soft robots, biomedical devices and active metamaterials.

| Notation    | Definition   |
|-------------|--|
| $\lambda$   | Deployment ratio of the dual-morphing M-ori        |
| $\phi$      | Angle of the dual-morphing M-ori                   |
| $L$         | Effective length of the dual-morphing M-ori        |
| $V_M$       | Inner volume of the 1-module Miura-ori polyhedron  |
| $\theta$    | Angle between the adjacent modules                 |
| $P$         | Applied pressure                                   |
| $P_{trans}$ | Transition pressure between the two morphing modes |
| $\alpha$    | Subtended angle of the Miura-ori parallelogram     |
| $w$         | Crease line width of the dual-morphing M-ori       |

**Table 3.1. Notations used in chapter 3.**

## **Chapter 4. Application: Deployable Soft Pneumatic Networks (D-PneuNets) Actuator with Dual-morphing Origami Chambers**

Soft pneumatic actuators have been widely adopted for applications that require delicate interactions with humans or the environment, due to their intrinsic safety originated from soft matters such as elastomers [62], films [115], [116], and fabrics [117]–[122]. The most typical form factor of soft pneumatic bending actuator is the soft pneumatic networks actuator (also widely known as 'PneuNets actuator' [62]). Soft pneumatic networks actuators are in a shape of inflatable chambers arranged in a row (pneumatic networks) above a strain-limiting layer that inextensible flat strip (e.g. paper, fabric, film) is embedded, and they produce continuous bending motion through (i) an asymmetric lengthening of the inextensible layer and extensible pneumatic networks and (ii) mutual contacts between pneumatic chambers.

The bulkiness and the output force of the soft pneumatic networks actuator is in a trade-off relationship because the moment produced by extension or interactions of/between the pneumatic chambers is proportional to the square of the height of the chambers [123]. Consequently, to ensure efficient power,

the soft pneumatic network actuators are either (i) designed as bulky and highly stretchable silicone beam structures consisting of tall pneumatic chambers or (ii) designed to hold high pressure by making them flexible but less-stretchable by using fabrics, thermoplastic polyurethanes (TPUs) [124]–[128], or fiber-reinforcement (a method that constrain excessive stretching of materials and guide the motion [94], [129]–[131]). In the former case (case(i), the elastomeric zHowever, the bulkiness limits the compact designs of robotic systems, and may cause inconvenience to users, particularly when not in use, in applications where physical interactions between human and robot are required (e.g. wearable devices). In the latter case (case ii), on the other hands, the actuators can be built in non-bulky form. However, these actuators require high pressure input ( $>100\text{kPa}$ ) because of relatively high elastic modulus or the appendages limit the bending capability. Researchers have enhanced the performance of these actuators by introducing novel design of pleats for lateral motion [120], [125], yet still not challenging for the trade-off relationship of bulkiness and output force that may enhance the performance dramatically.

In this section, we developed a deployable soft pneumatic networks actuator (D-PneuNets) with origami structured pneumatic chambers that can deploy in the height direction. Made of stretchable elastomers, the deployable chambers undergo dual-morphing behavior including early origami-unfolding based

morphing and late stretching based morphing, as discovered in Chapter 3. As a result, the D-PneuNets actuator is initially in a compact and flat form that the pneumatic chambers are fully folded when not in use, then its chambers grow more than 2.5 times in the height direction to increase the moment arm at a low applied pressure, and finally inflate to generate high force. Our design concept was verified through the comparison of output force with the conventional soft pneumatic networks actuator, and also characterized through experimental study and finite element method (FEM). Using D-PneuNets actuators, we developed a robotic soft glove that is compact when not in use, and demonstrated that it can generate enough power to grip various objects.

#### **4.1 Design of the D-PneuNets Actuator**

The deployment and bending behavior of the D-PneuNets is shown in Fig. 4.1. Its key design difference with the conventional pneumatic networks bending actuator is that the deployable pneumatic chambers are structured as a modified Yoshimura origami cylinders. For the D-PneuNets origami chambers, the minimally complex case of the Yoshimura origami cylinder  $N_F=2$  and  $\phi_Y$   $45^\circ$ ) was chosen because of (i) the potential large deployment ratio by large facets, (ii) the axial symmetry that linearly and symmetrically transmit force, and (iii) relatively simple fabrication comes from the simplicity of the structure

with the minimum number of facets.

When the pneumatic pressure is applied into the elastomeric origami chambers, both unfolding and stretching occurs simultaneously. At a low applied pressure level, however, the unfolding is the dominant morphing behavior and the elastomeric Yoshimura origami cylinders mainly grow in the height direction. As the origami structures are almost unfolded, the dominant morphing behavior shifts from unfolding to stretching and the entire body inflates. Consequently, the D-PneuNets actuators undergo deployment and bending where the origami chambers grow in the height direction, getting ready to generate high power, and the origami chambers inflate and bending the entire actuator. The bending is produced by strain difference between the inflating chambers and the strain-limiting layer, in addition to the mutual contacts that chambers pushing against each other. It is also notable that the unfolding proceeds rapidly from the beginning of actuation and is almost completes at a certain pressure, but bending occurs throughout the actuation process.

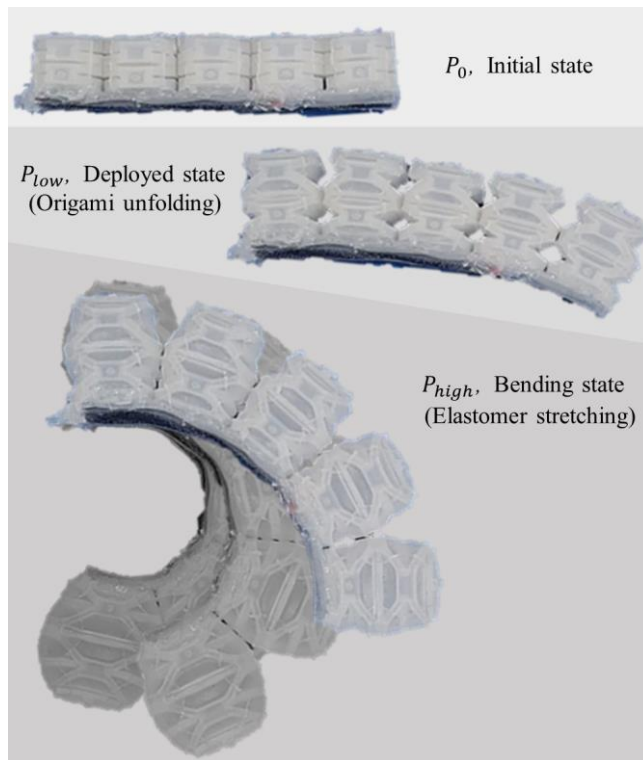


**Fig. 4.1.** A D-PneuNets actuator with five Yoshimura origami cylinder structured chambers and its deployment and bending behavior.

## 4.2 Characterization of the Actuator

### 4.2.1 Concept Validation

Based on the moment equilibrium and Hertzian contact theory, Zhu Liu et al established a tip force model of the soft pneumatic networks actuator []. Assuming that the thickness of the strain-limiting layer is small enough to be neglected, the tip force model is express as follow:

$$F_t = \frac{Pw(n-1)(7-4\alpha)}{2\{nl+(n-l)l_g\}}H^2 \quad (4.1)$$

Given the relationship  $F_t \sim H^2$ , the D-PneuNets actuators can generate an output force of  $(\frac{H_{unfold}}{H_{initial}})^2$  times compared to the conventional soft pneumatic networks actuators with chamber height of  $H_{initial}$ .

To validate the design concept, we measured the output forces of a D-PneuNets actuator and two soft pneumatic network actuators with each height equal to the initial height ( $H_{initial}$ ) and fully unfolded height ( $H_{unfold}$ ) of the D-PneuNets actuator (we call them Min-height PneuNets actuator and Max-height-PneuNets actuator respectively). The actuators are shown in Fig. 4.2. (a) (five chambers), and all of them were built with Dragon Skin 10. In order for the conditions to be as similar as possible, the corresponding design parameters between the D-PneuNets actuator ( $N_l=4$ ,  $h_{g1}=0.5$  mm,  $h_{g1}=0.5$  mm,  $t_w=1$  mm,  $t_w=1.5$  mm and  $l_c=5.25$  mm) and the conventional actuators were all designed to be the same (e.g., wall thickness). The initial and unfolded height

of the origami deployable chambers were  $H_{initial} = 13.5 \text{ mm}$  and  $H_{unfold} = 34.5 \text{ mm}$ , which is a 2.56 fold growth. The experimental setup is shown in Fig. 4(b); the tip of the actuator was positioned at the top of the load cell (333FDX, KTOYO), and the tip force at a zero bending angle was measured at an applied pneumatic pressure from 0 kPa to 12 kPa in 3 kPa increments, regulated by a pressure regulator (RVUM, PISCO). For each actuator, the experiment was performed 5 times.

The experimental result is shown in Fig. 4.2. (c). The output forces of the D-PneuNets actuator and the Max-height-PneuNets actuator were measured almost equally within the error range. At 12 kPa, the average output forces of the D-PneuNets actuator and Max-height-PneuNets actuator were 2.023 N and 2.109 N, respectively. On the other hands, the Min-height-PneuNets actuator only generated an average output force of 0.178 N at an applied pneumatic pressure of 12 kPa, which is significantly lower (<10 %) than the D-PneuNets actuator of the same initial chamber height. The experimental result, therefore, verifies the design concept of the D-PneuNets actuator, which is compact when not in use and capable of generating large force when required.

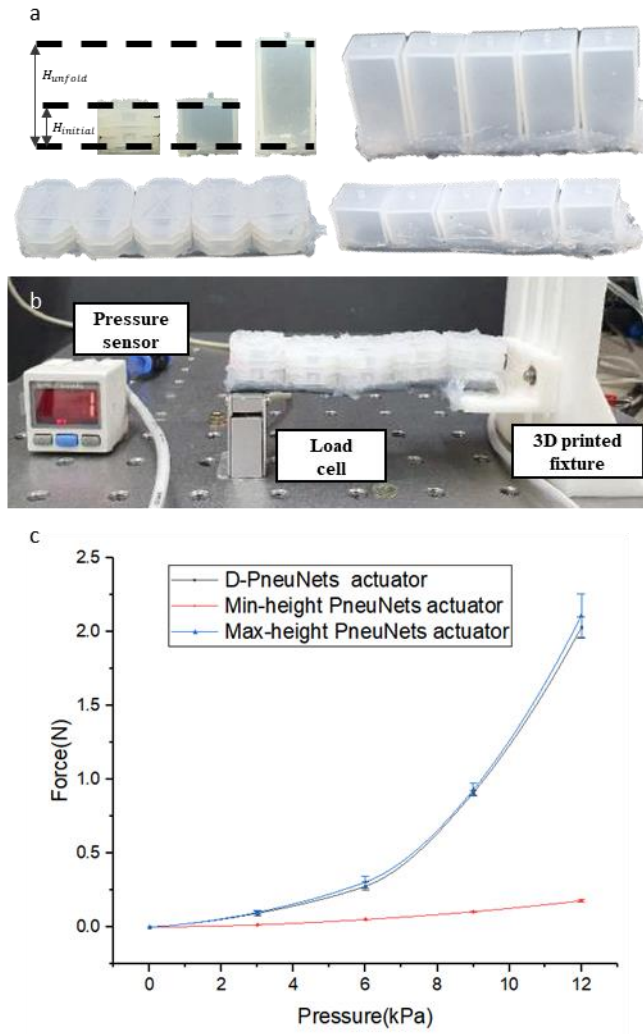


**Fig. 4.2.** A force measurement experiment. (a) D-PneuNets and two soft pneumatic network actuators with each height equal to  $H_{initial}$  and  $H_{fold}$ . (b) An experimental setup for force measurement. (c) An experimental result of the force measurement.

## 4.2.2 Characterization of the Behavior

Parametric studies regarding unfolding and stretching behaviors of elastomeric origami chambers were studied in Chapter 3; as the widths of the crease lines decrease, the unfolding response becomes more sensitive to applied pneumatic pressure while the stretching response of the material does not change. In this chapter, we have further investigated whether the unfolding behavior of the origami chambers affects the bending behavior of the actuator.

Two D-PneuNets actuators with three chambers, made of Dragon Skin™ 30, with  $l_g$  of 1mm and 3mm, respectively, were prepared. As experimental setup shown in Fig. 4.3. (a), the actuators were hung on a stand and red circle markers were attached. A pneumatic pressure was applied from 0 kPa to 30 kPa in 3 kPa increments, and frontal photographs were taken for every steps. Using the position data, the radius of the arc-shaped strain-limiting layer  $R$  and the change in chamber height  $\Delta H$  were calculated.

A finite element analysis (FEA) was conducted using a software ABAQUS as shown in Fig. 4.3. (b). In order to reduce computational complexity that increase run time and may cause non convergence problems, models divided into quarters with respect to a symmetrical plane were imported and boundary conditions corresponding to the symmetry conditions were set. Uniaxial and biaxial test results of the elastomers were imported to ABAQUS and fitted as

Ogden 3rd order hyperelastic model. All analysis were conducted under quasi-static condition and penalty contact method. FEA of conventional pneumatic networks actuators were also conducted in addition to FEA of the D-PneuNets actuators for comparison.

Experimental and simulation results for bending curvature of the actuators ( $\kappa = l/R$ ) and the height change of the chambers ( $\Delta H$ ) in response to applied pneumatic pressure are shown in Fig. 4.4. (a) and (b), respectively. For all actuators,  $\kappa$  increased slowly before the mutual contact ( $<3$  kPa) but increased rapidly after the interaction between chambers began ( $>3$  kPa). For example, for the D-PneuNets actuator with  $l_g = 3$  mm,  $\kappa$  was 0.00295 at 3 kPa and increased to 0.0118 at 9 kPa. Also, naturally,  $\kappa$  of the D-PneuNets actuator with  $l_g = 1$  mm was larger than for  $l_g = 3$  mm (from 39% to 77%) due to the effect of the mutual contact.

Particularly noteworthy, the gradient of  $\kappa$  for the D-PneuNets actuators is large during unfolding phase after the mutual contact ( $3 \text{ kPa} < P < 9 \text{ kPa}$ ), and then the gradient decreases as the chambers are mostly unfolded ( $P > 12 \text{ kPa}$ ). For the conventional pneumatic networks actuators, on the other hands, the gradient of  $\kappa$  gradually increases as pressure is applied. This seems to be because the crease lines of the D-PneuNets actuators protrude in side directions during the unfolding process, causing a large interaction between the chambers.

Consequently, the D-PneuNets actuators significantly bent more than the conventional pneumatic networks actuators. For example, for the simulation results of the D-PneuNets actuator and the pneumatic networks actuator with  $l_g = 1$  mm,  $\kappa$  at 22.5 kPa were 0.0411 and 0.0266, respectively.

For  $\Delta H$ , the D-PneuNets actuator with  $l_g = 3$  mm was slightly larger for  $l_g = 1$  mm. The result is probably because the interaction between the chambers inhibits the unfolding. In addition,  $\Delta H$  of the conventional pneumatic networks actuators increased as the chambers were stretched, but the amount was significantly lower than the D-PneuNets actuators deployed by unfolding at a low pressure; simulation results of  $l_g = 3$  mm actuators for  $\Delta H$  at 30 kPa were 21.54 mm and 4.88 mm, respectively.

The simulation results of the D-PneuNets actuator and the PneuNets actuator's internal volume in response to applied pressure are shown in Fig. 4.5. (a). Due to the overlap of the unfolding and stretching,  $V$  of the D-PneuNets actuator increases rapidly from  $1.73 \text{ cm}^3$  to  $54.29 \text{ cm}^3$ , compared to  $V$  of the PneuNets actuator with only stretching increases from  $20.76 \text{ cm}^3$  to  $49.17 \text{ cm}^3$ , for an applied pressure of 30 kPa. From the result, the stored energy ( $E$ ) to the applied pressure was calculated, and result shows that  $E$  of the D-PneuNets actuator was significantly higher (more than 1.7 times) than PneuNets actuator at the same applied pressure (Fig. 4.5. (b)). On the other

hands, there was no significant difference in required energy for bending, especially after fully unfolded, as shown in Fig. 4.5. (c).

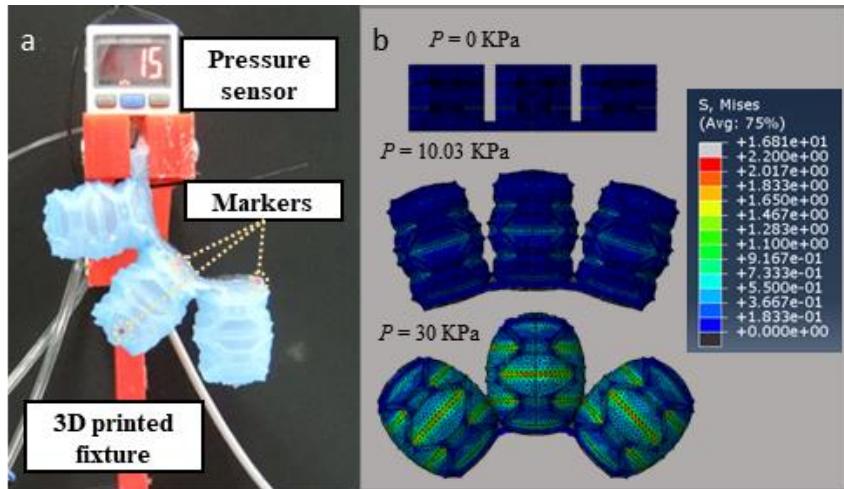
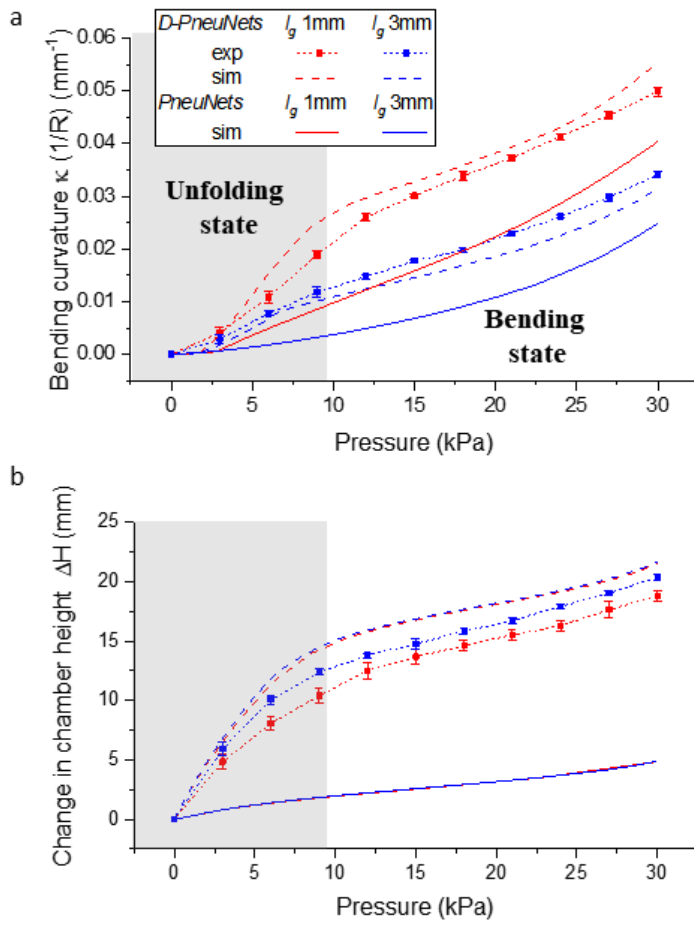
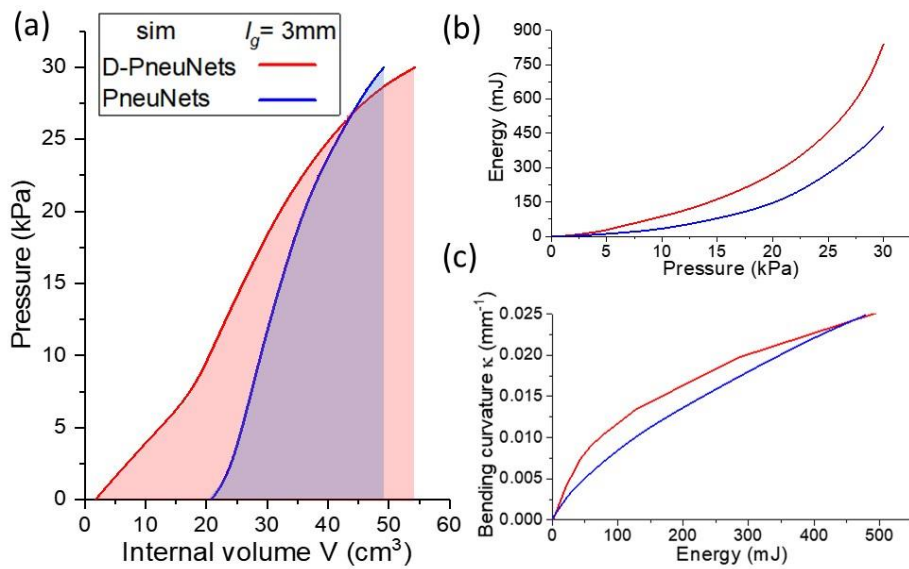


Fig. 4.3. The deployment and bending behavior of a D-PneuNets actuator. (a) An experimental setup to measure the deployment and bending behavior. (b) FEA simulation results of the D-PneuNets actuator with  $l_g = 3$  mm.



**Fig. 4.4.** Experimental and simulation result (a) of the curvature  $\kappa$  and (b) the change in chamber height  $\Delta H$  for the actuators with  $l_g = 1$  mm and 3 mm.



**Fig. 4.5. Simulation result of the D-PneuNets and PneuNets actuators for the internal volume and (b) the stored energy to applied pressure. (c) The relationship between the stored energy and the bending curvature.**

### 4.2.3 Dual-material Yoshimura Origami Cylinder Chamber

The chamber side walls of conventional pneumatic networks actuators are designed to be thicker than the front and back walls, or undesired bulge outs of the chamber occur in areas where mutual contact does not occur. However, for the D-PneuNets origami chambers,  $H_{initial}$  increases as the side wall thickness  $t_w$  increases, resulting in a decrease in  $\lambda$ . Instead of thickening the side walls, we applied a dual material design to increase the stiffness of the side walls. As shown in Fig. 4.6. (a), the chamber was divided into 4 sections in the shape of an X when viewed from above, and Dragon Skin™ 30 was applied to two sections corresponding to the side walls while Dragon Skin™ 10 was applied to the rest of the sections.

The shape changes of the single-material chamber and the dual-material chamber were measured. From 12 kPa to 24 kPa in 3 kPa increments, a pneumatic pressure was applied and the top view photographs were taken as shown in Fig. 4.6. (b); low pressure was excluded because the chambers did not expand sufficiently enough. The shape of the inflated chambers viewed from above was assumed as an ellipse. Using MATLAB code, the boundaries were found and eccentricities were calculated. FEA was also conducted and analyzed in the same process.

Experimental and simulation results of eccentricity in response to the applied

pressure is shown in Fig. 4.6. (c). As intended, the lateral bulge out of the dual-material chamber was mitigated compared to the single-material chamber. The eccentricities were 1.18 and 1.09 at 21 kPa for the dual-material chamber and single-material chamber respectively. Compared to the simulation result, the experimental result shows smaller difference in eccentricity between the single-material chamber and the dual-material chamber, which is presumably due to the unintentional mixing of materials between half-cured Dragon Skin™ 10 and injected Dragon Skin™ 30 during the fabrication process.

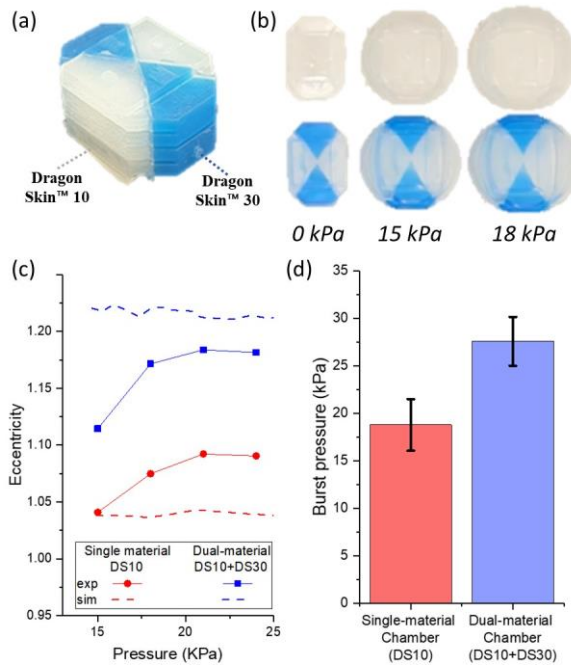


**Fig. 4.6. A Dual-material Yoshimura origami cylinder chamber. (a)** A material composition of the dual-material chamber. **(b)** Dual-material origami chambers viewed from above. **(c)** Experimental and simulation results for the eccentricity of the origami chambers. **(d)** Experimental results for the burst pressure of the origami chambers.

### 4.3 Robotic Soft Glove Using D-PneuNets Actuators

For the purpose of assisting and rehabilitating hand motor functions of stroke patients, researchers have been developed robotic gloves that bend fingers [39], [132]–[135]. In particular, robotic soft gloves using soft pneumatic actuators provide not only inherent safety but also simplicity to users that comes from no need of rigid components or complicated routing, compared to linkage-based mechanisms [136]–[138] and tendon-driven mechanisms [39], [135], respectively. These advantages offer the potential of greatly improving the activities of daily living (ADL).

A soft robotic glove prototype using D-PneuNets actuators was developed as shown in Fig. 4.7. Due to the deployable actuator, the developed soft robotic glove provides initial compactness while generate sufficient force when in use. Two D-PneuNets actuators wrap over the index and middle fingers (six and seven chambers, respectively) and fastened by elastomeric thimbles, finger straps, and a wrist strap. All elastomeric components were fabricated in a single step by molding and casting, using 3D printed molds. The dual-material chambers with  $N_l = 2$  ( $H_{initial} = 6.75$  mm) were chosen for compactness. Air was applied to both actuators simultaneously through urethane tubes using an external pneumatic source. The glove part is entirely soft, water-proof, and light-weight, weighing 71.2g.

An experiment to measure pressure distribution of the D-PneuNets soft robotic glove during wrap grasping was conducted. A mat-type pressure sensor Pliance® (Novel Inc.) was wrapped around two cylindrical objects with diameters of 65 mm and 140 mm. After sensor calibration, the wearer wrapped the objects with his hand relaxed, and then 15 kPa of pneumatic pressure was applied to the D-PneuNets soft robotic glove. The result is shown in Fig. 4.8 (a) and (b); the D-PneuNets soft robotic glove generated 3.10 N and 4.23 N for diameter of 65 mm and 140 mm cylinders, respectively. The measured pressure was distributed as low values due to the softness of the glove and human hand. Assuming the friction coefficient of Dragon Skin™ 30 as 0.8 [139], it can be concluded that the D-PneuNets soft robotic glove can hold up to weight of 345 g by applying only 15 kPa of pneumatic pressure.

Finally, we conducted a grasping test with the D-PneuNets soft robotic glove for six everyday-objects as shown in Fig. 4.9. Objects of various shapes (pouch, ball, cylinder, boxes, etc.) and weights (from 17 g to 175 g) were moved and placed by a subject wearing the D-PneuNets soft robotic glove with same applied pneumatic pressure of 20 kPa. It took about 60 seconds to move the six objects, and all objects were held stably without slip or wobble.

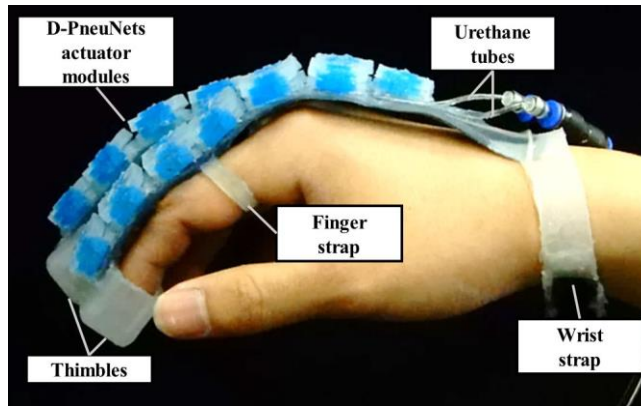


Fig. 4.7. A prototype of the D-PneuNets soft robotic glove.

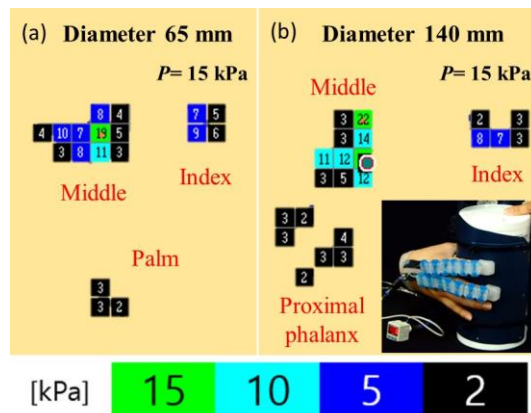
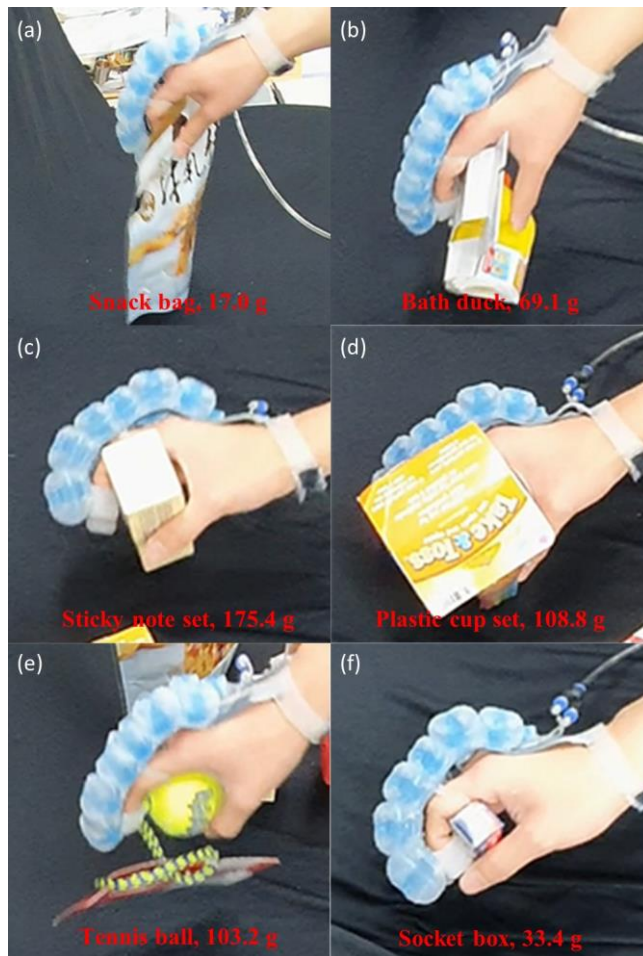


Fig. 4.8. Wrap grasping pressure measurement results for cylindrical objects of (a) diameter= 65mm and (b) diameter= 140mm.



**Fig. 4.9.** Grasping tests with various objects. (a) Snack bag, (b) bath duck, (c) Sticky note set, (d) plastic cup set, (e) tennis ball, and (f) socket box.

## 4.4 Fabrication of D-PneuNets Actuators

Molding and casting is the most general fabrication method for elastomeric soft robots. For complex structures such as origami structures, however, a detaching process of the mold may require too much effort. In addition, the mold may have to be sacrificed by breaking or melting [140]. In Chapter 3, a stacking of the water-soluble polyvinyl alcohol (PVA) molds was proposed to fabricate the elastomeric origami structures. Because the sacrificial molds are not reusable, the processes were time and cost consuming compared to the general molding and casting process.

To solve this issue, we designed inner molds to be easily assembled and disassembled through magnetic force. As shown in Fig. 4.10. (a), neodymium disc magnets were fitted inside the holes of the base molds and the inner molds. After the elastomers are cured, the inner molds can be disassembled and pulled out from inside the elastomeric origami chambers part by part, instead of sacrificing them. All molds were 3D printed by Objet 260 Connex3 (Stratasys Ltd.) using a rigid material VeroWhitePlus™ (shore hardness 85D, Stratasys, Ltd.).

The fabrication process of the D-PneuNets actuators is shown in Fig. 4.10. Similar to the fabrication process of the conventional soft pneumatic bending actuators, the extensible fluidic networks and the inextensible strain-limiting

layer are fabricated separately, and are bonded in the final process. The fabrication process of the pneumatic networks is shown in Fig. 4.10. (a) and (b). First, neodymium disc magnets were assembled to the base mold and the inner molds, and the inner molds were stacked on top of the base mold. Secondly, the outer molds (A, A' and B) were assembled in sequence. At this time, the outer molds A and A' were aligned along the triangularly shaped bulges of the base mold. Finally, an elastomer, Dragon Skin™ 10 (shore hardness A 10, Smooth-on Inc.) or Dragon Skin™ 30 (shore hardness A 30, Smooth-on Inc.), was injected through the holes of the outer molds, cured in an oven at 75°C for 1 hour, and the molds were disassembled in the reverse order. In the preparation process, elastomers were colored using silicone color pigments Silc Pig™ (Smooth-on Inc.) to be distinguished.

We also developed a fabrication process for dual-material chambers as shown in Fig. 4.10. (c) (the purpose of the dual-material chamber is discussed in Section III-C). After the process shown in Fig. 4.10. (a), the outer mold C with no gaps between the inner molds was assembled, and Dragon Skin™ 30 was injected through the outer molds A and A' and half-cured in the oven at 75°C for 15 minutes. The half-cured elastomer hardens and retains its shape, but still can adhere to uncured elastomers. Then, the outer mold C was replaced by outer mold B and Dragon Skin™ 10 was injected through the outer mold B.

After cured in the oven at 75°C for 6 hours, the molds were disassembled.

The inextensible strain-limiting layers were fabricated as shown in Fig. 3.10. (d) and were attached with the pneumatic networks as shown in Fig. 3.10. (e). An elastomeric adhesive (Sil-poxy™, Smooth-on Inc.) was applied flawlessly on the strain-limiting layer, the pneumatic network was placed on it. Finally, 1.8-mm-diameter polyurethane tube (MPUT1.8-10-C, MISUMI) was inserted at the end, and the actuator was cured in the oven at 75°C for 10 minutes.

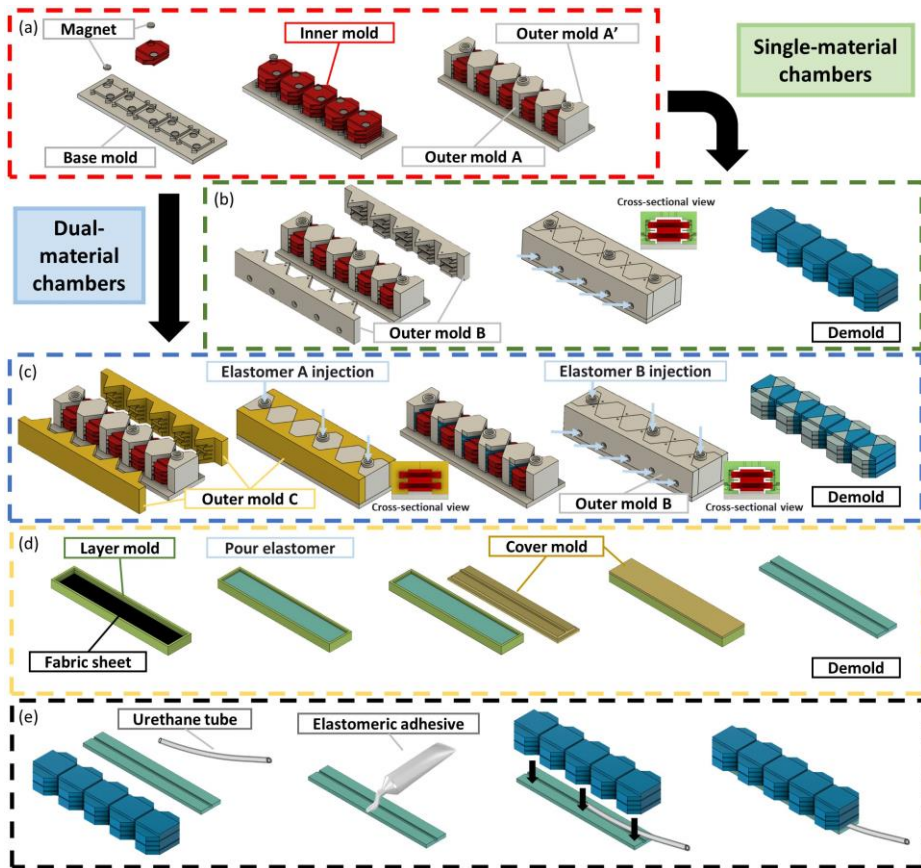


**Fig. 4.10.** A schematic diagram of the fabrication process. (a) Assembly process of mold using neodymium magnet. (b) Fabrication process of the single-material chambers, (c) the dual-material chambers, (d) the inextensible strain-limiting layer. (e) Attachment process of the chambers and the strain-limiting layer.

## 4.5 Discussion

In this chapter, a new type of soft pneumatic networks bending actuator utilizing deployable origami-shaped chambers was proposed, to generate high force compared to the compact initial form. Both behaviors of the actuator and the inflation of chambers, including dual-material chamber for preventing unnecessary bulge out, were characterized by experiment and FEA simulation. As an application, a prototype of the robotic soft glove using D-PneuNets actuators was developed. The experiment and demonstration confirmed that the developed robotic glove provides sufficient performance to grab various everyday-objects, with advantages of having an initial compact form and low actuation pressure. Despite the complex origami structure, the D-PneuNets actuators could be fabricated by molding and casting with the help of magnet assembly/disassembly of inner molds.

Future works for D-PneuNets actuator include analytic or numerical modelling to estimate both the morphing of chambers and the bending of the strain-limiting layer. For the D-PneuNets soft robotic glove, building the entire system including a controller and a power source (e.g., a pneumatic supply system presented in [141]) and evaluating the usability and durability are required. As for the fabrication method that enables mold reconfiguration and multi-material placement, we expect it to be utilized in the manufacturing of

multi-functional soft robots. We believe our approach offers a new design method for compact and space-efficient pneumatic soft actuators that can also be implemented in various materials (e.g., fabrics and TPUs), and can be applied to portable, mobile, or wearable robotic applications.

| Notation      | Definition  |
|---------------|---|
| $F_t$         | Tip force of the soft bending actuator  |
| $P$           | Applied pressure  |
| $n$           | Number of the soft bending actuator's chambers  |
| $w$           | Width of the soft bending actuator's chamber  |
| $l$           | Length of the soft bending actuator's chamber   |
| $l_g$         | Gap length between chambers   |
| $\alpha$      | Coefficient related to Hertzian contact   |
| $H$           | Height of the chamber   |
| $N_F$         | Number of facets of Yoshimura origami cylinder that lie in the same plane when fully folded |
| $N_l$         | Number of layers of the Yoshimura origami cylinder  |
| $\phi$        | Subtended angle of the Yoshimura origami trapezoid  |
| $H_{initial}$ | Fully folded height of the Yoshimura origami cylinder                                       |
| $H_{unfold}$  | Fully unfolded height of the Yoshimura origami cylinder                                     |
| $h_{g1}$      | Outside gap length between facets   |
| $h_{g2}$      | Inside gap length between facets  |
| $t_w$         | Wall thickness of the Yoshimura origami cylinder  |
| $t_c$         | Ceiling thickness of the Yoshimura origami cylinder   |
| $l_c$         | Height of a single Yoshimura origami tessellation   |
| $\kappa$      | Bending curvature of the soft bending actuator  |

**Table 4.1. Notations used in chapter 4.**

## **Chapter 5. A Dual-origami Design for Soft Robots**

Soft fluidic actuators produce continuous and life-like motions that are intrinsically safe, but current designs are not yet mature enough to enable large deployment with high force and low-cost fabrication methods. In this section, we present a soft robot with a small initial form factor that undergoes quasi-sequential deployment and bending motion driven by a single fluid input, enabled by a dual-origami design in which both the fluidic network and the strain-limiting layer are compliant origami architectures. We selectively placed the folded strain-limiting layer in between the facets of the folded fluidic network, building the latter to be more extensible than the former. Accordingly, in an early stage of the response to fluid pressure, the two elements both unfold simultaneously, and the whole body mainly deploys while slight bending also occurs simultaneously, depending on the stiffness of the origami strain-limiting layer. And when the strain-limiting layer is almost fully unfolded, the fluidic network unfolds solely to drive the whole body to bend, accessing the regime outside of origami kinematics by utilizing flexibility of the soft material. The motion is pre-programmable through adjusting design parameters of the origami strain-limiting layer. The finite element analysis (FEA) and experimental results provide relationships between the quasi-sequential deployment and bending motion and the geometries, to select an appropriate

parameter value for a given desired motion. Dual-origami soft actuators can be directly printed by a low-cost fused deposition modeling (FDM) 3D printer using flexible filaments such as thermoplastic polyurethane (TPUs) or thermoplastic elastomers (TPEs), with an introduction of a heat treatment post-processing for soft fluidic robots to leverage high pressure holds ( $>200$  kPa). Our new design method for soft robots achieved an effective spatial extension from a limited form factor, and embodies not only portability but also cooperative abilities with other mechanical elements through growth and retract.

## **5.1 Motivation: Drawbacks of the Dual-morphing Principle**

A dual-morphing stretchable origami (Chapter 3, 4) presented an entirely stretchable origami that deploys by unfolding and then produce additional motion by anisotropic stretching. Although this dual-morphing principle that utilizes both morphing principles of unfolding and stretching could achieve extreme shape morphing, there exist several limitations originating from the essential use of highly stretchable materials: i) low force due to incapability of holding high pressure, ii) poor reliability due to non-linearity of materials and Mullins effect, iii) slow response time due to heavy reliance on material response speed iv) difficulty in control due to difficulties in kinematics analysis of stretching behavior, and v) narrow material selection with only a few specific

materials (expensive silicone elastomers or high-tech 3d printing materials) available. In addition, a complex fabrication process using sacrificial molds, as well as the need for deposition of multiple materials to achieve functional motion (e.g. bending) over deployment and balloon-like bloating, significantly increase fabrication cost. These drawbacks presented challenges for practical usage of dual-morphing principle in real-world applications, highlighting a need for a new design method of a different working principle that does not rely on stretching, broadens the range of applicable materials, and enables large deployment, high force, and low-cost/easy fabrication (the detailed comparison of the dual-morphing principle and the current work is shown in Table 5.1.).

|                               | <b>Dual-origami design</b>                                     | <b>Dual-morphing origami design</b>   |
|-------------------------------|--|---|
| <b>Deformation</b>            | Extremely large  | Large   |
| <b>Morphing modes</b>         | 1 (unfolding)  | 2 (unfolding and stretching)  |
| <b>Working principle</b>      | Asymmetric unfolding of two origami structures                 | Origami unfolding and material stretching   |
| <b>Motion</b>                 | Quasi-sequential deployment and bending                        | Quasi-sequential deployment and inflating   |
| <b>Material property</b>      | Flexible but non-stretchable                                   | Highly stretchable only   |
| <b>Material stiffness</b>     | $E > 10 \text{ MPa}$   | $E < 0.5 \text{ MPa}$   |
| <b>Number of materials</b>    | 1  | 1 (only balloon-like bloating available) or more (for pre-programming)                  |
| <b>Pre-programming method</b> | Tuning the relative length and stiffness of origami structures | Selective disposition of multiple materials   |
| <b>Applied pressure level</b> | High ( $> 100 \text{ kPa}$ )                                   | Low ( $< 30 \text{ kPa}$ )  |
| <b>Output force</b>           | $> 3 \text{ kgf}$  | $< 300 \text{ gf}$  |
| <b>Reliability</b>            | Good   | Poor (due to materials' non-linearity and Mullins effect)                               |
| <b>Response time</b>          | Fast   | Slow  |
| <b>Kinematically defined</b>  | Yes  | No  |
| <b>Fabrication</b>            | Low-cost 3D printing (FDM)                                     | Layer mold stacking requiring sacrificial molds or high-tech multi-material 3D printing |

**Table 5.1. Comparison of the dual-origami design and dual-morphing origami design.**

## 5.2 Design and Working Principle

### 5.2.1 Dual-origami Components

A common six-module dual-origami soft fluidic bending actuator that is initially folded and deploys through dual-origami unfolding is shown in Fig 5.1.

(a). Two integral components of the dual-origami design are the origami fluidic network and the origami strain-limiting layer based on conventional deployable origami architectures. We selected Miura-ori polyhedron and zigzag folded Miura-ori as the parent origami frame of two components, respectively [142]. For soft robotic application, we modified/determined their geometry as follows: (1) For both origami architectures, we merged two parallelograms on the same layer by removing the shared crease line because the folding of the removed crease line can be replaced by the bending of the merged flexible facet. (2) The Miura-ori polyhedron's diamond shaped crease-line-loops at the top and bottom were enclosed by plates of the same shape for fluidic actuation. (3) We optionally made a V-cut at the crease lines of the zigzag folded Miura-ori to tune the folding stiffness. As shown in Fig 5.1. (a) and (b), the proposed dual-origami design is in the initial folded form where the zigzag folded Miura-ori strain-limiting layers are interposed between the facets of the Miura-ori polyhedron fluidic network.

Both origami components are built to be C-channel-shaped geometry in which their facets are serially connected in the direction of stacking via C-

channel shaped crease lines. When bending moments are applied at the C-channel shaped crease lines, bending intensively occurs as if origami unfolding occurs. Because the applied fluidic pressure at the Miura-ori polyhedron fluidic network produces bending moments at entire crease lines directly (fluidic network) or indirectly (strain-limiting layer), dual-origami components unfold simultaneously. We defined a single module dual-origami unit as the structure consisting of a flat fluidic network with two parallel facets and a strain-limiting layer of a single facet connected to it. A multi-module dual-origami can be readily designed by the stacking module units and connecting them via C-channel-shaped crease lines.

### **5.2.2 Quasi-sequential Deployment and Bending Motion**

The quasi-sequential deployment and bending behavior of a representative six-module dual-origami soft fluidic bending actuator was experimentally measured and plotted in Fig. 5.2. This peculiar motion can be distinguished into two modes that quasi-sequentially appear in accordance with the applied fluid pressure level Fig 5.1. (c). The first mode, a deployment-dominant mode, appears at relatively low fluid pressure ( $P < 40$  kPa), and both the origami fluidic network and the origami strain-limiting layer unfold simultaneously. Therefore, the deployment ratio ( $\lambda = \frac{L-L_0}{L_0}$ , where  $L$  is the effective layer length and  $L_0$

is its initial value), in response to applied fluidic pressure, rapidly increases compared to the bending angle ( $\phi$ ) (Fig 5.3., red area and Fig. 5.4.). As the applied fluid pressure increases, the second mode, a bending-dominant mode appears, and the unfolding speed of origami fluidic network overwhelms the unfolding speed of the origami strain-limiting layer. This is because the strain-limiting layer is nearly completely unfolded yet the fluidic network is not, and thus  $\phi$  surges while  $\lambda$  slowly increases (Fig 5.3., gray area and Fig. 5.4.). When the applied pressure is decreased, the deployed soft body retracts due to its own elasticity. We also built a conventional soft bending actuator (widely known as PneuNet design) [61], [62], [64], and plotted its behavior for comparison (Fig 5.1. (b), black line). Although the initial length  $L_0$  of the dual-origami design (29.5 mm) was much lower than the  $L_0$  of the conventional design (107 mm), the dual-origami actuator was unfolded similarly in scale to the conventional actuator, and the bending trajectories overlapped near  $16^\circ < \phi < 80^\circ$  (the conventional design is still advantageous for large bending because of the trade-off relationship between deployment and bending, which is further discussed in section 2.2). The aspect ratio of the dual-origami bending actuators was initially 0.657 and increased up to 3 when unfolded, which is similar to the conventional soft bending actuator's aspect ratio of 2.89 (dimensions of both actuators are shown in Fig. 5.5.).

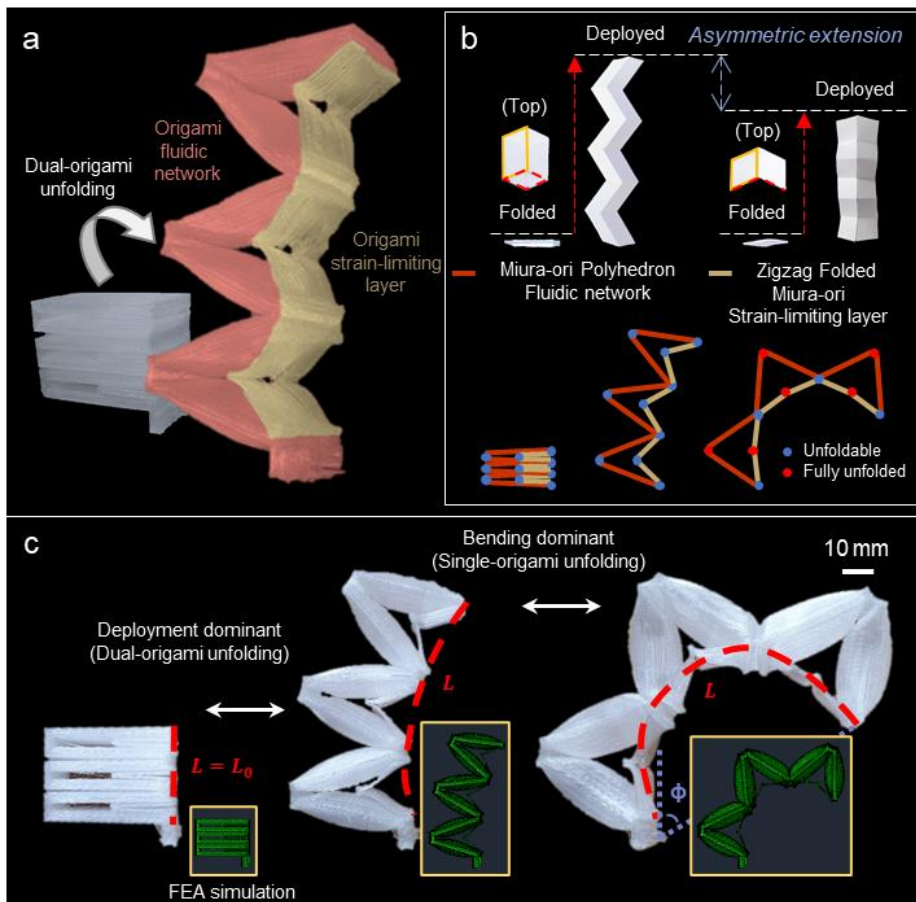


**Fig. 5.1. Design and principle of the dual-origami soft fluidic bending actuator. (a) Unfolding of six-module dual-origami soft fluidic bending actuator. (b) Parent paper origami structures and their schematic drawings of behavior in a dual-origami soft fluidic bending actuator. (c) Quasi-sequential deployment and bending motion of six-module dual-origami soft fluidic bending actuator. Insets represent corresponding simulation result.**

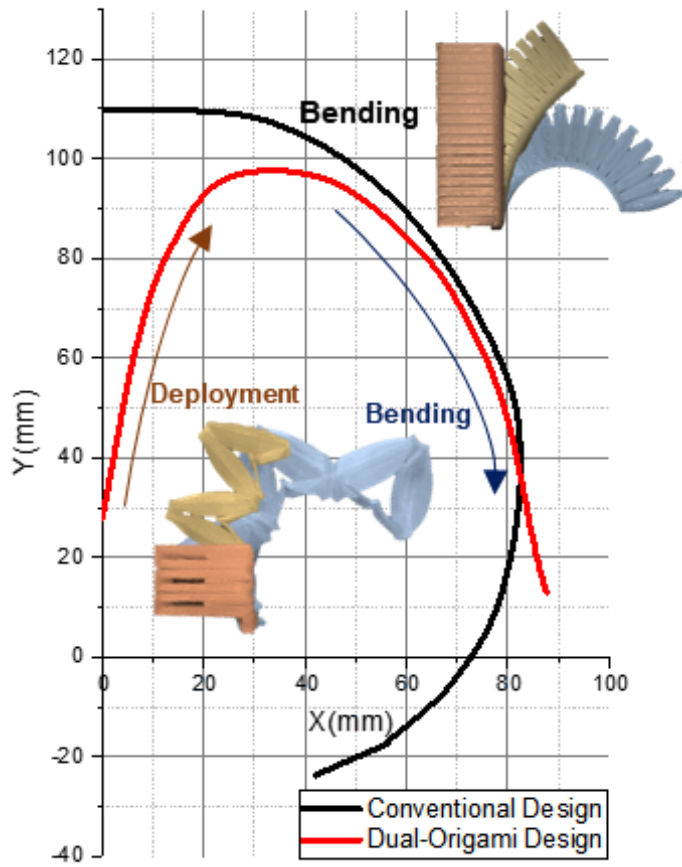


**Fig. 5.2. End-tip trajectories of dual-origami soft bending actuator and conventional soft pneumatic bending actuator.**

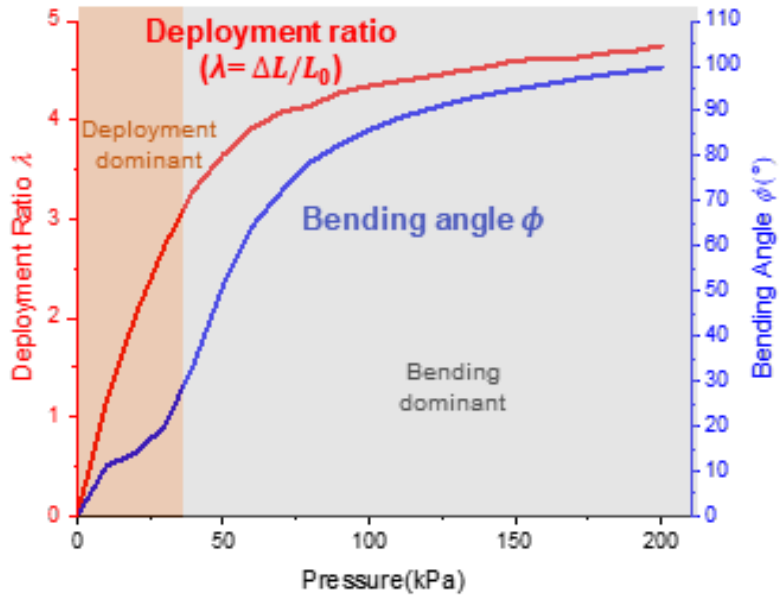


**Fig. 5.3. Deployment ratio ( $\lambda$ ) and bending angle ( $\phi$ ) in response to applied pressure.**

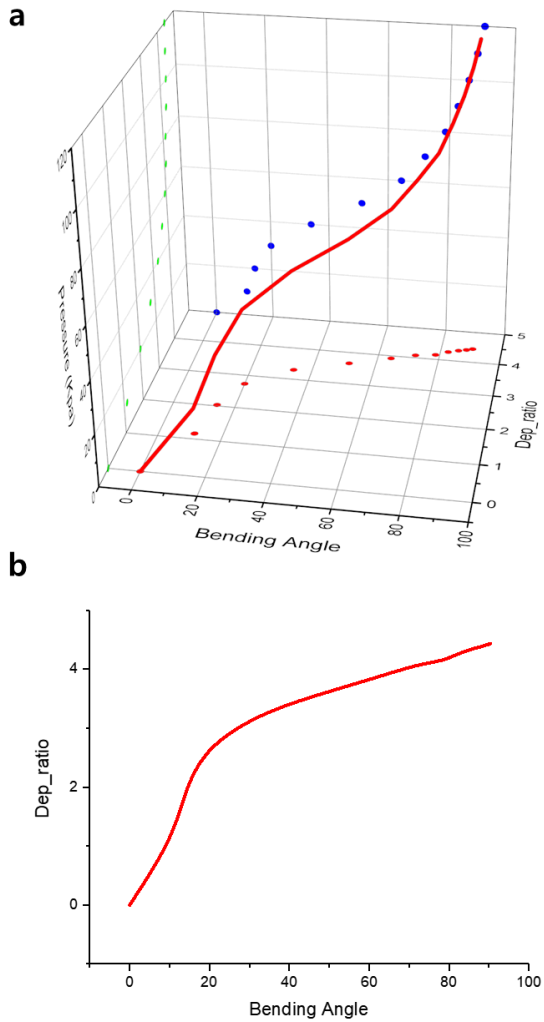


**Fig. 5.4. The quasi-sequential motion of the Dual-origami actuator.**

**(a) A 3D plot of pressure, bending angle and deployment ratio. (b)**

**Change in bending angle and deployment ratio during actuation.**

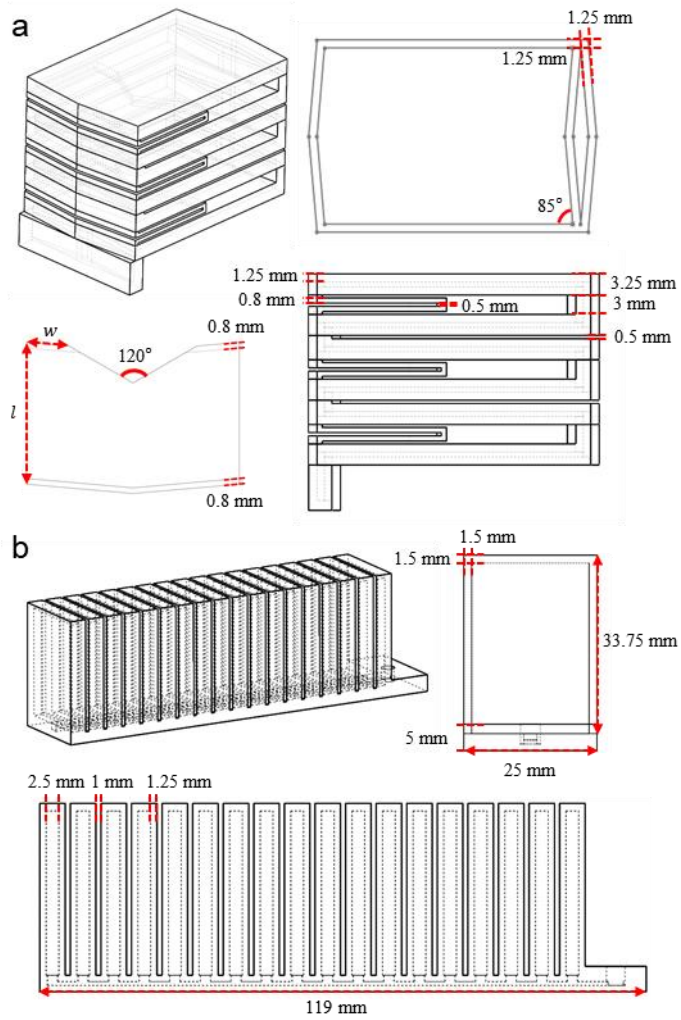


**Fig 5.5. Dimensions of (a) dual-origami soft fluidic bending actuator ( $w= 6$  mm and  $l= 20$  mm) and (b) conventional soft bending actuator.**

## 5.3 Pre-programming of the Motion

### 5.3.1 Simplified Kinematic Model

The six-module dual-origami soft fluidic robot can be represented as connected linkage model, and its lengths, angles, and positions were defined as shown in Fig 5.6. With the assumption that the stretching of the material is negligible ( $E \sim 10$  MPa, strain is  $\sim 1\%$  at applied pressure of 100 kPa), it can also be assumed that lengths ( $L, h_1, h_2$ ) are constant.

For positions  $\vec{p}_n$ , following relationships can be established:

$$\vec{p}_0 = \begin{bmatrix} 0 \\ 0 \end{bmatrix} \quad (5.1)$$

$$\vec{p}_{4n-3} = \vec{p}_{4n-2} + \begin{bmatrix} h_1 \cos \beta_{2n-1} \\ h_1 \sin \beta_{2n-1} \end{bmatrix} \quad (5.2)$$

$$\vec{p}_{4n-2} = \vec{p}_{4n-3} + \begin{bmatrix} L \cos \alpha_{2n-1} \\ L \sin \alpha_{2n-1} \end{bmatrix} \quad (5.3)$$

$$\vec{p}_{4n-1} = \vec{p}_{4n-2} + \begin{bmatrix} h_2 \cos \beta_{2n} \\ h_2 \sin \beta_{2n} \end{bmatrix} \quad (5.4)$$

$$\vec{p}_{4n} = \vec{p}_{4n-1} + \begin{bmatrix} L \cos \alpha_{2n} \\ L \sin \alpha_{2n} \end{bmatrix} \quad (5.5)$$

For angles  $\alpha_n$  and  $\beta_n$  following relationships can be established:

For n is odd,

$$\alpha_{n+1} - \alpha_n = \begin{cases} 2\theta_n + \pi, & \text{for } \alpha_n < 0 \text{ and } \alpha_{n+1} > 0 \\ 2\theta_n - \pi, & \text{else} \end{cases} \quad (5.6)$$

$$\beta_{n+1} = \begin{cases} -\frac{\pi}{2} + \theta_n + \alpha_n + 2\pi, & \alpha_n < 0 \text{ and } \beta_{n+1} > 0 \\ -\frac{\pi}{2} + \theta_n + \alpha_n, & \text{else} \end{cases} \quad (5.7)$$

For n is even,

$$\alpha_{n+1} - \alpha_n = \begin{cases} -2\theta_n - \pi, & \text{for } \alpha_n > 0 \text{ and } \alpha_{n+1} < 0 \\ -2\theta_n + \pi, & \text{else} \end{cases} \quad (5.8)$$

$$\beta_{n+1} = \begin{cases} \frac{\pi}{2} - \theta_n - \alpha_n - 2\pi, & \text{for } \alpha_n > 0 \text{ and } \beta_{n+1} < 0 \\ \frac{\pi}{2} - \theta_n - \alpha_n, & \text{else} \end{cases} \quad (5.9)$$

Initial conditions  $\alpha_1$  and  $\beta_1$ :

$$\alpha_1 = \pi - \theta_0 \quad (5.10)$$

$$\beta_1 = \frac{\pi}{2} \quad (5.11)$$

By solving for (5.6-5.11), angles  $\alpha_n$  and  $\beta_n$  can be expressed as follows:

For  $n \geq 2$ ,  $n \in N$ ,  $m_1, m_2 \in Z$ ,

$$\alpha_n = 2 \sum_{k=1}^{n-1} \{(-1)^{k+1} \cdot \theta_k\} + \frac{1 + (-1)^n}{2} \pi + \pi - \theta_0 + 2\pi m_1 \quad (5.12)$$

$$\beta_n = -\frac{\pi}{2} + (-1)^n \left[ 2 \sum_{k=1}^{n-2} \{(-1)^{k+1} \cdot \theta_k\} + \theta_{n-1} + \pi - \theta_0 \right] + 2\pi m_2 \quad (5.13)$$

When all modules are same, following relationship for  $\theta_n$  is established:

$$\theta_n = \begin{cases} \theta_{ori}, & n \text{ is odd} \\ \theta_{free}, & n \text{ is even} \end{cases} \quad (5.14)$$

Finally, positions can be obtained as a function of  $\theta_n$  by substituting (5.1-5.5) and (5.10-5.14).

For 2N-module structure, bending angle  $\phi$  can be calculated from end-tip position  $\vec{p}_{4N}$ :

$$\vec{p}_{4N} = \begin{bmatrix} \sum_{k=1}^N \{L(\cos\alpha_{2k-1} + \cos\alpha_{2k}) + h_1\cos\beta_{2k-1} + h_2\cos\beta_{2k}\} \\ \sum_{k=1}^N \{L(\sin\alpha_{2k-1} + \sin\alpha_{2k}) + h_1\sin\beta_{2k-1} + h_2\sin\beta_{2k}\} \end{bmatrix} \quad (5.15)$$

In case of all modules are same and  $L \gg h_1, h_2$ ,  $\phi$  can be calculated from (5.15) as below:

$$\phi \approx \tan^{-1} \left\{ \frac{\sum_{k=1}^N \cos\alpha_{2k-1} + \cos\alpha_{2k}}{\sum_{k=1}^N \sin\alpha_{2k-1} + \sin\alpha_{2k}} \right\} \quad (5.16)$$

$$\phi \approx \tan^{-1} \left\{ \frac{\sum_{k=1}^N \sin\{(2k-1)(\theta_{free} - \theta_{ori})\}}{\sum_{k=1}^N \cos\{(2k-1)(\theta_{free} - \theta_{ori})\}} \right\} \quad (5.17)$$

$$\phi \approx N(\theta_{free} - \theta_{ori}) \quad (5.18)$$

In Fig 5.6. (c), the model was compared with the experimental result, and it was well suited for low applied pressure.

Change in effective layer length  $\Delta L$  can be approximated as a length of an arc:

$$\Delta L \approx 2N\theta_{ori}l_{network} \quad (5.19)$$

A ratio of the bending angle to the deployment ratio can be derived from (5.18) and (5.19):

$$\frac{\phi}{\lambda} = \frac{\phi}{\Delta L/L_0} \quad (5.20)$$

$$\frac{\phi}{\lambda} = \frac{L_0}{2l_{network}} \left( \frac{\theta_{free}}{\theta_{ori}} - 1 \right) = CA_0 \quad (5.21)$$

Where we defined bending-to deployment ratio factor  $C$  as

$$C = \frac{1}{2} \left( \frac{\theta_{free}}{\theta_{ori}} - 1 \right) \quad (5.22)$$

and  $A_0 = \frac{L_0}{l_{network}}$  is an initial aspect ratio.

We named  $C$  as the bending-to-deployment ratio factor because it represents the dominance of bending to deployment during the quasi-sequential deployment and bending motion. A high value of  $C$  means that the dominance of bending is large; when the robot only bends without deployment,  $C \rightarrow \infty$  (e.g., when the inextensible strain-limiting layer is attached, like conventional soft bending robots), and when the robot only deploys without bending,  $C = 0$  (e.g., origami fluidic network without a strain-limiting layer). For common dual-origami soft fluidic bending actuators, it was observed that  $C$  rapidly increase at the transition pressure at which the dominance shift occurs.

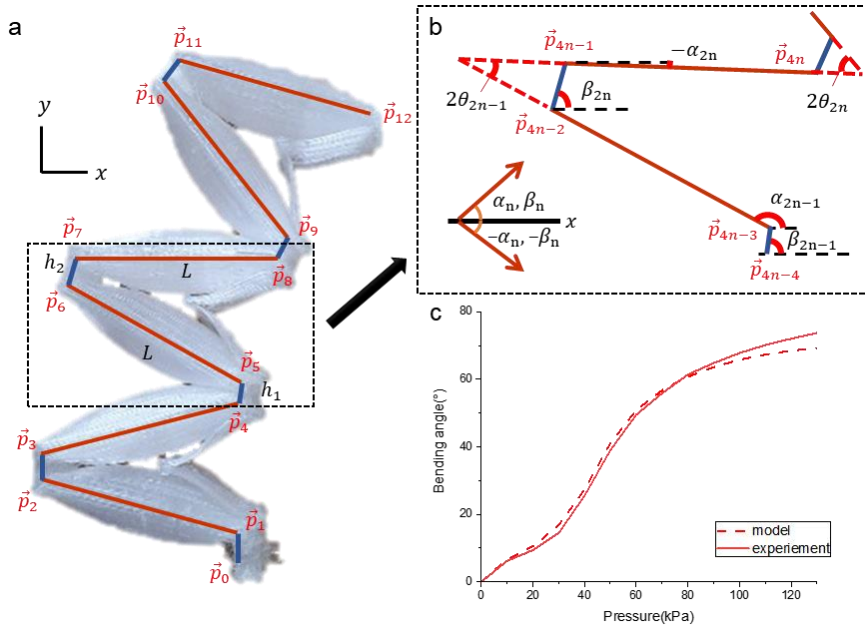


**Fig. 5.6. Linkage model for dual-origami soft fluidic actuator. (a) 6-module dual-origami soft fluidic actuator's linkage model and position vectors. (b) Definition of angles for calculating position. (c) Comparison of model for bending angle and experimental result.**

### 5.3.2 Pre-programming Method

In order to better understand the quasi-sequential deployment and bending motion, we investigated the relationship between the geometric parameters of the origami strain-limiting layer and  $\theta_{ori}$  or  $\theta_{free}$  by performing experiments and FEA simulations (Fig 5.7.). A crease line width of one side ( $w$ ) and a ratio between  $l_{layer}$  and  $l_{network}$  ( $\Lambda = l_{layer}/l_{network}$ ) were considered as the important geometric parameters because it was expected that the rotational stiffness of the crease line would increase with increasing  $w$  and the maximum value of  $\theta_{ori}$  would be geometrically determined by  $\Lambda$ . In both the experiment and simulation, the response of  $\theta_{free}$  to applied fluid pressure was constant even though geometric parameters of the origami layer at the nearby modules were changed (Fig. 5.7. (c)). On the other hand, the response of  $\theta_{ori}$  to applied fluid pressure was affected by  $w$  and  $\Lambda$ . It was noteworthy that the change in  $w$  gradually shifts the response while  $\Lambda$  changes it significantly (Fig 5.7. (d) and (e)). For example, the increase in  $w$  from 3 to 12 mm decreased  $\theta_{ori}$  from 58.16° to 49.56° at 100 kPa (for  $\Lambda=0.476$ ), and the increase in  $\Lambda$  from 0.238 to 0.476 increased  $\theta_{ori}$  from 25.47° to 54.43° at 100 kPa (for  $w=6$  mm). The result also indicates that the amount of deployment and bending should be selectively pre-programmed with consideration of their tradeoff relationship;  $\phi$  decreases as  $\theta_{ori}$  increases but

$\lambda$  is proportional to  $\theta_{ori}$ . Accordingly,  $C$  was 0.158 at 20 kPa for the most deployable case, while  $C$  was 0.825 at 20 kPa for the most bendable case, which is about 5.22 times difference (Fig 5.7. (b)).

To confirm the pre-programmability of the quasi-sequential deployment and bending motion, six-module dual-origami soft fluidic bending actuators with different geometric parameters were built. As shown in Fig 5.8., we could design clear differences in motion determined by  $w$  and  $\Lambda$ ; their end-tip trajectories were plotted in Fig. 5.8.  $\lambda$  decreased from 4.78 to 4.32 and  $\phi$  increased from 90.9° to 106.9° as  $w$  increased from 3 mm to 12 mm, whereas increase of  $\Lambda$  from 0.238 to 0.476 greatly increased  $\lambda$  from 2.35 to 4.75 and decreased  $\phi$  from 144.75° to 99.66° (at  $P=200$  kPa). The result confirms that the quasi-sequential deployment and bending motion is more sensitive to  $\Lambda$  than  $w$ . Therefore, it would be recommended to determine  $\Lambda$  for coarse adjusting in precedence to  $w$  for fine adjusting. Additionally, thickness of the strain-limiting layer ( $t$ ) can be considered for pre-programming of the motion. However, it should be noted that a small change in  $t$  would change motion dramatically because the bending stiffness of the layer is proportional to  $t^3$ , and therefore it is not recommended to tune  $t$  for motion pre-programming. (Fig. 5.9. shows simulation result that small change of  $t=0.6$  mm to 0.8 mm increases  $C$  significantly from 0.115 to 0.296 at 18 kPa).

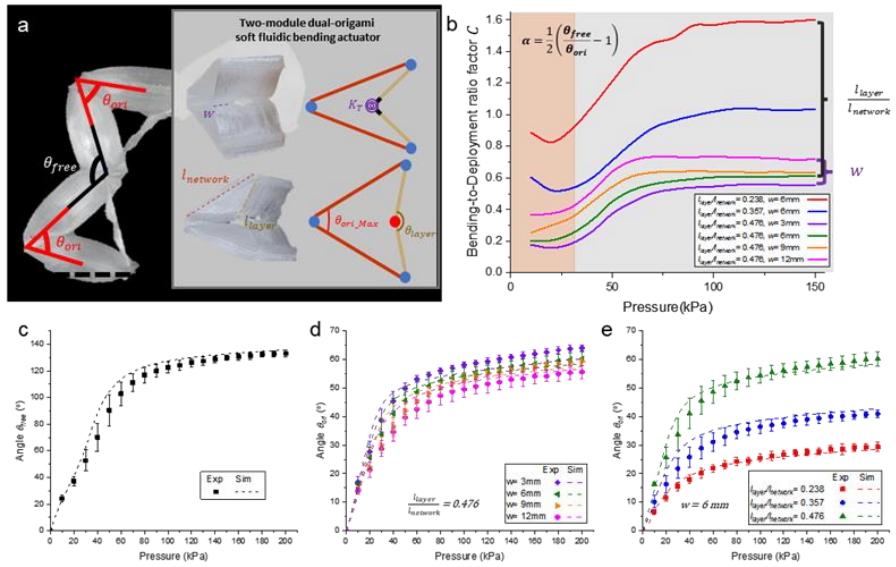


**Fig 5.7. Linkage model for dual-origami soft fluidic actuator. (a) 6-module dual-origami soft fluidic actuator's linkage model and position vectors. (b) Definition of angles for calculating position. (c) Comparison of model for bending angle and experimental result.**

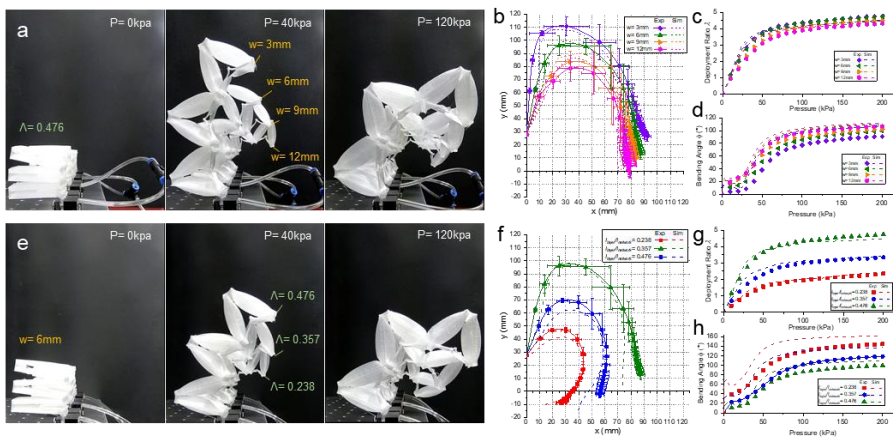


**Fig 5.8.** Pre-programming of 6-module dual-origami soft fluidic actuators. (a) For strain-limiting layer with different width ( $w$ ), six-module dual-origami soft fluidic bending actuators were placed in raw a and actuated simultaneously by same applied pressure. Experimental and simulation results for (b) end-tip trajectories, (c) deployment ratio ( $\lambda$ ), and (d) bending angle ( $\phi$ ) were plotted. (e, f, g, and h) Same procedure as (f-i) were performed for strain-limiting layer with different length ratio ( $\Lambda$ ).

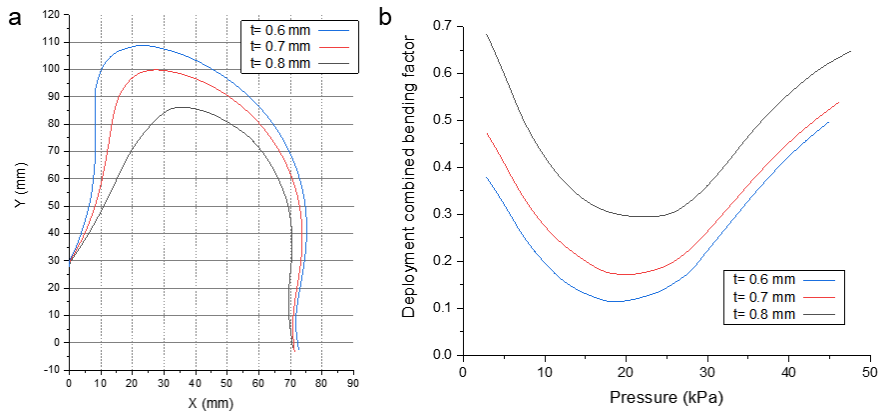


**Fig 5.9.** A parametric study of the relationship between the quasi-sequential deployment and bending motion and the thickness of the strain-limiting layer ( $t$ ). Data are achieved using FEA simulation. (a) End-tip trajectories of the 6-module dual-origami fluidic soft actuators with variable  $t$ . (b) Bending-to-deployment ratio factor in response to applied pressure (< 50 kPa, deployment state) with variable  $t$ .

## 5.4 Force Estimation: Simplified Pseudo rigid Body Model

The pseudo rigid body model of the six-module dual-origami soft fluidic robot is shown in Fig. 5.10.

Free body diagram shown in Fig.5.11. can be solved as follow:

$$k_n \theta_n - k_{n+1} \theta_{n+1} - FL_n \cos \left( \sum_{i=1}^{n+1} \theta_i - \varphi_i \right) = 0 \quad (5.23)$$

$$(n = 1, 2, \dots, N, k_{N+1} = 0)$$

$$k_n \theta_n = F \sum_{i=1}^{N+1-n} \{ L_{N+1-i} \cos \left( \sum_{j=1}^{N+1-i} \theta_j - \varphi_j \right) \} \quad (5.24)$$

The torsional stiffness of joints  $k_n$  is expected to be non-linear, determined by various factors including initial designed geometry, deformed geometry (Brazier effect [143], [144]), applied pressure [145], [146], and interaction between modules. To investigate  $k_n$ , FEA simulations that push the six-module dual-origami soft fluidic robot in lateral direction were conducted and  $k_n$  data in response to various applied pressure  $P$  and rotated angles of joints  $\theta_n$  were collected. For example,  $k_n$  at applied pressure  $P=50\text{kPa}$  is shown in Fig. 5.12.

(a). To investigate the effect of the interaction, the difference between non-contact and contact result was calculated as shown in Fig. 5.13. (b). The result shows that the interaction happens at a specific  $\theta_n$  and then  $k_n$  is linearly proportional to the change in  $\theta_n$ .

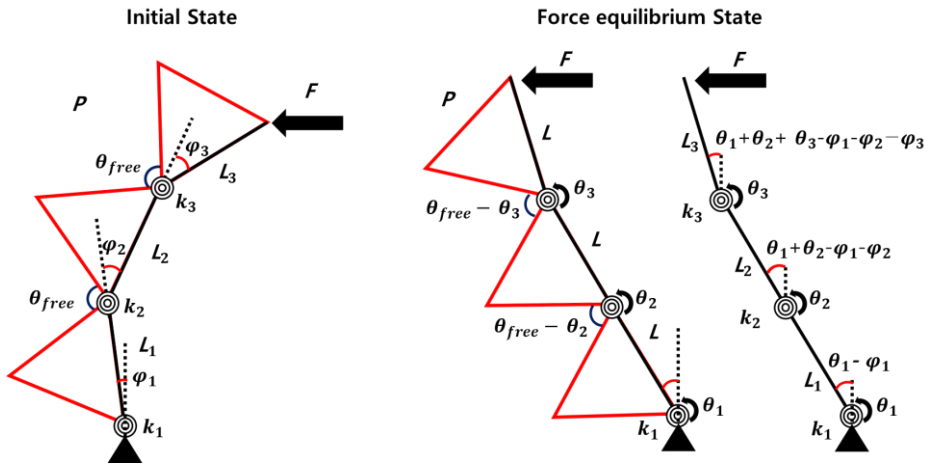


Fig. 5.10. Pseudo rigid body model for dual-origami soft fluidic actuator.

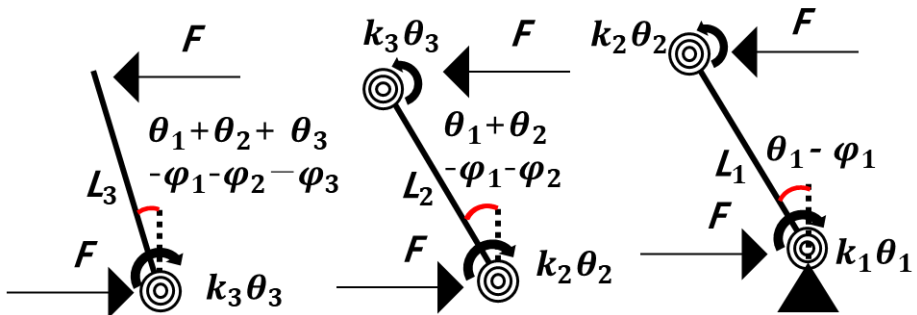
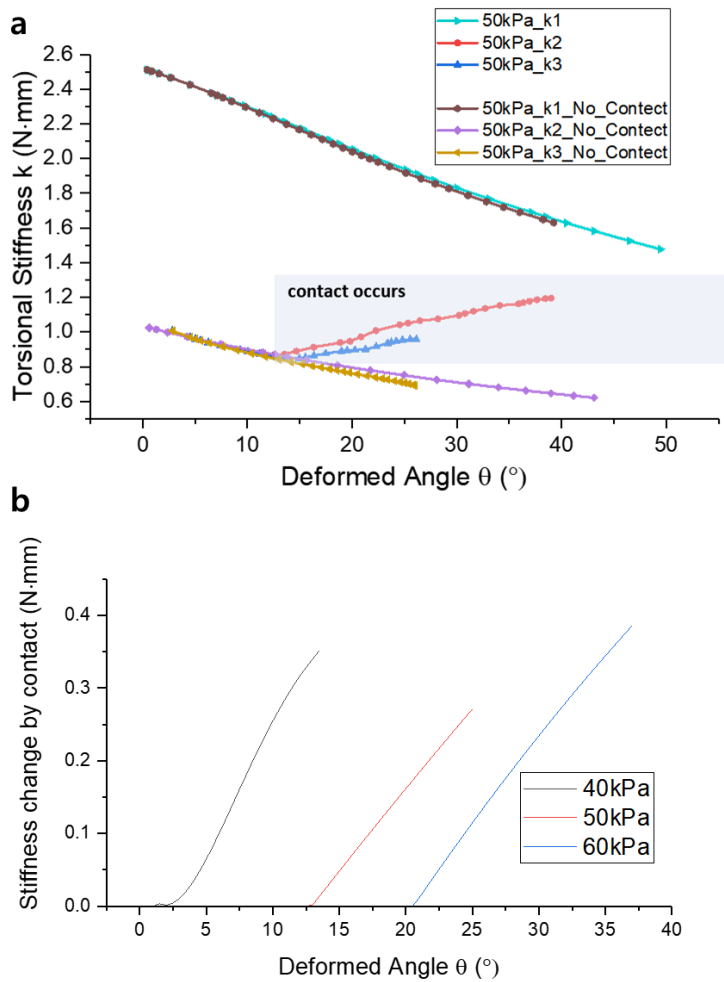


Fig. 5.11. Free body diagram of the PRBM model.



**Fig. 5.12. (a) Effective torsional stiffness  $k_n$  in response to applied pressure  $P= 50\text{kPa}$ . FEA simulations were performed with interaction condition on and off respectively. (b) Change in  $k_n$  due to the contact of facets.**

As a result, empirical model for  $k_n$  that assuming it as a function of  $P$  and  $\theta_n$  was developed as follow:

$$k_1 = c_{11} + c_{12}P - (c_{n3} + c_{n4}P)\theta \quad (5.25)$$

For  $n>1$ ,

$$k_n = c_{n1} + c_{n2}(P - c_{n3})^2 - \{c_{n4}(P - c_{n5})^2 + c_{n6}\}\theta \quad (5.26)$$

$$+ \max(0, c_{n7}(\theta - c_{n8}P + c_{n9}))$$

The constant values for the six-module dual-origami soft fluidic robot with  $\Lambda = 0.476$  are calculated in Table 5.2. The modeling results and the simulation results for varying  $P$  and  $\theta$  are shown in Fig. 5.13.

|          |          |          |          |          |          |          |
|----------|----------|----------|----------|----------|----------|----------|
| $c_{11}$ | $c_{11}$ | $c_{11}$ | $c_{11}$ | $c_{n1}$ | $c_{n2}$ | $c_{n3}$ |
| 0.9203   | 0.0317   | -0.0019  | -0.0005  | 0.68     | 0.0024   | 40       |
| $c_{n4}$ | $c_{n5}$ | $c_{n6}$ | $c_{n7}$ | $c_{n8}$ | $c_{n9}$ |          |
| 0.000045 | 40       | 0.0043   | 0.023    | 0.875    | 31.5     |          |

**Table 5.2. Constant values in effective torsional stiffness model.**

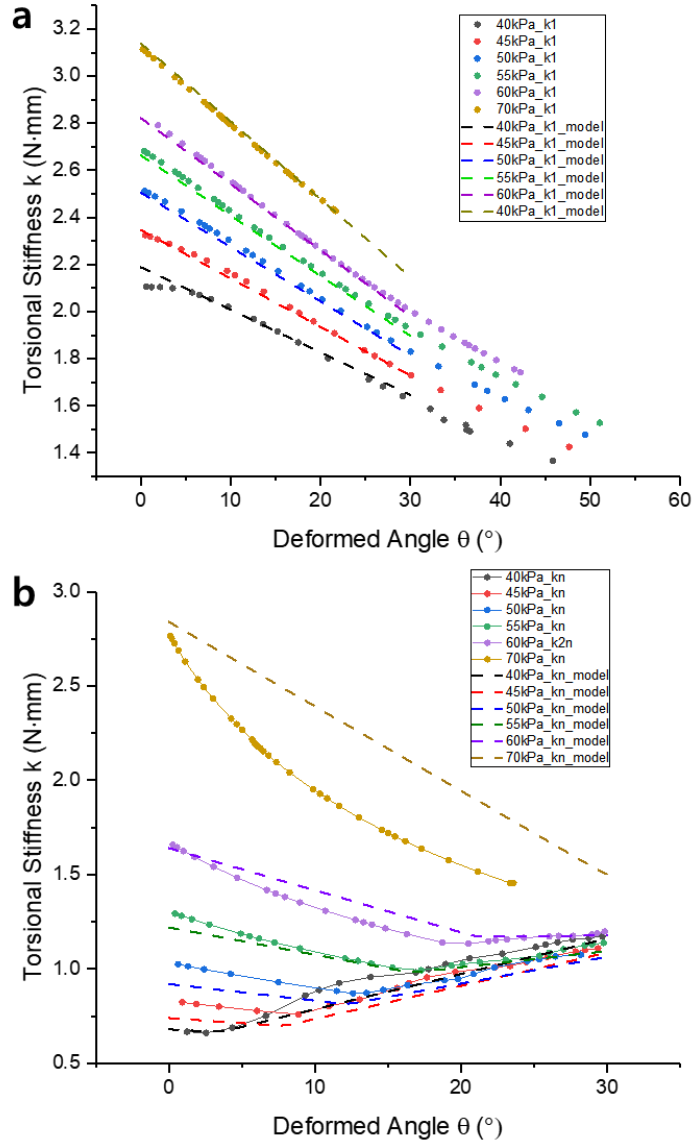


**Fig. 5.13. Modeling result of  $k_n$ . (a)  $n=1$ , and (b)  $n>1$ .**

From formula (5.24), the applied force  $F$  can be calculated using effective joint stiffness model position parameters as follows:

$$F = \frac{k_n \theta_n}{|y_T - y_n|} \quad (5.26)$$

$$F = \frac{k_n \theta_n - k_{n+1} \theta_{n+1}}{L_n \cos(\phi_i)} \quad (5.27)$$

Formula (5.26) and (5.27) show that the applied force can be estimated in two cases. (i) One effective torsional stiffness, a corresponding rotated angle and two positions of the corresponding joint and the tip are known. (ii) Two torsional stiffness, two corresponding rotated angles and one angle between the joint and the reference coordinate system. The estimated force using the pseudo rigid body model is shown in Fig. 5.14.

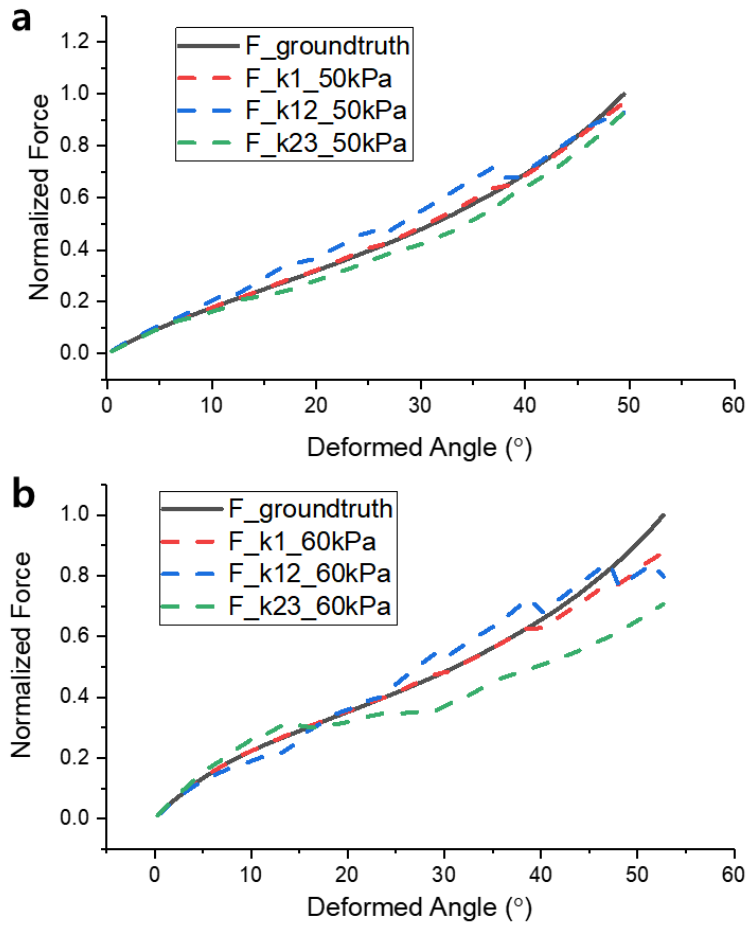


**Fig. 5.14. Force estimation for applied pressure of (a) 50 kPa and (b) 60kPa.**

## **5.5 3D Printing and Heat Treatment of Dual-origami Soft Fluidic Bending Actuator**

Soft fluidic robots are principally fabricated through molding and casting of elastomers [1], [60], [61]. However, the inevitable process of detaching cured elastomer from the molds has led to difficulties in designing complex fluidic networks because the molds are usually buried within the elastomeric structure. As a solution, using sacrificial molds, made of soluble or low melting materials such as polyvinyl alcohol (PVA) and wax, were proposed [140]. In Chapter 3, we have fabricated zigzag folded shaped origami architectures by the layer stacking method using PVA molds. However, these fabrication processes are complicated and time-consuming, while requiring experienced hands due to low material stiffnesses of the sacrificial molds. Meanwhile, 3D printing has been recently studied as an automotive fabrication method for soft robots [60], [64], [147]–[149]. In particular, FDM is a prominent and popular open-source technology with economic merits of low initial and maintenance costs. The final products can be built without supports by bridging gaps within a few centimeters, and in recent studies, researchers have directly fabricated conventional soft bending actuators made with commercially available TPU filaments [64], [149]. However, because FDM printers directly add molten material line by line, defects and gaps often occur at the boundary lines, leading to failure or fluid leakage at high fluid pressure.

We fabricated a dual-origami soft fluidic bending actuator using an FDM 3 printer as shown in Fig 5.15. (a). The printed actuator can be actuated immediately after gluing a urethane tubing with an adhesive, but failure or leakage occasionally happened when high pressure ( $>200$  kPa) was applied. For robust fabrication, we attempted a heat treatment of the fluidic soft actuator in an oven, expecting leakage prevention and enhancement of pressure holding. It was important to heat using the appropriate temperature and time; i) when either of them was insufficient, the post-processing was of little avail, and ii) when the conditions were excessive, the processed product was deformed or even melt and collapsed (Fig 5.16.). During the process, the soft bending actuator was placed between aluminum blocks to prevent possible deformation of modules at both ends. The post-processing was successful at  $172^{\circ}\text{C}$  for 2 hours (melting temperature of TPUs,  $T_m > 190^{\circ}\text{C}$ ), and the white or transparent TPUs turned yellowish after post-processing. As seen in micrographs in Fig 5.15. (b), it was observed that the boundaries between printed lines became blurred and were filled with adhered materials regardless to build direction. We verified the effectiveness by printing small test pouches and comparing maximum sealing pressure for raw and heat-treated pouches. As a result, the raw pouches could withstand 129 kPa on average, while the heat-treated pouches could withstand 756 kPa on average, which is an increase of 5.58 times (Fig 5.15. (c)).

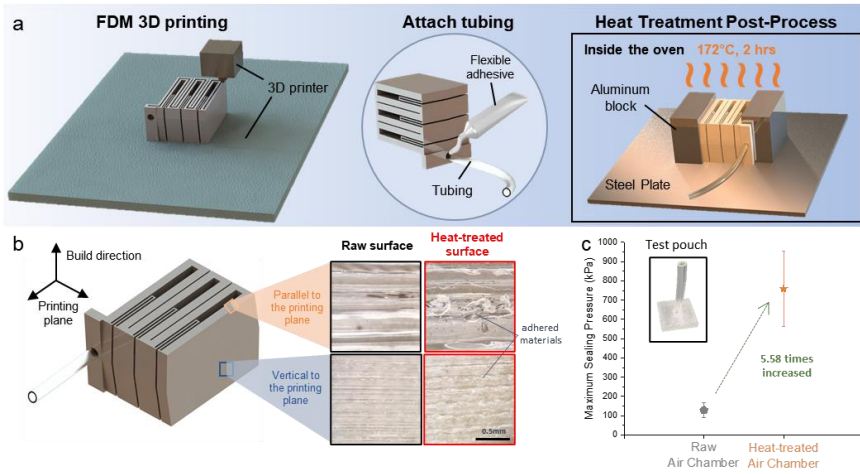


**Fig 5.15. Fabrication and reinforcement of the dual-origami soft fluidic bending actuator. (a) 3-step process of fabrication. (b) Micrographs of raw surface and heat-treated surface. (c) Maximum sealing pressure of raw air chamber and heat-treated air chamber.**

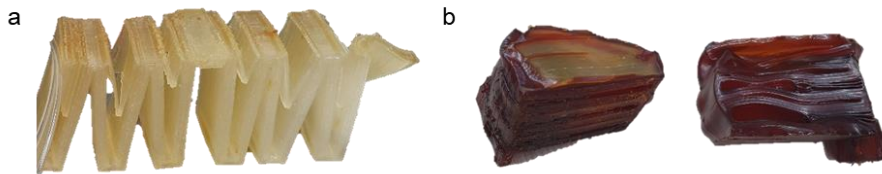


**Fig 5.16. Failure cases of the heat treatment. (a) Deformation occurred when the soft robot was heat-treated without constraining aluminum blocks. (b) The soft robots melted when heat-treated at an excessively high temperature (180°C 6 hours).**

## 5.6 Materials and Methods

### 5.6.1 Characterization and Measurement

For the parametric study, we prepared five six-module dual-origami soft fluidic bending actuators for each geometric parameter. Red or blue dots were marked with a pen on the side edge of the modules. A protruded diamond shaped crease line loop at the bottom was surrounded and held by 3d printed rigid parts, and then these rigid parts were fixed to an aluminum optical breadboard. Dual-origami soft fluidic bending actuators were installed vertically to the gravity direction to ensure that gravity does not affect the deployment. For every specimen, photographs were taken for applied pressure from 0 to 200 kPa with 10 kPa increments, which was precisely controlled by a pressure regulator (RVUM, PISCO). The photographs were analyzed with MATLAB (MathWorks). The center positions of the marked circles were automatically found and characterized based on the color information. The angle between adjacent modules ( $\theta_{ori}$  and  $\theta_{free}$ ) was derived by calculating the angle between straight lines connecting points, and effective layer length ( $L$ ) was derived using cubic Hermite spline of points at strain-limiting layer side. The bending angle ( $\phi$ ) was derived by calculating the angle between the axis in the height direction and the line connecting the floor and the end-tip trajectory. For the gripping force measurement, a regulated constant pressure (from 100 kPa to 220 kPa with 20 kPa increment for each experiments) was applied to the two-

finger gripping unit holding a cylinder located at the end of the rail connected to a load cell (333FDX, KTOYO) and a linear actuator (P16-P, Actuonix Motion Devices, Inc.). To estimate the scale of friction, the rail without external gripping force was also pulled and the friction force was measured to be as low as below 50 gf.

### **5.6.2 Finite Element Analysis**

Finite element analysis was conducted using FEA software ABAQUS (Dassault systems). Uniaxial tensile test for eFlex was performed following iso standard ASTM D412, and the result was imported into ABAQUS as a material property. All simulation conditions were set identical to the experimental conditions; the protruded diamond shaped crease line was set as a fixed boundary condition, and the contacts between facets were considered using the ‘general contact condition’. Nodes corresponding to the points marked in the actual experiment were selected and their unique nodal displacements were collected to calculate the angle between adjacent modules, deployment ratio, and bending angle.

### **5.6.3 3D Printing Process and Materials**

Commercially available flexible filament eFlex (TPU, shore hardness 87A, eSUN) was used as the 3D printing material, and all experiments were conducted with robots made of this material. Other flexible materials including

eTPU-95A (TPU, shore hardness 95A, eSUN), NinjaFlex (TPU, shore hardness 85A, NinjaTek), and eLastic (TPE, shore hardness 85A, eSUN) were also tested and it was confirmed that all of the tested materials can be used. Open-source slicing software Ultimaker Cura (Ultimaker BV) was used to prepare stereolithography (STL) files and they were imported into DIY 3D printer CORE 200 (Making Tool) using a 0.4 mm nozzle. For stable printing, the print speed was set as slow as 20 mm/s, and it took about 4 hours to print the six-module dual-origami and about 9 hours to print the dual-origami two-finger gripping unit. For stiffer material eTPU-95A, 40 mm/s of print speed could be applied, and the printing time was halved. Printer performance affected the consistency of soft robots' motion because a small error in strain-limiting layer thickness (related to bending stiffness $\sim t^3$ ) significantly changed the dominance of deployment and bending.

## 5.7 Discussion

In this section, we have presented a soft fluidic bending actuator that undergoes characteristic quasi-sequential deployment and bending motion, attributed by an asymmetric extension of dual-origami components; a folded fluidic chamber and a folded strain-limiting layer. The proposed design embodies spatial benefits of deployment and retraction that originate from origami architectures,

as well as inherent adaptiveness of soft fluidic robots. The dual-origami soft fluidic bending actuators can be directly and automatically fabricated through accessible 3D printing technology, and additional heat treatment post-processing was introduced to reinforce the material adhesion. Furthermore, we have investigated the kinematic features of the flexible soft origami robot and established a bending-to-deployment ratio factor to quantify the dominance shifting from deployment to bending. The relationship between design parameters and the motion was also explored and the tradeoff relationship between deployment and bending was demonstrated through pre-programming of six-module dual-origami fluidic bending actuators.

We believe that our approach provides a new design guidance of soft fluidic robots to embody grow-and-retract motion with a small initial form factor that considers space usage, differentiating from conventional design methods that primarily focus on motion generation. In addition, the proposed design principle is implemented by non-stretchable and flexible materials, allowing wide range of material choice. Future work may include fabrication using light and thin materials such as thermoplastic sheets (e.g., polypropylene, polyethylene), composite fabrics, and papers, to improve scalability and functionality. Further improvement such as sensor integration, real-time control and analytical modeling would complement the complexity of the combined

motion of deployment and bending. We expect that the unique property of a small form factor soft robot with grow-and-retract motion would be considered as a powerful option for applications in next-generation soft robotic systems, including portable or mobile application, medical devices, wearable robots, and integrated robotic systems.

| Notation        | Definition                                       |
|-----------------|--|
| $\lambda$       | Deployment ratio of the dual-origami robot       |
| $\phi$          | Angle of the dual-origami robot                  |
| $L$             | Effective length of the dual-origami robot       |
| $C$             | Deployment and bending ratio factor              |
| $A_0$           | Initial aspect ratio                             |
| $\theta_{ori}$  | Angle between modules with strain-limiting layer |
| $\theta_{free}$ | Angle between free modules                       |
| $l_{layer}$     | Length of the strain-limiting layer              |
| $l_{network}$   | Length of the fluidic network                    |
| $\Lambda$       | Ratio between $l_{layer}$ and $l_{network}$      |
| $k$             | Effective torsional stiffness                    |
| $\theta_n$      | Rotated angle of n-th joint                      |
| $\varphi$       | Angle between links of PRBM model                |
| $F$             | Applied external force                           |
| $y$             | Y-position of the joint                          |

**Table 5.3. Notations used in chapter 5.**

## **Chapter 6. Application: Soft Gripper Using Dual-origami Actuators**

Soft grippers with soft fluidic bending actuators acting as fingers have emerged as a promising technology for safe and delicate pick-and-place including foods, pharmaceuticals, and logistics applications [150]. With conventional soft grippers, however, the object size that can be gripped is limited by the initial configuration (Fig. 6.1. (a)). To widen the gripper opening, prestressed or bidirectional soft fluidic actuators were developed [149], [151], but the problem where the grippers should only approach the object vertically to avoid collisions still remains, which may reduce the work efficiency and increase the burden of the manipulator control and operation. To tackle the issues, in this section, we present a soft gripper using dual-origami actuators.

### **6.1 Design of the Gripper**

We constructed a dual-origami two-finger gripping unit where each finger at both sides is a six-module dual-origami fluidic soft fluidic bending actuator. The initial configuration was designed to be parallel to the objects to achieve a wide gripper opening (Fig. 6.1. (b)). The total width of the two-finger unit was relatively small compared to conventional soft robotic finger, but the finger unit

could grip larger objects, even objects larger than its initial size. In addition, because the compactness greatly reduced the risk of collision, the finger unit could approach to objects via various paths (vertical, horizontal, and diagonal from bottom to top, Fig. 6.1. (c)).

The motion and closed configuration were pre-programmed via FEA simulation and prototyping for fast and versatile grip. When all strain-limiting layers were built with the same parameters that prefer deployment over bending (Design II of Fig. 6.2.), the closed configuration was achieved at 100 kPa with a 93 mm gap. On the other hand, when the modules at the bottom were designed to be bent greatly (Design I of Fig. 6.2.), the gripping unit formed a narrow-closed configuration with a 65 mm gap at 40 kPa. Therefore, Design I can be considered as the suitable unit that allows for fast grip with sufficient contact area during power grip (grip that wraps around an object).

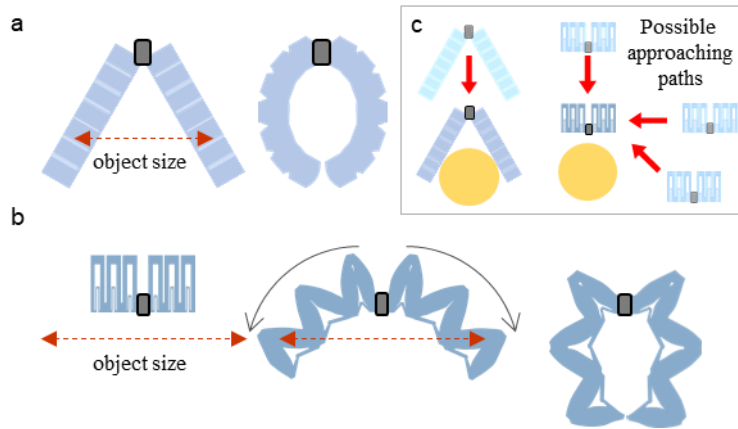


**Fig. 6.1. A dual-origami two-finger gripping unit. Gripping motion and affordable object size of (a) a conventional soft gripper and (b) a dual-origami two-finger gripping unit, and comparison of their (c) possible approaching paths.**

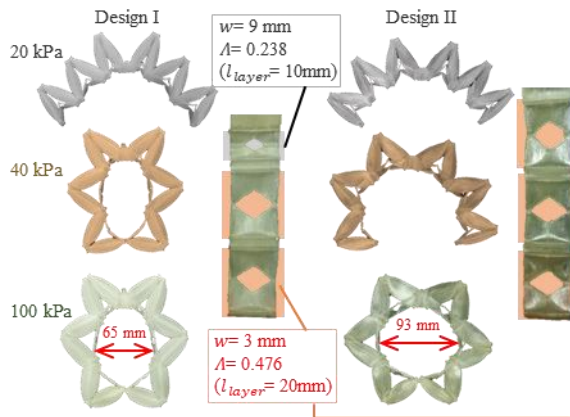


**Fig. 6.2. Motion and configuration design of the gripping units.**

## 6.2 Characterization of the Gripper

The gripping force of Design I gripping unit was measured (experimental setup is shown in Fig. 6.3. and explained in the Experimental Section). We tested gripping three PLA cylinders of different diameters, 25 mm, 50 mm and 75 mm. While the gripping unit was holding the cylinders, the cylinders were pulled at a uniform speed (3.3 mm/s). As shown in Fig. 6.4. (a), the peak force appeared during power grip, and then a relatively uniform force was measured during pinch grip, and finally the cylinder was completely pulled out. At 220 kPa, the peak force of 3.15 kgf, 1.53 kgf, and 1.25 kgf were measured for 75 mm, 50 mm, and 25 mm cylinders, respectively (Fig. 6.4. (b)). The gripping unit is lightweight (56.8 g), and the payload-to-weight ratio exceeds 55. We also tested for repeatability of the gripping unit. After 1000-cycles at 40 kPa, the bending angle of the gripping unit was changed by 8.19% compared to the 200-cycles (Fig. 6.5.).

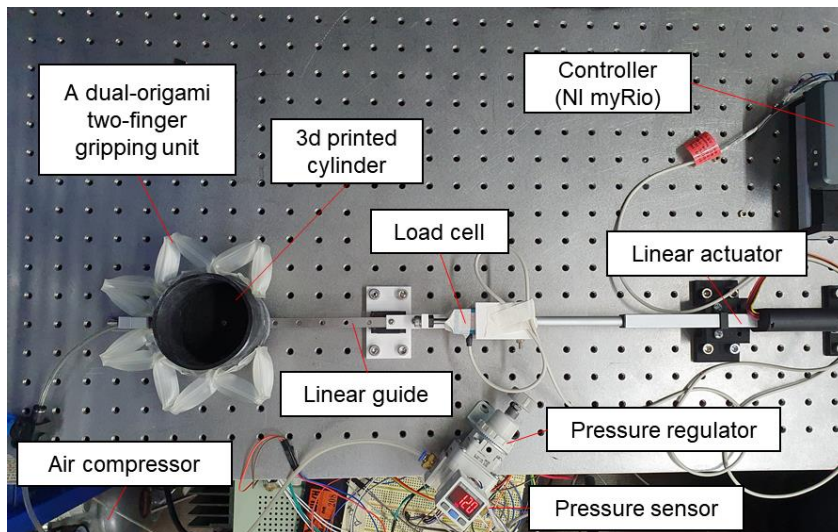


**Fig. 6.3.** Experimental setup for gripping force measurement of the dual-origami two-finger gripping unit.

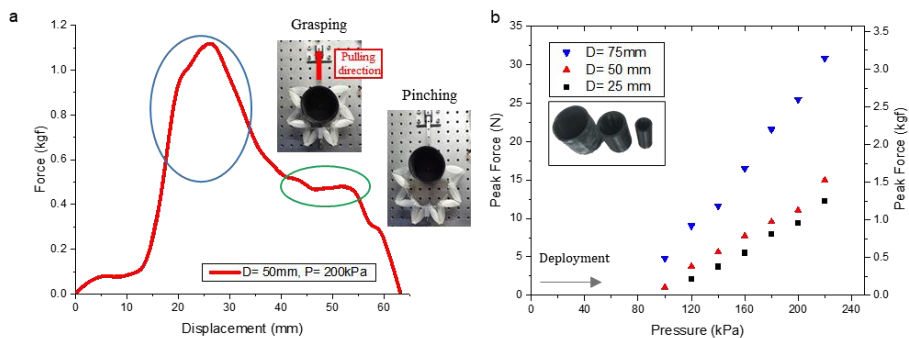


**Fig. 6.4.** (a) The gripping force of the Design I gripping unit ( $P= 200\text{kPa}$ ) when the gripped cylinder ( $D= 50\text{mm}$ ) is pulled-out. (b) Peak gripping forces of the Design I gripping unit in response to applied pressure for different cylinder diameters.

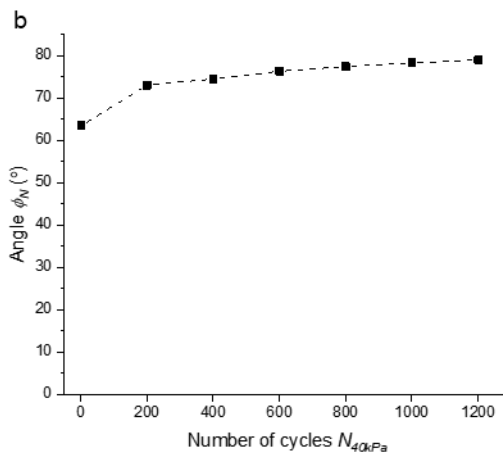
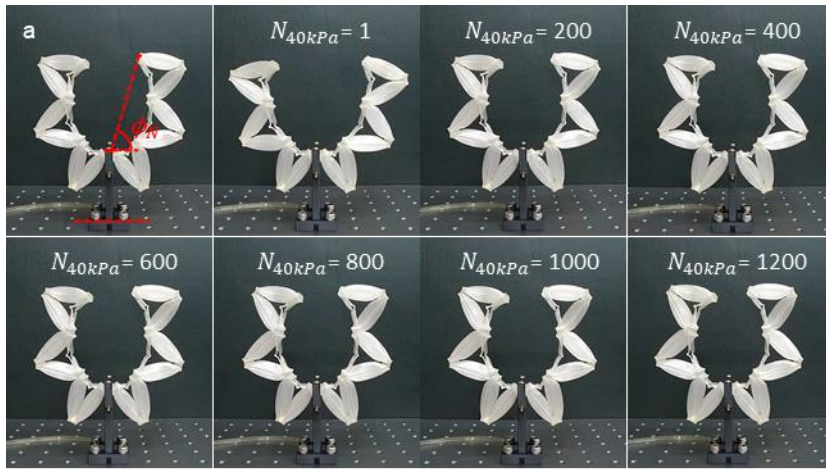


**Fig. 6.5. Repeatability test results of the dual-origami two-finger gripping unit. A) Side view of the dual-origami two-finger gripping unit at applied pressure of 40 kPa and number of cycles  $N_{40kPa}$ . B) Variation of bending angle  $\phi_N$  with the number of cycles  $N_{40kPa}$ .**

### **6.3 Development of a Versatile Soft Gripper**

As an application that leverages the spatial benefit of the retractable finger gripping unit, we developed a versatile soft gripper that uses both dual-origami fingers and suction gripper (VSS40-S-X, F.TEC, Fig. 6.6. (a)). For conventional grippers that complementarily utilize the advantages of finger grip and suction grip (in order to grip from rough and rounded object to flat and smooth object), protruding fingers interfere with the suction gripper when contacting the objects, and this problem required additional actuators and control strategies; e.g., attaching linear actuator to suction gripper [152]. In the case of our proposed versatile gripper, the folded fingers are at the rear of the suction cup; they inherently do not interfere with the suction gripper. When the finger units are actuated, they deploy to the front of the suction gripper and can grip the object by themselves or even collaborate with the suction gripper. We attached the versatile gripper to a conventional robotic arm (M1013, Doosan Robotics) and conducted a pick-and-place task for ten objects (Fig. 6.6. (b)). The soft fingers could grip various objects ranging from soft and light objects (e.g., 6-g mask, soft doll, confectionery) to a 2.5-kg dumbbell (Fig. 6.6. (c)). The suction grip was selectively used for flat objects, and fingers could be sequentially used for collaborative grasping (soup bowl). Moreover, by attaching artificial nails at the tip, the fingers could pick up a flat coin, reorient it in the upright position,

and insert it in a slot precisely (tasks that each requires strength, delicacy, precision and dexterity were conducted). Fig. 6.7. shows the soft gripper successfully conducting gripping tasks designated at the manipulation competition of Robosoft 2021. The first task requires strength to grip a heavy and large fruit (1-2 kg), and the second task requires delicacy to grip a small sized delicate fruit. Korean radish weighing 1.3 kg and raspberry were chosen respectively. The third and fourth tasks were to pick a coin and insert it into a coin slot, requiring precision and dexterity respectively. The Korean 100-won coin (24 mm diameter) was chosen and the coin slot was fabricated as 4 mm × 27 mm using an acrylic plate.

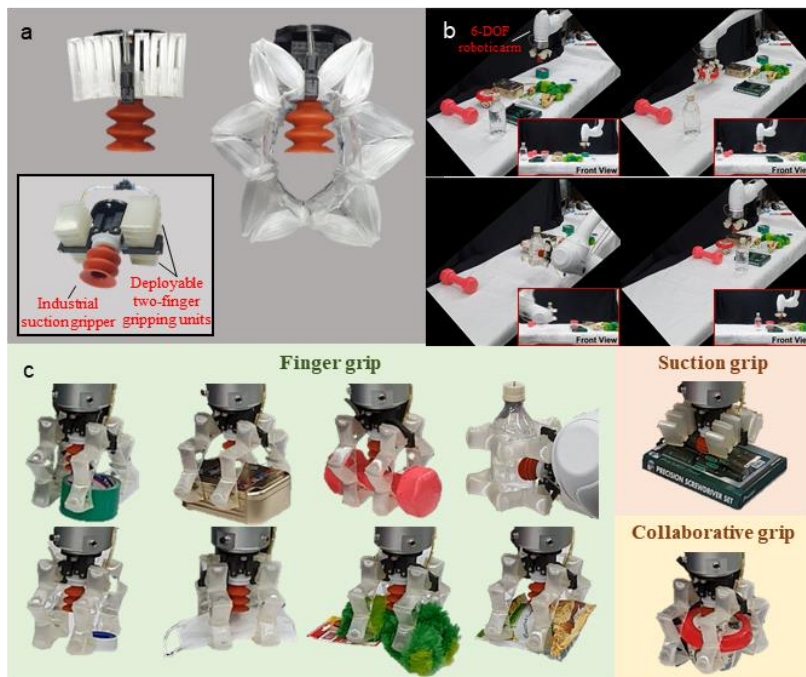


**Fig. 6.6.** A versatile soft gripper. (a) Overview of the developed gripper. (b) Pick-and-place for various objects of irregular shapes and sizes. (c) Depending on the object and environment, finger grip, suction grip, and collaborative grip could be considered respectively.

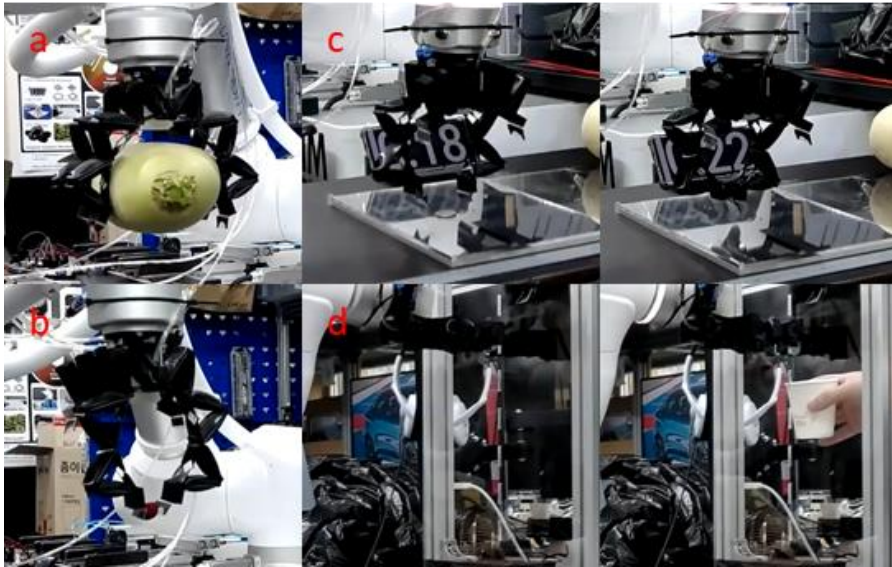


**Fig. 6.7.** A soft gripper. (a) grasping Korean radish weighing 1.3 kg, (b) raspberry, (c) a coin, and (d) inserting it in a coin slot.

## 6.4 Gripper Customized for Box-shaped Objects

The pre-programmability of the motion also enables customizing the dual-origami two-finger gripping unit according to the object shape. As shown in Fig. 6.8. (a), we built a two-finger gripping unit customized for box-shaped objects. Two strain-limiting layers at the bottom and middle modules were designed to be long ( $\lambda = 0.531$ ,  $w = 6$  mm) while the strain-limiting layer at the top module was designed to be short ( $\lambda = 0.231$ ,  $w = 9$  mm). Consequently, the two-finger gripping unit undergoes two-step motion of first widening the gripper opening significantly (from 68 mm to 215 mm) and then closing it moderately (Fig. 6.8. (a)). In the demonstration of the soft gripper with the developed two-finger gripping units, the box-shaped objects with different sizes (width of 100 mm to 208 mm, Fig. 6.8. (b)) were picked and placed (Fig. 6.8. (c) and(d)).

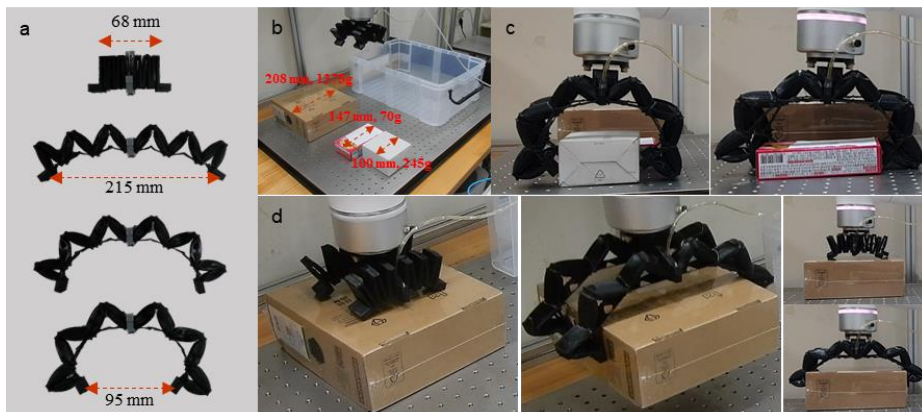


**Fig. 6.8.** A soft gripper customized for box-shaped objects. (a) Over view of the two-finger gripping unit for box-shaped objects. (b) Box-shaped objects of different sizes. (c and d) Soft gripper picking and placing different boxes.

## **6.5 Discussion**

In this section, we built the deployable two-finger gripping unit that can generate high holding force (~3.15 kg, weight 56.8 g), and applied them into a versatile soft gripper that cooperate with a commercial suction gripper. The demonstration has successfully shown that the deployable finger units can not only grow and adapt to various objects, but also can make place to the suction cup for efficient use of the entire system. Moreover, the soft gripper for box-shaped objects was proposed, showing the easy customization of the deployable two-finger gripping unit. Finally, the vision-based gripping platform was built.

## Chapter 7. Conclusion

In this thesis, the deployable soft origami structures and robots were presented. Based on the design strategy that both utilize kinematical deployment of origami and flexibility of soft materials, the developed soft origami structures produced quasi-sequential deployment and additional motion in response to a single pneumatic input. Two design methods, the dual-morphing origami design and the dual-origami design, were presented according to the material stiffness. The dual-morphing origami utilizes two morphing modes of unfolding and stretching, and can produce extreme shape morphing. On the other hands, the dual-origami utilizes asymmetric lengthening of two origami structures, and can produce relatively large force. A deployable soft bending actuator (D-PneuNets) and a deployable soft gripper were demonstrated as respective applications. The characterizations of the deployable soft actuators were studied through experiments and finite element analysis, and their pre-programming methods were established. Moreover, fabrication methods for complex origami structures, layer stacking method and mold reconfiguration method using magnets for dual-morphing origami and direct low-cost 3D printing for dual-origami, were newly developed.

## Bibliography

- [1] A. D. Marchese, R. K. Katzschmann, and D. Rus, “A recipe for soft fluidic elastomer robots,” *Soft Rob.*, vol. 2, no. 1, pp. 7–25, 2015, doi: 10.1089/soro.2014.0022.
- [2] N. S. Usevitch, Z. M. Hammond, M. Schwager, A. M. Okamura, E. W. Hawkes, and S. Follmer, “An untethered isoperimetric soft robot,” *Sci. Robot.*, vol. 5, no. 40, p. eaaz0492, 2020, doi: 10.1126/scirobotics.aaz0492.
- [3] D. Drotman, S. Jadhav, D. Sharp, C. Chan, and M. T. Tolley, “Electronics-free pneumatic circuits for controlling soft-legged robots,” *Sci. Robot.*, vol. 6, no. 51, p. aay2627, 2021, doi: 10.1126/SCIROBOTICS.AAY2627.
- [4] V. Cacucciolo, J. Shintake, Y. Kuwajima, S. Maeda, D. Floreano, and H. Shea, “Stretchable pumps for soft machines,” *Nature*, vol. 572, no. 7770, pp. 516–519, 2019, doi: 10.1038/s41586-019-1479-6.
- [5] R. F. Shepherd *et al.*, “Using explosions to power a soft robot,” *Angew. Chemie - Int. Ed.*, vol. 52, no. 10, pp. 2892–2896, 2013, doi: 10.1002/anie.201209540.
- [6] T. Nakajima, T. Yamaguchi, S. Wakabayashi, T. Arie, S. Akita, and K. Takei, “Transformable Pneumatic Balloon-Type Soft Robot Using Attachable Shells,” *Adv. Mater. Technol.*, vol. 5, no. 7, pp. 1–6, 2020, doi: 10.1002/admt.202000201.
- [7] N. D. Naclerio *et al.*, “Controlling subterranean forces enables a fast, steerable, burrowing soft robot,” *Sci. Robot.*, vol. 6, no. 55, p. abe2922, 2021, doi: 10.1126/scirobotics.eabe2922.
- [8] Y. Li, Y. Chen, T. Ren, Y. Li, and S. H. Choi, “Precharged Pneumatic Soft Actuators and Their Applications to Untethered Soft Robots,” *Soft Rob.*, vol. 5, no. 5, pp. 567–575, 2018, doi: 10.1089/soro.2017.0090.
- [9] J. Fan, S. Wang, Q. Yu, and Y. Zhu, “Swimming Performance of the

- Frog-Inspired Soft Robot,” *Soft Rob.*, vol. 7, no. 5, pp. 615–626, 2020, doi: 10.1089/soro.2019.0094.
- [10] K. M. Digumarti, A. T. Conn, and J. Rossiter, “EuMoBot: replicating euglenoid movement in a soft robot,” *J. R. Soc. Interface*, vol. 15, no. 148, p. 20180301, Nov. 2018, doi: 10.1098/rsif.2018.0301.
- [11] O. Azami, D. Morisaki, T. Miyazaki, T. Kanno, and K. Kawashima, “Development of the extension type pneumatic soft actuator with built-in displacement sensor,” *Sensors Actuators A Phys.*, vol. 300, p. 111623, Dec. 2019, doi: 10.1016/j.sna.2019.111623.
- [12] E. W. Hawkes, L. H. Blumenschein, J. D. Greer, and A. M. Okamura, “A soft robot that navigates its environment through growth,” *Sci. Robot.*, vol. 2, no. 8, p. ean3028, 2017, doi: 10.1126/scirobotics.aan3028.
- [13] D. S. Shah, J. P. Powers, L. G. Tilton, S. Kriegman, J. Bongard, and R. Kramer-Bottiglio, “A soft robot that adapts to environments through shape change,” *Nat. Mach. Intell.*, vol. 3, no. 1, pp. 51–59, 2021, doi: 10.1038/s42256-020-00263-1.
- [14] R. K. Katzschmann, J. DelPreto, R. MacCurdy, and D. Rus, “Exploration of underwater life with an acoustically controlled soft robotic fish,” *Sci. Robot.*, vol. 3, no. 16, p. eaar3449, 2018, doi: 10.1126/SCIROBOTICS.AAR3449.
- [15] W. Heng *et al.*, “Fluid-Driven Soft CoboSkin for Safer Human–Robot Collaboration: Fabrication and Adaptation,” *Adv. Intell. Syst.*, vol. 3, no. 3, p. 2000038, 2021, doi: 10.1002/aisy.202000038.
- [16] M. Cianchetti *et al.*, “Soft Robotics Technologies to Address Shortcomings in Today’s Minimally Invasive Surgery: The STIFF-FLOP Approach,” *Soft Rob.*, vol. 1, no. 2, pp. 122–131, 2014, doi: 10.1089/soro.2014.0001.
- [17] S. K. Talas, B. A. Baydere, T. Altinsoy, C. Tutcu, and E. Samur, “Design and Development of a Growing Pneumatic Soft Robot,” *Soft*

- Rob.*, vol. 7, no. 4, pp. 521–533, 2020, doi: 10.1089/soro.2019.0083.
- [18] W. Huang, J. Xiao, and Z. Xu, “A variable structure pneumatic soft robot,” *Sci. Rep.*, vol. 10, no. 1, pp. 1–15, 2020, doi: 10.1038/s41598-020-75346-5.
- [19] D. J. Preston *et al.*, “A soft ring oscillator,” *Sci. Robot.*, vol. 4, no. 31, p. aaw5496, 2019, doi: 10.1126/scirobotics.aaw5496.
- [20] E. Acome *et al.*, “Hydraulically amplified self-healing electrostatic actuators with muscle-like performance,” *Science.*, vol. 359, no. 6371, pp. 61–65, 2018, doi: 10.1126/science.aao6139.
- [21] Z. Xing, J. Zhang, D. McCoul, Y. Cui, L. Sun, and J. Zhao, “A Super-Lightweight and Soft Manipulator Driven by Dielectric Elastomers,” *Soft Rob.*, vol. 7, no. 4, pp. 512–520, 2020, doi: 10.1089/soro.2018.0134.
- [22] T. Li *et al.*, “Fast-moving soft electronic fish,” *Sci. Adv.*, vol. 3, no. 4, p. e1602045, 2017, doi: 10.1126/sciadv.1602045.
- [23] Y. Wu *et al.*, “Insect-scale fast moving and ultrarobust soft robot,” *Sci. Robot.*, vol. 4, no. 32, 2019, doi: 10.1126/scirobotics.aax1594.
- [24] G. Gu, J. Zou, R. Zhao, X. Zhao, and X. Zhu, “Soft wall-climbing robots,” *Sci. Robot.*, vol. 3, no. 25, p. eaat2874, 2018.
- [25] J. Cao *et al.*, “Untethered soft robot capable of stable locomotion using soft electrostatic actuators,” *Extrem. Mech. Lett.*, vol. 21, pp. 9–16, 2018, doi: 10.1016/j.eml.2018.02.004.
- [26] I. Must, E. Sinibaldi, and B. Mazzolai, “A variable-stiffness tendril-like soft robot based on reversible osmotic actuation,” *Nat. Commun.*, vol. 10, no. 1, pp. 1–8, 2019, doi: 10.1038/s41467-018-08173-y.
- [27] C. Wang *et al.*, “Soft Ultrathin Electronics Innervated Adaptive Fully Soft Robots,” *Adv. Mater.*, vol. 30, no. 13, pp. 1–9, 2018, doi: 10.1002/adma.201706695.
- [28] W.-B. Li *et al.*, “Electrically Activated Soft Robots: Speed Up by Rolling,” *Soft Rob.*, vol. 8, no. 5, pp. 611–624, 2021, doi:

- 10.1089/soro.2020.0012.
- [29] S. R. Goudu, I. C. Yasa, X. Hu, H. Ceylan, W. Hu, and M. Sitti, “Biodegradable Untethered Magnetic Hydrogel Milli-Grippers,” *Adv. Funct. Mater.*, vol. 30, no. 50, p. 2004975, 2020, doi: 10.1002/adfm.202004975.
- [30] E. B. Joyee and Y. Pan, “A fully three-dimensional printed inchworm-inspired soft robot with magnetic actuation,” *Soft Rob.*, vol. 6, no. 3, pp. 333–345, 2019, doi: 10.1089/soro.2018.0082.
- [31] W. Zhang, W. Zhang, and Z. Sun, “A reconfigurable soft wall-climbing robot actuated by electromagnet,” *Int. J. Adv. Robot. Syst.*, vol. 18, no. 2, pp. 1–10, 2021, doi: 10.1177/1729881421992285.
- [32] H. Niu *et al.*, “MagWorm: A Biomimetic Magnet Embedded Worm-Like Soft Robot,” *Soft Rob.*, vol. 8, no. 5, pp. 507–518, 2021, doi: 10.1089/soro.2019.0167.
- [33] Y. Kim, H. Yuk, R. Zhao, S. A. Chester, and X. Zhao, “Printing ferromagnetic domains for untethered fast-transforming soft materials,” *Nature*, vol. 558, no. 7709, pp. 274–279, 2018, doi: 10.1038/s41586-018-0185-0.
- [34] C. Zhou *et al.*, “Ferromagnetic soft catheter robots for minimally invasive bioprinting,” *Nat. Commun.*, vol. 12, no. 1, pp. 1–12, 2021, doi: 10.1038/s41467-021-25386-w.
- [35] Y. Ju *et al.*, “Reconfigurable magnetic soft robots with multimodal locomotion,” *Nano Energy*, vol. 87, no. March, p. 106169, 2021, doi: 10.1016/j.nanoen.2021.106169.
- [36] Y. Kim, G. A. Parada, S. Liu, and X. Zhao, “Ferromagnetic soft continuum robots,” *Sci. Robot.*, vol. 4, no. 33, p. aax7329, 2019, doi: 10.1126/SCIROBOTICS.AAX7329.
- [37] M. Manti, T. Hassan, G. Passetti, N. D’Elia, C. Laschi, and M. Cianchetti, “A Bioinspired Soft Robotic Gripper for Adaptable and Effective Grasping,” *Soft Rob.*, vol. 2, no. 3, pp. 107–116, 2015, doi:

- 10.1089/soro.2015.0009.
- [38] V. Vikas, E. Cohen, R. Grassi, C. Sozer, and B. Trimmer, “Design and Locomotion Control of a Soft Robot Using Friction Manipulation and Motor-Tendon Actuation,” *IEEE Trans. Robot.*, vol. 32, no. 4, pp. 949–959, 2016, doi: 10.1109/TRO.2016.2588888.
- [39] H. In, B. B. Kang, M. K. Sin, and K. J. Cho, “Exo-Glove: A wearable robot for the hand with a soft tendon routing system,” *IEEE Robot. Autom. Mag.*, vol. 22, no. 1, pp. 97–105, 2015, doi: 10.1109/MRA.2014.2362863.
- [40] C. Laschi, M. Cianchetti, B. Mazzolai, L. Margheri, M. Follador, and P. Dario, “Soft robot arm inspired by the octopus,” *Adv. Robot.*, vol. 26, no. 7, pp. 709–727, 2012, doi: 10.1163/156855312X626343.
- [41] B. B. Kang *et al.*, “Learning-Based Fingertip Force Estimation for Soft Wearable Hand Robot with Tendon-Sheath Mechanism,” *IEEE Robot. Autom. Lett.*, vol. 5, no. 2, pp. 946–953, 2020, doi: 10.1109/LRA.2020.2966391.
- [42] U. Jeong, K. Kim, S. H. Kim, H. Choi, B. D. Youn, and K. J. Cho, “Reliability analysis of a tendon-driven actuation for soft robots,” *Int. J. Rob. Res.*, vol. 40, no. 1, pp. 494–511, 2021, doi: 10.1177/0278364920907151.
- [43] H. In, U. Jeong, H. Lee, and K. J. Cho, “A Novel Slack-Enabling Tendon Drive That Improves Efficiency, Size, and Safety in Soft Wearable Robots,” *IEEE/ASME Trans. Mechatronics*, vol. 22, no. 1, pp. 59–70, 2017, doi: 10.1109/TMECH.2016.2606574.
- [44] E. Brown *et al.*, “Universal robotic gripper based on the jamming of granular material,” *Proc. Natl. Acad. Sci. U. S. A.*, vol. 107, no. 44, pp. 18809–18814, 2010, doi: 10.1073/pnas.1003250107.
- [45] C. Tawk, A. Gillett, G. M. Spinks, and G. Alici, “A 3D-Printed Omni-Purpose Soft Gripper,” *IEEE Trans. Robot.*, vol. 35, no. 5, pp. 1268–1275, 2019.

- [46] J. Y. Lee, J. Eom, S. Y. Yu, and K. Cho, “Customization Methodology for Conformable Grasping Posture of Soft Grippers by Stiffness Patterning,” *Front. Robot. AI*, vol. 7, no. September, pp. 1–15, 2020, doi: 10.3389/frobt.2020.00114.
- [47] W. Park, S. Seo, and J. Bae, “A Hybrid Gripper with Soft Material and Rigid Structures,” *IEEE Robot. Autom. Lett.*, vol. 4, no. 1, pp. 65–72, 2019, doi: 10.1109/LRA.2018.2878972.
- [48] G. D. Howard, J. Brett, J. O’Connor, J. Letchford, and G. W. Delaney, “One-Shot 3D-Printed Multimaterial Soft Robotic Jamming Grippers,” *Soft Rob.*, vol. 00, no. 00, pp. 1–12, 2021, doi: 10.1089/soro.2020.0154.
- [49] S. S. Nakshatharan, J. G. Martinez, A. Punning, A. Aabloo, and E. W. H. Jager, “Soft parallel manipulator fabricated by additive manufacturing,” *Sensors Actuators, B Chem.*, vol. 305, no. October 2019, p. 127355, 2020, doi: 10.1016/j.snb.2019.127355.
- [50] A. Shiva *et al.*, “Tendon-Based Stiffening for a Pneumatically Actuated Soft Manipulator,” *IEEE Robot. Autom. Lett.*, vol. 1, no. 2, pp. 632–637, 2016, doi: 10.1109/LRA.2016.2523120.
- [51] Y. Sun, S. Song, X. Liang, and H. Ren, “A Miniature Soft Robotic Manipulator Based on Novel Fabrication Methods,” *IEEE Robot. Autom. Lett.*, vol. 1, no. 2, pp. 617–623, 2016, doi: 10.1109/LRA.2016.2521889.
- [52] E. H. Skorina, M. Luo, and C. D. Onal, “A soft robotic wearable wrist device for kinesthetic haptic feedback,” *Front. Robot. AI*, vol. 5, no. JUN, pp. 1–11, 2018, doi: 10.3389/frobt.2018.00083.
- [53] Y. Mengüç *et al.*, “Wearable soft sensing suit for human gait measurement,” *Int. J. Rob. Res.*, vol. 33, no. 14, pp. 1748–1764, 2014, doi: 10.1177/0278364914543793.
- [54] N. Lotti *et al.*, “Adaptive model-based myoelectric control for a soft wearable arm exosuit: A new generation of wearable robot control,”

- IEEE Robot. Autom. Mag.*, vol. 27, no. 1, pp. 43–53, 2020, doi: 10.1109/MRA.2019.2955669.
- [55] W. H. Choi, S. Kim, D. Lee, and D. Shin, “Soft, Multi-DoF, Variable Stiffness Mechanism Using Layer Jamming for Wearable Robots,” *IEEE Robot. Autom. Lett.*, vol. 4, no. 3, pp. 2539–2546, 2019, doi: 10.1109/LRA.2019.2908493.
- [56] M. Runciman, A. Darzi, and G. P. Mylonas, “Soft Robotics in Minimally Invasive Surgery,” *Soft Rob.*, vol. 6, no. 4, pp. 423–443, 2019, doi: 10.1089/soro.2018.0136.
- [57] H. Abidi *et al.*, “Highly dexterous 2-module soft robot for intra-organ navigation in minimally invasive surgery,” *Int. J. Med. Robot. Comput. Assist. Surg.*, vol. 14, no. 1, pp. 1–9, 2018, doi: 10.1002/rcs.1875.
- [58] J. Zhu *et al.*, “Intelligent Soft Surgical Robots for Next-Generation Minimally Invasive Surgery,” *Adv. Intell. Syst.*, vol. 3, no. 5, p. 2100011, 2021, doi: 10.1002/aisy.202100011.
- [59] L. Paternò, G. Tortora, and A. Menciassi, “Hybrid soft-rigid actuators for minimally invasive surgery,” *Soft Rob.*, vol. 5, no. 6, pp. 783–799, 2018, doi: 10.1089/soro.2017.0140.
- [60] P. Polygerinos *et al.*, “Soft Robotics: Review of Fluid-Driven Intrinsically Soft Devices; Manufacturing, Sensing, Control, and Applications in Human-Robot Interaction,” *Adv. Eng. Mater.*, vol. 19, no. 12, p. 1700016, 2017, doi: 10.1002/adem.201700016.
- [61] F. Ilievski, A. D. Mazzeo, R. F. Shepherd, X. Chen, and G. M. Whitesides, “Soft Robotics for Chemists,” *Angew. Chemie*, vol. 123, no. 8, pp. 1930–1935, 2011, doi: 10.1002/ange.201006464.
- [62] B. Mosadegh *et al.*, “Pneumatic networks for soft robotics that actuate rapidly,” *Adv. Funct. Mater.*, vol. 24, no. 15, pp. 2163–2170, 2014, doi: 10.1002/adfm.201303288.
- [63] Y. Tang *et al.*, “Leveraging elastic instabilities for amplified performance: Spine-inspired high-speed and high-force soft robots,”

- Sci. Adv.*, vol. 6, no. 19, p. eaaz6912, May 2020, doi: 10.1126/sciadv.aaz6912.
- [64] H. K. Yap, H. Y. Ng, and C. H. Yeow, “High-Force Soft Printable Pneumatics for Soft Robotic Applications,” *Soft Rob.*, vol. 3, no. 3, pp. 144–158, 2016, doi: 10.1089/soro.2016.0030.
- [65] F. Connolly, P. Polygerinos, C. J. Walsh, and K. Bertoldi, “Mechanical programming of soft actuators by varying fiber angle,” *Soft Rob.*, vol. 2, no. 1, pp. 26–32, 2015, doi: 10.1089/soro.2015.0001.
- [66] D. Yang, M. S. Verma, E. Lossner, D. Stothers, and G. M. Whitesides, “Negative-Pressure Soft Linear Actuator with a Mechanical Advantage,” *Adv. Mater. Technol.*, vol. 2, no. 1, p. 1600164, 2017, doi: 10.1002/admt.201600164.
- [67] S. Koizumi, S. Kurumaya, H. Nabaie, G. Endo, and K. Suzumori, “Braiding thin McKibben muscles to enhance their contracting abilities,” *IEEE Robot. Autom. Lett.*, vol. 3, no. 4, pp. 3240–3246, 2018, doi: 10.1109/LRA.2018.2851025.
- [68] K. P. Becker, Y. Chen, and R. J. Wood, “Mechanically Programmable Dip Molding of High Aspect Ratio Soft Actuator Arrays,” *Adv. Funct. Mater.*, vol. 30, no. 12, p. 1908919, 2020, doi: 10.1002/adfm.201908919.
- [69] J. Deiters, W. Kowalczyk, and T. Seidl, “Simultaneous optimisation of earwig hindwings for flight and folding,” *Biol. Open*, vol. 5, no. 5, pp. 638–644, 2016, doi: 10.1242/bio.016527.
- [70] K. Saito, S. Nomura, S. Yamamoto, R. Niyama, and Y. Okabe, “Investigation of hindwing folding in ladybird beetles by artificial elytron transplantation and microcomputed tomography,” *Proc. Natl. Acad. Sci. U. S. A.*, vol. 114, no. 22, pp. 5624–5628, 2017, doi: 10.1073/pnas.1620612114.
- [71] S. M. Baek, S. Yim, S. H. Chae, D. Y. Lee, and K. J. Cho, “Ladybird beetle-inspired compliant origami,” *Sci. Robot.*, vol. 5, no. 41, p.

- eaaz6262, 2020, doi: 10.1126/SCIROBOTICS.AAZ6262.
- [72] D.-Y. Lee, J.-K. Kim, C.-Y. Sohn, J.-M. Heo, and K.-J. Cho, “High-load capacity origami transformable wheel,” *Sci. Robot.*, vol. 6, no. 53, p. eabe0201, 2021, doi: 10.1126/scirobotics.abe0201.
- [73] Y. Lin *et al.*, “Controllable Stiffness Origami ‘Skeletons’ for Lightweight and Multifunctional Artificial Muscles,” *Adv. Funct. Mater.*, vol. 30, no. 31, p. 2000349, 2020, doi: 10.1002/adfm.202000349.
- [74] C. H. Belke and J. Paik, “Mori: A Modular Origami Robot,” *ASME/IEEE Trans. Mechatronics*, vol. 22, no. 5, pp. 2153–2164, 2017.
- [75] A. Pagano, T. Yan, B. Chien, A. Wissa, and S. Tawfick, “A crawling robot driven by multi-stable origami,” *Smart Mater. Struct.*, vol. 26, no. 9, 2017, doi: 10.1088/1361-665X/aa721e.
- [76] J. Li, H. Godaba, Z. Q. Zhang, C. C. Foo, and J. Zhu, “A soft active origami robot,” *Extrem. Mech. Lett.*, vol. 24, pp. 30–37, 2018, doi: 10.1016/j.eml.2018.08.004.
- [77] S. J. Kim, D. Y. Lee, G. P. Jung, and K. J. Cho, “An origami-inspired, self-locking robotic arm that can be folded flat,” *Sci. Robot.*, vol. 3, no. 16, p. eaar2915, 2018, doi: 10.1126/scirobotics.aar2915.
- [78] H. Suzuki and R. J. Wood, “Origami-inspired miniature manipulator for teleoperated microsurgery,” *Nat. Mach. Intell.*, vol. 2, no. 8, pp. 437–446, 2020, doi: 10.1038/s42256-020-0203-4.
- [79] J. Kaufmann, P. Bhowad, and S. Li, “Harnessing the Multistability of Kresling Origami for Reconfigurable Articulation in Soft Robotic Arms,” *Soft Rob.*, vol. 00, no. 00, pp. 1–12, 2021, doi: 10.1089/soro.2020.0075.
- [80] T. Liu, Y. Wang, and K. Lee, “Three-Dimensional Printable Origami Twisted Tower: Design, Fabrication, and Robot Embodiment,” *IEEE Robot. Autom. Lett.*, vol. 3, no. 1, pp. 116–123, 2018, doi:

- 10.1109/LRA.2017.2733626.
- [81] J. Santoso and C. D. Onal, “An Origami Continuum Robot Capable of Precise Motion through Torsionally Stiff Body and Smooth Inverse Kinematics,” *Soft Rob.*, vol. 8, no. 4, pp. 371–386, 2021, doi: 10.1089/soro.2020.0026.
- [82] Z. Shen *et al.*, “Soft Origami Optical-Sensing Actuator for Underwater Manipulation,” *Front. Robot. AI*, vol. 7, no. March, pp. 1–10, 2021, doi: 10.3389/frobt.2020.616128.
- [83] S. Wu, Q. Ze, J. Dai, N. Udipi, G. H. Paulino, and R. Zhao, “Stretchable origami robotic arm with omnidirectional bending and twisting,” *Proc. Natl. Acad. Sci.*, vol. 118, no. 36, p. e2110023118, Sep. 2021, doi: 10.1073/pnas.2110023118.
- [84] M. Schenk, A. D. Viquerat, K. A. Seffen, and S. D. Guest, “Review of inflatable booms for deployable space structures: Packing and rigidization,” *Journal of Spacecraft and Rockets*, vol. 51, no. 3. pp. 762–778, 2014, doi: 10.2514/1.A32598.
- [85] N. A. Pehrson, D. C. Ames, S. P. Smith, S. P. Magleby, and M. Arya, “Self-deployable, self-stiffening, and retractable origami-based arrays for spacecraft,” *AIAA J.*, vol. 58, no. 7, pp. 3221–3228, 2020, doi: 10.2514/1.J058778.
- [86] C. Sun, W. Wan, and L. Deng, “Adaptive space debris capture approach based on origami principle,” *Int. J. Adv. Robot. Syst.*, vol. 16, no. 6, pp. 1–11, 2019, doi: 10.1177/1729881419885219.
- [87] J. Morgan, S. P. Magleby, and L. L. Howell, “An approach to designing origami-adapted aerospace mechanisms,” *J. Mech. Des. Trans. ASME*, vol. 138, no. 5, 2016, doi: 10.1115/1.4032973.
- [88] M. Johnson *et al.*, “Fabricating biomedical origami: a state-of-the-art review,” *International Journal of Computer Assisted Radiology and Surgery*, vol. 12, no. 11. pp. 2023–2032, 2017, doi: 10.1007/s11548-017-1545-1.

- [89] T. Langford, A. Mohammed, K. Essa, A. Elshaer, and H. Hassanin, “4D Printing of Origami Structures for Minimally Invasive Surgeries Using Functional Scaffold,” *Appl. Sci.*, vol. 11, no. 1, pp. 1–13, 2021, doi: 10.3390/app11010332.
- [90] M. Chauhan, J. H. Chandler, A. Jha, V. Subramaniam, K. L. Obstein, and P. Valdastri, “An Origami-Based Soft Robotic Actuator for Upper Gastrointestinal Endoscopic Applications,” *Front. Robot. AI*, vol. 8, no. May, pp. 1–15, 2021, doi: 10.3389/frobt.2021.664720.
- [91] R. V. Martinez, C. R. Fish, X. Chen, and G. M. Whitesides, “Elastomeric origami: Programmable paper-elastomer composites as pneumatic actuators,” *Adv. Funct. Mater.*, vol. 22, no. 7, pp. 1376–1384, 2012, doi: 10.1002/adfm.201102978.
- [92] S. Li, D. M. Vogt, D. Rus, and R. J. Wood, “Fluid-driven origami-inspired artificial muscles,” *Proc. Natl. Acad. Sci. U. S. A.*, vol. 114, no. 50, pp. 13132–13137, 2017, doi: 10.1073/pnas.1713450114.
- [93] B. Chen *et al.*, “Soft Origami Gripper with Variable Effective Length,” p. 2000251, 2021, doi: 10.1002/aisy.202000251.
- [94] G. Singh and G. Krishnan, “Designing Fiber-Reinforced Soft Actuators for Planar Curvilinear Shape Matching,” *Soft Rob.*, vol. 7, no. 1, pp. 109–121, 2020, doi: 10.1089/soro.2018.0169.
- [95] L. Paez, G. Agarwal, and J. Paik, “Design and Analysis of a Soft Pneumatic Actuator with Origami Shell Reinforcement,” *Soft Rob.*, vol. 3, no. 3, 2016, doi: 10.1089/soro.2016.0023.
- [96] J. A. Faber, A. F. Arrieta, and A. R. Studart, “Bioinspired spring origami,” *Science.*, vol. 359, no. 6382, pp. 1386–1391, 2018, doi: 10.1126/science.aap7753.
- [97] S. Mintchev, J. Shintake, and D. Floreano, “Bioinspired dual-stiffness origami,” *Sci. Robot.*, vol. 3, no. 20, p. eaau0275, 2018, doi: 10.1126/scirobotics.aau0275.
- [98] K. Miura and T. Tachi, “Synthesis of rigid-foldable cylindrical

- polyhedra,” *Symmetry Art Sci.*, pp. 204–213, 2010.
- [99] H. Yasuda, T. Yein, T. Tachi, K. Miura, and M. Taya, “Folding behaviour of Tachi-Miura polyhedron bellows,” *Proc. R. Soc. A Math. Phys. Eng. Sci.*, vol. 469, no. 2159, 2013, doi: 10.1098/rspa.2013.0351.
- [100] Yoshimura Yoshimaru, “On the mechanism of buckling of a circular cylindrical shell under axial compression,” *NACA*, 1955.
- [101] “Origami Fish Base Instructions.” <https://www.origamiway.com/origami-fish-base.shtml> (accessed Dec. 01, 2021).
- [102] M. J. Harrington *et al.*, “Origami-like unfolding of hydro-actuated ice plant seed capsules,” *Nat. Commun.*, vol. 2, no. 1, pp. 1–7, 2011, doi: 10.1038/ncomms1336.
- [103] M. Lemaire and R. Chase, “Twitching and quivering of the tentacles during snail olfactory orientation,” *J. Comp. Physiol. - A Sensory, Neural, Behav. Physiol.*, vol. 182, no. 1, pp. 81–87, 1997, doi: 10.1007/s003590050160.
- [104] S. Armon, E. Efrati, R. Kupferman, and E. Sharon, “Geometry and Mechanics in the Opening of Chiral Seed Pods,” *Science.*, vol. 333, no. 6050, pp. 1726–1730, Sep. 2011, doi: 10.1126/science.1203874.
- [105] Y. Forterre, J. M. Skotheim, J. Dumais, and L. Mahadevan, “How the Venus flytrap snaps,” *Nature*, vol. 433, no. 7024, pp. 421–425, Jan. 2005, doi: 10.1038/nature03185.
- [106] K. Oliver, A. Seddon, and R. S. Trask, “Morphing in nature and beyond: a review of natural and synthetic shape-changing materials and mechanisms,” *J. Mater. Sci.*, vol. 51, no. 24, pp. 10663–10689, 2016, doi: 10.1007/s10853-016-0295-8.
- [107] E. Reyssat and L. Mahadevan, “Hygromorphs: From pine cones to biomimetic bilayers,” *J. R. Soc. Interface*, vol. 6, no. 39, pp. 951–957, 2009, doi: 10.1098/rsif.2009.0184.

- [108] R. M. Erb, J. S. Sander, R. Grisch, and A. R. Studart, “Self-shaping composites with programmable bioinspired microstructures,” *Nat. Commun.*, vol. 4, no. 1, pp. 1–8, 2013, doi: 10.1038/ncomms2666.
- [109] A. Sydney Gladman, E. A. Matsumoto, R. G. Nuzzo, L. Mahadevan, and J. A. Lewis, “Biomimetic 4D printing,” *Nat. Mater.*, vol. 15, no. 4, pp. 413–418, 2016, doi: 10.1038/nmat4544.
- [110] L. Huang *et al.*, “Ultrafast Digital Printing toward 4D Shape Changing Materials,” *Adv. Mater.*, vol. 29, no. 7, pp. 1–6, 2017, doi: 10.1002/adma.201605390.
- [111] J. Kim, J. A. Hanna, M. Byun, C. D. Santangelo, and R. C. Hayward, “Designing Responsive Buckled Surfaces by Halftone Gel Lithography,” *Science.*, vol. 335, no. 6073, pp. 1201–1205, Mar. 2012, doi: 10.1126/science.1215309.
- [112] R. F. Shepherd *et al.*, “Multigait soft robot,” *Proc. Natl. Acad. Sci. U. S. A.*, vol. 108, no. 51, pp. 20400–20403, 2011, doi: 10.1073/pnas.1116564108.
- [113] E. Siéfert, E. Reyssat, J. Bico, and B. Roman, “Bio-inspired pneumatic shape-morphing elastomers,” *Nature Materials*, vol. 18, no. 1, pp. 24–28, 2019, doi: 10.1038/s41563-018-0219-x.
- [114] M. Follador, F. Tramacere, and B. Mazzolai, “Dielectric elastomer actuators for octopus inspired suction cups,” *Bioinspiration and Biomimetics*, vol. 9, no. 4, p. 046002, 2014, doi: 10.1088/1748-3182/9/4/046002.
- [115] R. Niiyama, X. Sun, C. Sung, B. An, D. Rus, and S. Kim, “Pouch motors: Printable soft actuators integrated with computational design,” *Soft Rob.*, vol. 2, no. 2, pp. 59–70, 2015, doi: 10.1089/soro.2014.0023.
- [116] H. Sareen *et al.*, “Printflatables: Printing human-scale, functional and dynamic inflatable objects,” in *Proceedings of the 2017 CHI Conference on Human Factors in Computing Systems*, 2017, vol. 2017-May, pp. 3669–3680, doi: 10.1145/3025453.3025898.

- [117] R. F. Natividad, M. R. Del Rosario, P. C. Y. Chen, and C. H. Yeow, “A hybrid plastic-fabric soft bending actuator with reconfigurable bending profiles,” in *2017 IEEE International Conference on Robotics and Automation (ICRA)*, 2017, pp. 6700–6705, doi: 10.1109/ICRA.2017.7989792.
- [118] P. H. Nguyen and W. Zhang, “Design and Computational Modeling of Fabric Soft Pneumatic Actuators for Wearable Assistive Devices,” *Sci. Rep.*, vol. 10, no. 1, pp. 1–13, 2020, doi: 10.1038/s41598-020-65003-2.
- [119] H. J. Yoo *et al.*, “Wearable lymphedema massaging modules: Proof of concept using origami-inspired soft fabric pneumatic actuators,” *2019 IEEE 16th Int. Conf. Rehabil. Robot.*, pp. 950–956, 2019, doi: 10.1109/ICORR.2019.8779525.
- [120] L. Cappello *et al.*, “Exploiting Textile Mechanical Anisotropy for Fabric-Based Pneumatic Actuators,” *Soft Rob.*, vol. 5, no. 5, pp. 662–674, 2018, doi: 10.1089/soro.2017.0076.
- [121] J. Xiong, J. Chen, and P. S. Lee, “Functional Fibers and Fabrics for Soft Robotics, Wearables, and Human–Robot Interface,” *Adv. Mater.*, vol. 33, no. 19, pp. 1–43, 2021, doi: 10.1002/adma.202002640.
- [122] Z. Pei, X. Xiong, J. He, and Y. Zhang, “Highly Stretchable and Durable Conductive Knitted Fabrics for the Skins of Soft Robots,” *Soft Rob.*, vol. 6, no. 6, pp. 687–700, 2019, doi: 10.1089/soro.2018.0048.
- [123] Z. Liu, F. Wang, S. Liu, Y. Tian, and D. Zhang, “Modeling and Analysis of Soft Pneumatic Network Bending Actuators,” *IEEE/ASME Trans. Mechatronics*, vol. 26, no. 4, pp. 2195–2203, 2020, doi: 10.1109/TMECH.2020.3034640.
- [124] B. W. K. Ang and C. H. Yeow, “Design and Modeling of a High Force Soft Actuator for Assisted Elbow Flexion,” *IEEE Robot. Autom. Lett.*, vol. 5, no. 2, pp. 3731–3736, 2020, doi: 10.1109/LRA.2020.2980990.
- [125] B. A. W. Keong and R. Y. C. Hua, “A Novel Fold-Based Design

- Approach toward Printable Soft Robotics Using Flexible 3D Printing Materials,” *Adv. Mater. Technol.*, vol. 3, no. 2, pp. 1–12, 2018, doi: 10.1002/admt.201700172.
- [126] C. Tawk, M. in het Panhuis, G. M. Spinks, and G. Alici, “Soft Pneumatic Sensing Chambers for Generic and Interactive Human–Machine Interfaces,” *Adv. Intell. Syst.*, vol. 1, no. 1, p. 1900002, 2019, doi: 10.1002/aisy.201900002.
- [127] H. D. Yang and A. T. Asbeck, “A Layered Manufacturing Approach for Soft and Soft-Rigid Hybrid Robots,” *Soft Rob.*, vol. 7, no. 2, pp. 218–232, 2020, doi: 10.1089/soro.2018.0093.
- [128] A. A. A. Moghadam, A. Caprio, S. Alaie, J. K. Min, S. Dunham, and B. Mosadegh, “Rapid manufacturing of thin soft pneumatic actuators and robots,” *J. Vis. Exp.*, vol. 2019, no. 153, pp. 1–5, 2019, doi: 10.3791/60595.
- [129] P. Polygerinos, Z. Wang, K. C. Galloway, R. J. Wood, and C. J. Walsh, “Soft robotic glove for combined assistance and at-home rehabilitation,” in *Robotics and Autonomous Systems*, 2015, vol. 73, pp. 135–143, doi: 10.1016/j.robot.2014.08.014.
- [130] K. H. L. Heung, R. K. Y. Tong, A. T. H. Lau, and Z. Li, “Robotic Glove with Soft-Elastic Composite Actuators for Assisting Activities of Daily Living,” *Soft Rob.*, vol. 6, no. 2, pp. 289–304, 2019, doi: 10.1089/soro.2017.0125.
- [131] P. Polygerinos *et al.*, “Modeling of Soft Fiber-Reinforced Bending Actuators,” *IEEE Trans. Robot.*, vol. 31, no. 3, pp. 778–789, 2015, doi: 10.1109/TRO.2015.2428504.
- [132] J. Wang, Y. Fei, and W. Pang, “Design, Modeling, and Testing of a Soft Pneumatic Glove with Segmented PneuNets Bending Actuators,” *IEEE/ASME Trans. Mechatronics*, vol. 24, no. 3, pp. 990–1001, 2019, doi: 10.1109/TMECH.2019.2911992.
- [133] P. Polygerinos *et al.*, “Towards a soft pneumatic glove for hand

- rehabilitation,” *2013 IEEE/RSJ Int. Conf. Intell. Robot. Syst.*, pp. 1512–1517, 2013, doi: 10.1109/IROS.2013.6696549.
- [134] S. S. Yun, B. B. Kang, and K. J. Cho, “Exo-glove PM: An easily customizable modularized pneumatic assistive glove,” *IEEE Robot. Autom. Lett.*, vol. 2, no. 3, pp. 1725–1732, 2017, doi: 10.1109/LRA.2017.2678545.
- [135] L. Gerez, J. Chen, and M. Liarokapis, “On the Development of Adaptive, Tendon-Driven, Wearable Exo-Gloves for Grasping Capabilities Enhancement,” *IEEE Robot. Autom. Lett.*, vol. 4, no. 2, pp. 422–429, 2019, doi: 10.1109/LRA.2019.2890853Y.
- [136] T. T. Worsnopp, M. A. Peshkin, J. E. Colgate, and D. G. Kamper, “An actuated finger exoskeleton for hand rehabilitation following stroke,” *2007 IEEE 10th Int. Conf. Rehabil. Robot. ICORR’07*, pp. 896–901, 2007, doi: 10.1109/ICORR.2007.4428530.
- [137] I. Jo and J. Bae, “Design and control of a wearable and force-controllable hand exoskeleton system,” *Mechatronics*, vol. 41, pp. 90–101, 2017, doi: 10.1016/j.mechatronics.2016.12.001.
- [138] M. Fontana, A. Dettori, F. Salsedo, and M. Bergamasco, “Mechanical design of a novel hand exoskeleton for accurate force displaying,” *Proc. - IEEE Int. Conf. Robot. Autom.*, pp. 1704–1709, 2009, doi: 10.1109/ROBOT.2009.5152591.
- [139] Z. Wang, R. Kanegae, and S. Hirai, “Circular Shell Gripper for Handling Food Products,” *Soft Rob.*, 2020, doi: 10.1089/soro.2019.0140.
- [140] A. Koivikko and V. Sariola, “Fabrication of soft devices with buried fluid channels by using sacrificial 3D printed molds,” in *2019 2nd IEEE International Conference on Soft Robotics (RoboSoft)*, 2019, pp. 509–513, doi: 10.1109/ROBOSOFT.2019.8722741.
- [141] S. Joshi and J. Paik, “Pneumatic Supply System Parameter Optimization for Soft Actuators,” *Soft Rob.*, vol. 8, no. 2, pp. 152–163,

- 2021, doi: 10.1089/soro.2019.0134.
- [142] T. Tachi and K. Miura, “Rigid-foldable cylinders and cells,” *J. Int. Assoc. Shell Spat. Struct.*, vol. 53, no. 174, pp. 217–226, 2012.
- [143] H. Shima, M. Sato, and S.-J. Park, “Suppression of Brazier Effect in Multilayered Cylinders,” *Adv. Condens. Matter Phys.*, vol. 2014, pp. 1–10, 2014, doi: 10.1155/2014/923896.
- [144] T. W. Murphey, D. Turse, and L. Adams, “TRAC Boom Structural Mechanics,” in *4th AIAA Spacecraft Structures Conference*, Jan. 2017, no. January, pp. 1–13, doi: 10.2514/6.2017-0171.
- [145] V. Polenta, S. D. Garvey, D. Chronopoulos, A. C. Long, and H. P. Morvan, “Optimal internal pressurisation of cylindrical shells for maximising their critical bending load,” *Thin-Walled Struct.*, vol. 87, pp. 133–138, Feb. 2015, doi: 10.1016/j.tws.2014.11.012.
- [146] H. M. Mourad and M. Y. A. Younan, “Limit-Load Analysis of Pipe Bends Under Out-of-Plane Moment Loading and Internal Pressure,” *J. Press. Vessel Technol.*, vol. 124, no. 1, pp. 32–37, Feb. 2002, doi: 10.1115/1.1425807.
- [147] E. Sachyani Keneth, A. Kamyshny, M. Totaro, L. Beccai, and S. Magdassi, “3D Printing Materials for Soft Robotics,” *Adv. Mater.*, vol. 33, no. 19, pp. 1–17, 2021, doi: 10.1002/adma.202003387.
- [148] T. J. Wallin, J. Pikul, and R. F. Shepherd, “3D printing of soft robotic systems,” *Nature Reviews Materials*, vol. 3, no. 6, pp. 84–100, 2018, doi: 10.1038/s41578-018-0002-2.
- [149] J. H. Low, J. Y. Goh, N. Cheng, P. M. Khin, Q. Q. Han, and C. H. Yeow, “A Bidirectional 3D-printed Soft Pneumatic Actuator and Graphite-based Flex Sensor for Versatile Grasping,” in *2020 IEEE International Conference on Robotics and Automation (ICRA)*, 2020, pp. 7979–7985, doi: 10.1109/ICRA40945.2020.9196837.
- [150] “mGrip modular gripping system (Soft Robotics, inc).” <https://www.softroboticsinc.com/products/mgrip-modular-gripping->

solution-for-machine-builders (accessed May 01, 2021).

- [151] Z. Wang, Y. Torigoe, and S. Hirai, “A Prestressed Soft Gripper: Design, Modeling, Fabrication, and Tests for Food Handling,” *IEEE Robot. Autom. Lett.*, vol. 2, no. 4, pp. 1909–1916, 2017, doi: 10.1109/LRA.2017.2714141.
- [152] “The RightPick system (RightHand Robotics, Inc.)” <https://www.righthandrobotics.com/products> (accessed May 01, 2021).

## 초 록

본 논문에서는 유연재료로 만든 전개형 종이접기 구조를 개발하고 이를 전개 및 추가 동작이 가능한 소프트 로봇으로 활용하는 연구들을 기술하였다. 전개형 종이접기 구조는 운동학적으로 정의된 변형을 접힘 및 펴짐으로 구현한다. 개발한 유연 전개형 종이접기 구조는 종이접기 기존 가동범위에 더하여 유연재료의 신축에 의한 가동범위를 지니게 된다. 이에 공압 구동을 가능케하면 인가하는 압력에 따라 접힘 및 펴짐에 의한 가동과 유연재료의 신축에 의한 가동을 유사-연속적으로 거치도록 유도될 수 있다. 개발한 설계 기법은 크게 2가지로, 접이식 구조의 펴짐과 유연재료의 인장을 각각 활용하는 이중-모핑(Dual-morphing) 설계 원리와 접이식 구조의 펴짐에 차이를 주는 이중-종이접기(Dual-origami) 설계 원리가 있다.

심해에 서식하는 물고기인 펠리컨 장어 (학술명 *Eurypharynx pelecanoides*)의 머리뼈를 전개한 뒤 피부를 늘이는 독특한 거동에서 영감을 얻어 종이접기의 펴짐과 고인장 엘라스토머 재료 표면의 늘어남을 유사-연속적으로 구현하는 이중-구동 종이접기 구조를 개발하였다. 개발한 구조는 전체가 늘어날 수 있는 종이접기 단위로

유체 네트워크(fluid networks)가 구성되어 있다. 이중-모핑의 특징인 유사-연속 구동은 유체 구조 및 재료적으로 설계된 유체 네트워크에 유압이 물체의 전개를 우선적으로 하는 방향으로 작동하여 나타나게 된다. 개발한 설계 기법을 확인하기 위해, 펠리컨 장어를 모사하는 인공 생물을 제작하였고 이중-모핑 특성을 유사하게 함을 확인하였다. 이중-모핑 종이접기 셀을 기존의 종이접기 구조에 적용하여 전개 가능한 그리퍼, 크롤러, 그리고 수중 로봇을 개발하였다. 나아가 하나의 적용 사례로, 이중-모핑 구조 중 요시무라 종이접기 실린더 (Yoshimura origami cylinder)를 활용한 소프트 공압 구동기를 개발하였다. 개발한 전개가능한 소프트 공압 구동기 (D-PneuNets actuator)는 인가된 공압에 의해 공압 챔버들이 높이방향으로 자라서 모멘트 암을 키울 수 있어, 낼 수 있는 힘과 구동기 부피의 트레이드-오프 관계를 극복할 수 있다. 또한, 전개가능한 소프트 공압 구동기를 활용하는 공간 효율적인 착용형 로봇 장갑을 개발하였다.

이중-종이접기(Dual-origami) 설계 원리는 공압으로 구동되는 종이접기 구조와 종이접기 레이어를 연결하여 설계한 것으로, 두 종이접기 구조의 펴지는 길이 차이를 이용하여 전개 및 굽힘의 유사-연속구동을 구현한다. 고인장 엘라스토머에 비해 비교적 강성이 높은 재료를 사용하고 재료의 인장을 활용하지 않으므로

상대적으로 높은 힘을 낼 수 있으며 저가형 FDM(Fused Deposition Modeling) 3D 프린터로 간단한 제작이 가능하다. 두 종이접기 구조의 거동차이를 설계하여 전개와 굽힘의 비중을 조절할 수 있다. 이를 활용하여 개발한 전개형 소프트 그리퍼는 힘, 섬세함, 정확성, 그리고 민첩함을 요구하는 파지 업무를 수행할 수 있으며, 접혀 있는 상태의 높은 공간 효율성은 물리적 간섭없이 흡입 컵 그리퍼와 함께 사용할 수 있도록 하였다.

본 학위논문에서 개발한 전개형 종이접기 구조의 설계 기법들은 소프트 로봇을 사용하지 않을 때의 작은 형태에서 사용시 전개 후 기능적인 동작을 가능하게 하는 설계 지침을 제공하여, 고도화된 차세대 소프트 로봇 시스템에 적용될 수 있을 것으로 기대된다.

**주요어:** 소프트 로봇, 종이접기 공학, 폴리머 기반, 공압 구동, 종이접기, 소프트 그리퍼

**학 번:** 2015-20720